



RETURNING MATERIALS:
Place in book drop to
remove this checkout from
your record. FINES will
be charged if book is
returned after the date
stamped below.

--	--	--

FRAGMENT PRODUCTION IN INTERMEDIATE
ENERGY HEAVY ION REACTIONS

By

Barbara Vincenta Jacak

A DISSERTATION

Submitted to
Michigan State University
in partial fulfillment of the requirements
for the degree of

DOCTOR OF PHILOSOPHY

Department of Chemistry

1984

ABSTRACT

FRAGMENT PRODUCTION IN INTERMEDIATE ENERGY HEAVY ION REACTIONS

By

Barbara Vincenta Jacak

The emission of fragments with $A \leq 14$ has been studied in intermediate energy argon and neon-induced reactions. The energy spectra were observed to be approximately Maxwellian and the high energy region was fitted assuming emission from a single moving source. The source was found to move with a velocity intermediate between that of the projectile and the target, and its temperature was approximately independent of the mass of the emitted fragment, suggesting that complex fragments as well as light particles are emitted from a thermalized subsystem in the reaction.

A quantum statistical model of the disassembly of the thermalized region was used to infer information about the entropy of the system from the observed fragment distribution. This method yields lower values for the entropy per nucleon than derived from the production of protons and deuterons alone. The entropy extracted from target-like fragments observed in other experiments was found to be lower than the entropy from intermediate rapidity fragments, and was independent of the projectile energy. The complex fragment spectra through nitrogen were

also well described by the coalescence model, yielding source radii of 4.5-5.5 fm, in agreement with experiments measuring two-proton correlations.

The light particle data were used to test two models for the collision dynamics. A solution of the Boltzmann equation, incorporating a mean field and Pauli blocking as well as two-nucleon collisions, described the proton spectra from Ar + Ca for bombarding energies as low as 42 MeV/A. A conventional intranuclear cascade model, developed for high energy collisions, was unable to reproduce the data, underlining the importance of nuclear mean field and Pauli blocking effects in this energy regime. Nuclear fluid dynamical calculations were also compared with the data. The agreement was fair above 100 MeV/nucleon, but the model did not describe the lower energy data.

ACKNOWLEDGEMENTS

I wish to thank Dr. David Scott, my research advisor, for his guidance, instruction and support during my graduate career. His interest in me and in my future is very gratefully acknowledged, and his advice will always be welcome.

It is a pleasure to thank Dr. Gary Westfall for his teaching, support, advice, humor, and patience. His concern for this project and for me brought this dissertation within reach, and made graduate school a lot of fun.

I would also like to thank Drs. Horst Stocker and Hans Kruse for their patient teaching and assistance, and interest in this work. Their contributions to the theoretical analyses of these experiments and to my scientific education are greatly appreciated.

I also wish to extend my appreciation to the other researchers who have collaborated on some aspect of this research project: Drs. Konrad Gelbke, Gary Crawley, Bruce Hasselquist, Leigh Harwood, Bill Lynch, Betty Tsang, James Symons, Martin Murphy, Robert Legrain and Truett Majors. Thanks are due to Richard Au and Ron Fox for their invaluable help in taming the NSCL computers.

Gratitude is expressed to Drs. Henry Blosser and Sam Austin for the extensive travel support which I have received throughout my graduate career. Financial support in the form of research assistantships funded by the National Science Foundation is gratefully acknowledged. I wish to thank Bruce Hasselquist, Zach Koenig, Janaki Narayanaswami, Charles Chitwood, Patty Pirnie and Kevin Wolf for their friendship and support during these years of graduate school. The help of Theresa Perkins and Shari Conroy in preparing this dissertation is greatly appreciated.

Most of all, I thank my parents and my sister, Mary, for their encouragement, support, and love. They were the ones who convinced me that this was possible.

TABLE OF CONTENTS

	Page
LIST OF TABLES.....	vii
LIST OF FIGURES.....	viii
Chapter	
I. INTRODUCTION.....	1
A. Motivation.....	1
B. Organization.....	14
II. EXPERIMENTAL.....	17
A. Argon-Induced Reactions.....	19
1. Detector Systems.....	22
2. Electronics.....	26
3. Data Reduction.....	28
B. Neon-Induced Reactions.....	30
1. Detector Systems.....	32
2. Electronics.....	32
3. Data Reduction.....	36
III. RESULTS.....	37
A. Double Differential Cross Sections.....	37
B. Rapidity Plots.....	53
IV. SINGLE MOVING SOURCE PARAMETERIZATION.....	63
A. Rationale.....	63
B. Fitting Procedure.....	64

C.	Limitations.....	73
D.	Discussion of Parameters.....	75
E.	Systematics of the Temperature.....	88
F.	Three Moving Sources.....	91
V.	THERMAL MODELS.....	96
A.	The Fireball Model.....	96
B.	Deuteron-to-Proton Ratios and Entropy.....	104
C.	Quantum Statistical Model.....	109
1.	Description.....	109
2.	Calculated Deuteron-to- Proton Ratios.....	112
D.	Entropy Extracted from Fragment Distributions.....	115
1.	Intermediate Rapidity Fragments.....	118
2.	Rapidity Dependence of the Entropy.....	121
E.	Coalescence Model.....	128
VI.	DYNAMICAL MODELS.....	142
A.	Boltzmann Equation.....	142
1.	High Energy Cascade Models.....	142
2.	Nucleon-Nucleon Cross Sections.....	146
3.	Pauli Blocking.....	147
4.	Mean Field Term.....	150
5.	Generalized Coalescence.....	155

6. Comparison With Data.....	158
B. Nuclear Fluid Dynamics.....	165
1. Description.....	165
2. Comparison With Data.....	167
VII. SUMMARY AND CONCLUSIONS.....	175
A. Summary of Results.....	175
B. Conclusions.....	178
LIST OF REFERENCES.....	181

LIST OF TABLES

Table		Page
II-1	Energy range of fragments detected in the multi-element silicon telescopes used for the Ar-induced reactions.....	25
II-2	composition, size, highest energy proton stopped, and opening and solid angles for light particle telescopes used for the Ne-induced reactions.....	33
IV-1	Low energy cutoffs for moving source fits to light particle spectra.....	69
IV-2	Coulomb shifts used in moving source fits to spectra of particles from Ar-induced reactions.....	71
IV-3	Coulomb shifts used in moving source fits to spectra of particles from Ne-induced reactions.....	72
IV-4	Moving source parameters extracted for Ar + Au reactions.....	76
IV-5	Moving source parameters extracted for Ar + Ca reactions.....	77
IV-6	Moving source parameters extracted for Ne-induced reactions.....	78
IV-7	Parameters for fit to 137 MeV/A Ar + Au data with three moving sources.....	95
V-1	Values for coalescence and source radii for typical light and heavy fragments from Ar-induced reactions.....	141
VI-1	Renormalization factors for comparison of fluid dynamical results to light particle data for Ar + Au reactions.....	173

LIST OF FIGURES

Figure	Page	
I-1	Schematic illustration of heavy-ion collision processes, as a function of impact parameter (vertical scale) and bombarding energy (horizontal scale).....	3
I-2	Variation with incident energy above the Coulomb barrier of the temperature extracted from the proton spectra.....	7
I-3	An emulsion picture of a complete disintegration event induced by a 70 MeV/a ^{12}C nucleus.....	9
I-4	Density contour plots exhibiting the reaction dynamics predicted by TDHF (left) and a nuclear fluid dynamical model (right).....	13
II-1	Layout of the Low Energy Beam Line at the Bevalac.....	18
II-2	Scattering chamber configuration for measurement of the argon induced reactions.....	20
II-3	Electronics diagram for measurement of the argon induced reactions.....	27
II-4	Sample ΔE vs. E contour plot for heavy fragments.....	29
II-5	Scattering chamber configuration for measurement of the neon induced reactions.....	31
II-6	Electronics diagram for measurement of the neon induced reactions.....	35
III-1	Double differential cross sections for hydrogen isotopes produced in Ar + Au reactions. Data at 30, 50, 70, 90, 110, and 130° are shown for each particle. The solid lines are fits with a single moving source parameterization.....	38
III-2	Double differential cross sections for hydrogen	

	isotopes produced in Ar + Ca reactions.....	39
III-3	Double differential cross sections for helium isotopes produced in Ar + Au reactions.....	40
III-4	Double differential cross sections for helium isotopes produced in Ar + Ca reactions.....	41
III-5	Double differential cross sections for lithium isotopes produced in Ar + Au reactions. Data at 30, 50, 70, and 90° are shown for each particle. The solid lines are fits with a single moving source parameterization.....	43
III-6	Double differential cross sections for lithium isotopes produced in Ar + Ca reactions.....	44
III-7	Double differential cross sections for beryllium isotopes produced in Ar + Au reactions.....	45
III-8	Double differential cross sections for beryllium isotopes produced in Ar + Ca reactions.....	46
III-9	Double differential cross sections for boron isotopes produced in Ar + Au reactions.....	47
III-10	Double differential cross sections for carbon and nitrogen produced in Ar + Au reactions, without isotope separation.....	49
III-11	Double differential cross sections for boron and carbon produced in Ar + Ca reactions, without isotope separation.....	50
III-12	Double differential cross sections for p,d,t, and ⁴ He from Ne + Au reactions. Data at 50, 70, 90, 110, and 130° are shown. The solid lines are fits with a single moving source parameterization.....	51
III-13	Double differential cross sections for p,d, and t from 156 MeV/A Ne + Al. Data at 50, 70, 90, 110, and 130° are shown for each particle. The solid lines are fits with a single moving source parameterization.....	52
III-14	Contours of constant cross section in the rapidity vs. perpendicular momentum plane for	

	protons produced in Ar + Au and Ar + Ca reactions. Dashed semicircles indicate contours expected for emission from a target-like source, and dot-dashed semicircles indicate contours from a midrapidity source.....	57
III-15	Schematic illustration of a rapidity plot for a symmetric system. The plot is Lorentz transformed into the center of mass frame, and the data reflected through the center of mass rapidity.....	59
III-16	Same as Figure III-14, for ${}^4\text{He}$	61
III-17	Same as Figure III-14, for ${}^7\text{Be}$	62
IV-1	Proton spectrum for 137 MeV/A Ar + Au, calculated from complete disassembly of the fireball at the most probable impact parameter (dashed lines), and disassembly of the fireball + spectator fragments (solid lines).....	66
IV-2	Temperatures extracted from the spectra of fragments emitted from argon-induced reactions, as a function of the fragment mass.....	79
IV-3	The ratio of the source velocity extracted from the fragment spectra to the projectile velocity for argon induced reactions, as a function of the fragment mass.....	81
IV-4	The integrated fragment production cross sections for Ar + Au, as a function of the fragment mass.....	83
IV-5	The integrated fragment production cross sections for Ar + Ca, as a function of the fragment mass.....	84
IV-6	The ratio of composite fragment cross sections to the proton cross sections for argon induced reactions on Au and Ca targets.....	86
IV-7	Projectile dependence of the moving source parameters describing light particle spectra, for Ar and Ne beams on Au targets.....	87
IV-8	Bombarding energy dependence of the temperatures	

	extracted from the spectra of p,d, and t. The solid line is to guide the eye through the data, the dashed line is the temperature expected from a Fermi gas model, and the dot-dashed line is the prediction of the fireball model.....	89
IV-9	Fits to the p,d, and ³ He spectra from 137 MeV/A Ar + Au with three moving sources.....	94
V-1	Schematic diagram of the reaction geometry in the fireball model, illustrating the participant-spectator picture with a central "participant" region where the projectile and target overlap, and the cooler "spectator" remnants.....	98
V-2	Predictions of the fireball model (solid lines) and data for p,d, and ³ He from 137 MeV/nucleon Ar + Au.....	102
V-3	Bombarding energy dependence of the entropy as calculated for viscous (S_{η}) and non-viscous (S_{ζ}) fluids. Also shown are the "S" values obtained from measured and calculated deuteron-to-proton ratios.....	108
V-4	Deuteron-to-proton ratios calculated from the quantum statistical model at two breakup densities, $\rho=0.1 \rho_0$, and $0.5 \rho_0$. The primordial and final (after decay of excited states) ratios are shown.....	113
V-5	Ratio of deuteron-like to proton-like particles from the quantum statistical model at two breakup densities, as in Figure V-4. The primordial $R_{d/z}$ includes only the ground states of nuclei with $2 \leq A \leq 4$	116
V-6	Temperatures from single moving source fits to fragment spectra from Ar + Au, as a function of the fragment mass.....	117
V-7	a) Fragment production cross sections. The solid and dashed histograms are results of quantum statistical and Hauser-Feshbach calculations, respectively. b) Entropy extracted from the fits, as a function of bombarding	

	energy. The solid and dashed lines are the entropies expected from non-viscous and viscous fluids [ST 84].....	119
V-8	Mass distributions of target rapidity fragments. The histograms are fits with the quantum statistical model.....	123
V-9	Extracted entropy per nucleon: a) from target rapidity fragments and b) from midrapidity fragments. The solid and dashed lines represent the weighted average for fragments with $1 < A < 3$ and $1 < A < 4$, respectively. The three grouped solid lines show the entropy calculated using a fireball geometry and a Fermi gas model at three different values of ρ/ρ_0	124
V-10	Intermediate rapidity fragment distributions, and quantum statistical model results. In a) and b) fragments with $1 < A < 4$ are fitted, while in c) only fragments with $1 < A < 3$ are fitted.....	127
V-11	Energy spectra at 30° of fragments from 137 MeV/A Ar + Au.....	131
V-12	Energy spectra at 90° of fragments from 137 MeV/A Ar + Au.....	132
V-13	Coalescence model fits to the deuteron spectra from argon induced reactions. The angles shown are 30° , 50° , 70° , 90° , 110° , and 130° ; all angles were fitted with a single coalescence radius....	134
V-14	Coalescence model fit to the ${}^7\text{Be}$ spectrum from 137 MeV/A Ar + Au. The angles shown are 30° , 50° , 70° , and 90° ; all angles were fitted with a single coalescence radius.....	135
V-15	Coalescence model results for fragment spectra at a) 30° and b) 90°	137
V-16	Coalescence radii extracted from fragment spectra, as a function of fragment mass.....	138
VI-1	Nucleon-nucleon total cross sections used to determine collision probabilities in the Boltzmann equation model.....	148

VI-2	Spatial and momentum distributions of nucleons inside the nuclei at $t=0$ (solid lines) and $t=40$ fm/c (dashed lines) under the influence of the mean field term alone.....	153
VI-3	Particle positions and momenta (indicated by the arrows) for 42 MeV/A Ar + Ca collisions at $b=0$ and $b=5$ fm. The time development of the reaction from $t=10$ fm/c to $t=60$ fm/c is shown...	154
VI-4	The results of the Boltzmann equation model for 800 MeV p + C. Inclusive proton spectra at 15° , 30° , 40° , and 60° are shown by the points, and the calculation by the histograms. Statistical errors in the calculation are indicated.....	159
VI-5	Inclusive proton angular distributions for Ar + Ca reactions. The data are indicated by the points and the Boltzmann equation results by the solid lines.....	161
VI-6	Inclusive proton spectra for 137 MeV/A Ar + Ca. The data are indicated by the points. a) the histograms show results of the Boltzmann equation calculation. b) the histograms are results obtained with the cascade model [CU 81]..	162
VI-7	The Boltzmann equation calculation is compared to the proton spectra for a) 92 MeV/A Ar + Ca and b) 42 MeV/A Ar + Ca.....	164
VI-8	Time evolution of the 84 MeV/A $^{12}\text{C} + \text{Au}$ reaction in a fluid dynamical calculation for impact parameters $b=1, 3, 5,$ and 7 fm.....	168
VI-9	Fluid dynamical results (solid lines) for light particle spectra from 137 MeV/A Ar + Au.....	169
VI-10	Fluid dynamical results (solid lines) for light particle spectra from 92 MeV/A Ar + Au.....	170
VI-11	Fluid dynamical results (solid lines) for light particle spectra from 42 MeV/A Ar + Au.....	171

CHAPTER I
INTRODUCTION

A. MOTIVATION

Heavy ion reactions have provided a unique opportunity to study the chemistry of nuclear matter. Chemists and physicists have used low energy beams to study the nuclear response in relatively gentle collisions, and reactions at high bombarding energies to heat and compress nuclear matter and study its bulk properties. Very different theoretical frameworks for understanding the reaction mechanisms in these two energy regimes have been developed, but a complete description of the transition from low to high energy reactions does not yet exist. Historically, the development of heavy ion accelerators has focussed on beams at the extremes in energy; only recently have machines been constructed to address the intermediate energy transition region. The new accelerators have allowed measurements at bombarding energies between 20 and 200 MeV/nucleon, thus testing existing reaction models at the limits of their applicability. The data presented in this work give a survey of the intermediate energy domain and provide a testing ground for new theories. The theory presented here is a first attempt at incorporating both low and high energy phenomena and applying the result at intermediate energy.

Figure I-1 schematically illustrates the mechanisms of nuclear reactions as a function of incident energy and impact parameter [SC 81]. At low energies (a few MeV/nucleon), the duration of the collision is much longer than the transit time of a nucleon at the Fermi energy, and the whole nucleus responds to the collision. Central collisions lead to complete fusion [RE 65, LE 74, BI 79], while more peripheral collisions proceed by deeply-inelastic scattering, where the nuclei rotate about each other, exchanging nucleons and excitation energy [SC 77, VO 78, GO 80, BR 79]. The division appears to be set by a critical separation,

$$d_c = 1.0 (A_1^{1/3} + A_2^{1/3}) \quad (I-1)$$

where the nuclei overlap at their half-density points [GL 75]. In this region, an additional reaction mechanism of fast fission of the binary nuclear system may occur [GR 81] on a time and impact parameter scale between the other two mechanisms. The excited residual nuclei deexcite by emitting neutrons, gamma rays or charged particles, or in the case of heavy target nuclei, by fission.

Above 10 MeV/ nucleon neither the entire projectile mass nor the entire projectile momentum is absorbed by the target. In central collisions, only some of the projectile nucleons may be captured by the target; the rest escape

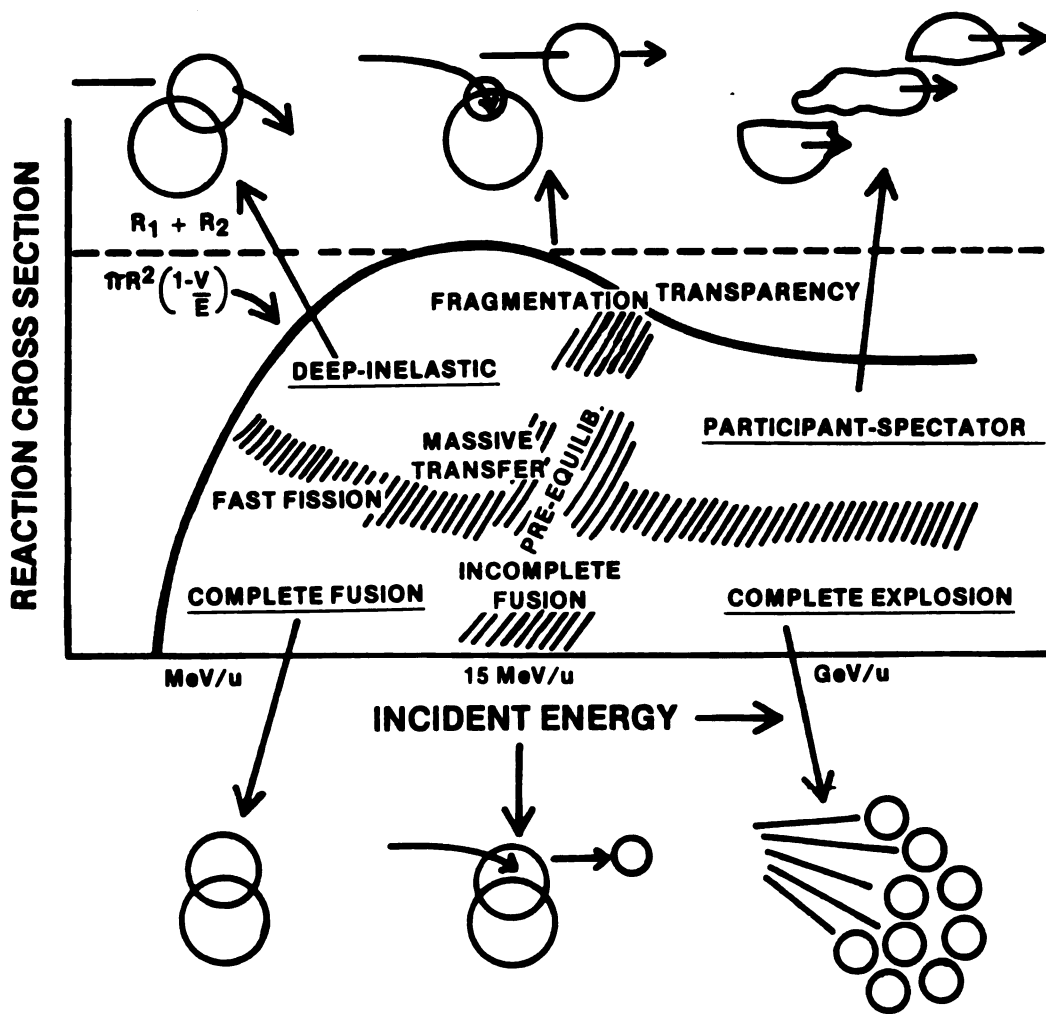


FIGURE I-1. Schematic illustration of heavy-ion collision processes, as a function of impact parameter (vertical scale) and bombarding energy (horizontal scale).

giving rise to incomplete fusion reactions [SI 79, WI 80, WU 80]. In more peripheral collisions, part of the projectile may be sheared off and interact with the target, leaving a relatively undisturbed fragment of the projectile moving at the original velocity [GE 78].

Collisions in the low energy regime are dominated by the nuclear mean field. The nucleons involved in the reaction interact with the rest of the nucleons in the system via a potential field. Dynamical models which address such collisions often use a time-dependent Hartree-Fock (TDHF) approach [BO 76, WO 77, CU 80, NE 82, WO 82] in which the motion of quantum-mechanical particles in a mean field is followed as the reaction proceeds in time. The Pauli principle prevents two-body scattering at low energies, but above 20 MeV/nucleon two-body collisions do take place, and a pure mean-field approach becomes inadequate [ST 80].

At very high energies, at the right in Figure I-1, the contact time between projectile and target is shorter and they may become somewhat transparent to one another [JA 78]. Central collisions result in breakup of the system into many fragments, and are characterized by a high multiplicity of light charged particles [GO 77, SA 80, NA 81, CE 81] and large, slow target fragments [WA 83]. Such reactions produce highly excited, compressed nuclear matter [GO 79, PR 83, PR 83a, NA 84], and have been studied in 4π

experiments, which measure all emitted particles simultaneously [GU 83, SA 83].

An important concept for the description of peripheral collisions is the separation of the observed fragments into participants and spectators [GU 76]. When the relative velocity of the two colliding nuclei is higher than the speed at which information is propagated through nuclear matter, the early stage of the reaction is localized to the overlapping volume of the target and projectile nuclei. The remaining fragments of the target and projectile retain much of their original velocity and are only slightly excited. At forward angles, cold projectile fragments accompanied by few emitted light particles are observed [GR 75]. Inclusive neutron [CE 81], light particle [PO 75, ME 80, SA 80, SY 80, NA 81, NA81a] and complex fragment [GO 77, ST 77, LE 79, WA 83] spectra measured at larger angles were analyzed with thermal models based on the participant and spectator concept. Fragment data from proton-induced reactions [HY 71, WE 78, GR 80, GR 84a] have been compared to those from heavy ion-induced reactions, and the spectra also appear thermal in origin.

In the intermediate energy region between 15 and 200 MeV/nucleon, a transition is expected to occur from the mean field description of low energy interactions to the two-body scattering behavior typical of high energies [SC 81]. A rather long mean free path is typical of the TDHF approach, but as the two-body collisions become more important, the

mean free path decreases, resulting in a strong thermalization of the incident momentum [ST 80]. A short mean free path might lead us to expect hydrodynamic behavior of the nucleons taking part in the reaction, and models using this assumption have been developed [AM 75, ST 79, ST 80a, NI 81, CS 83]. The transition in mechanism is expected to result when the velocity of the colliding nucleons surpasses both the Fermi velocity and the velocity of sound in nuclear matter; it is, however, unlikely that the transition is a sharp one.

Recently, experiments aimed at filling in the gap between 20 and 200 MeV/nucleon bombarding energy have been performed (for a review, see BO 84). Inclusive spectra of light particles produced in collisions from 25 - 156 MeV/nucleon have been measured [JA 81, NA 81a, WE 82, GL 82, LY 82, AU 82, AU 83, WE 84, JA 84]. These data have been analyzed in the framework of the participant-spectator model. The spectra were fitted assuming emission from a thermalized subset of target and projectile nucleons, a method which resulted in a successful parameterization of light particle data at as low as 20 MeV/nucleon bombarding energy [AW 81, AW 82].

The parameters describing the spectra vary smoothly with bombarding energy [WE 82]; Figure I-2 shows the temperature of the source emitting the particles, plotted as a function of the bombarding energy per nucleon above the Coulomb barrier. The smoothness is somewhat surprising as a

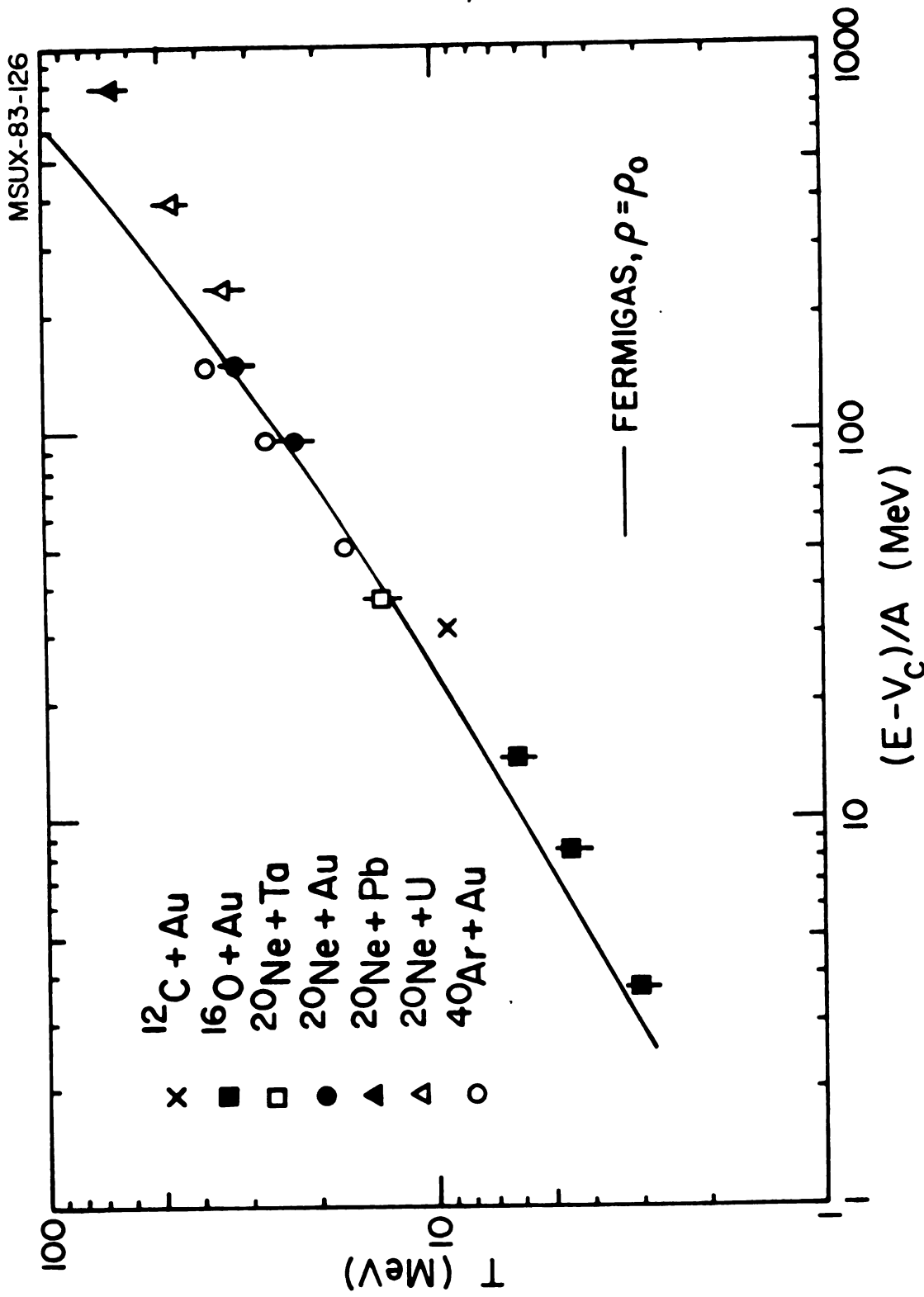


FIGURE I-2. Variation with incident energy above the Coulomb barrier of the temperature extracted from the proton spectra.

20 MeV/nucleon projectile moves slowly enough to allow considerable exchange of information with the target. This contrasts with the participant-spectator picture, yet the characteristics of the emitting source do not show any sharp discontinuities as a function of bombarding energy. It has been suggested that at bombarding energies where the participants and spectators are not yet well separated, a local thermalized zone, or hot spot, is formed [GO 79a, ST 81a, FR 83, FI 84]. As the bombarding energy goes up, this hot spot breaks away from the target, and becomes the "participant" zone.

Light emitted particles do not present the entire picture for intermediate energy reactions. For bombarding energies below 32-50 MeV/nucleon the excitation energy in the hot region is insufficient to unbind the participant matter into free nucleons [GA 80]. As a consequence, many complex fragments, especially alpha particles which are very tightly bound, are produced in the reaction. An example of a collision at 70 MeV/nucleon is shown in Figure I-3 [JA 82]. A ^{12}C nucleus enters the emulsion film from the left, and undergoes a reaction with an Ag or Br nucleus. This results in 16 visible charged particle tracks (4 deuterons, 7 alpha particles, 3 lithium and 2 beryllium fragments) containing a total of about 71 nucleons. In the case of a C + Br event, this corresponds to a complete breakup of the system into fragments with $A < 12$. If the target is Ag, a fragment with $Z = 18$ is missing. It should be noted that

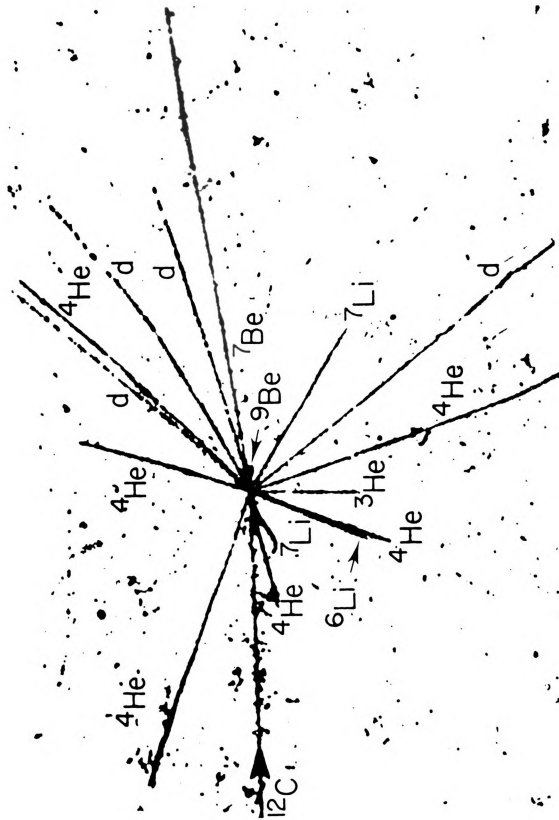


FIGURE I-3. An emulsion picture of a complete disintegration event induced by a 70 MeV/A ^{12}C nucleus.

this is not a rare type of event - such events account for approximately 20 % of the total reaction cross section. It is clear from Figure I-3 that a considerable number of fragments heavier than ${}^4\text{He}$ are emitted in intermediate energy reactions (some are seen in relativistic heavy ion reactions at small impact parameters [ME 80, WA 83], but generally the products at high energies are light charged particles).

Fragment inclusive cross sections for $Z \leq 10$ and $E \leq 200$ MeV have been measured at 30 MeV/nucleon bombarding energy [CH 83, SO 83, FI 84]. Production of higher energy ($E \leq 800$ MeV) fragments has been studied at 30 MeV/nucleon [JA 84], 55-110 MeV/nucleon [FR 81, JA 82] and 250 MeV/nucleon [WA 83]. The data were fitted similarly to the light particle spectra, and the heavier fragments also appear to originate from thermalized sources.

In order to gain more detailed information about the reaction mechanisms, experiments with some kinematic restrictions have been performed. Many of these first coincidence experiments have focussed on coincidences between large fragments arising from projectile or target remnants and fast charged particles. Studies at and below 35 MeV/nucleon have revealed that light charged particles associated with a projectile remnant are most likely to be found in one of two places: either focussed directly behind the fragment, consistent with a sequential breakup of the excited projectile [WU 79, WU 79a, BI 80, CA 84], or

focussed to the opposite side of the beam from the projectile fragment, suggesting emission from a recoiling source [GO 83, CA 84]. This trend continues even to 92 MeV/nucleon [HA 84]. These experiments are beginning to trace out the evolution of the projectile fragmentation mechanism from deeply-inelastic reactions, where the reaction time is long enough to excite the projectile.

Target-like residues detected in coincidence with light particles change very slowly with bombarding energy from 30-54 MeV/nucleon [BO 83]. However, the linear momentum transferred to the target by the projectile (as measured by the opening angle of the fission fragments) falls with increasing energy [GA 82, LA 83, TS 84, PO 84], and fusion of the projectile and target ceases to be important above 40 MeV/nucleon [LE 83, TS 84]. At 86 MeV/nucleon, complex fragments with $10 < A < 50$ are associated with central collisions, but the light charged particle multiplicity for these events is low [LY 82]. For heavy targets, the fragments appear to result from binary breakup, while for lighter targets such as Ag, breakup into 3 or more fragments is observed [LY 82].

The observation that many gross features change very slowly and regularly between 20 and 200 MeV/nucleon has inspired the use of theories at the limits of their applicability. The expected transition in the importance of two-body collisions and the mean free path of nucleons has led to the application of TDHF and hydrodynamical

calculations at intermediate energies [ST 80]. These two approaches are compared for a central collision in Figure I-4. The density plots on the left show the time evolution of a Kr + Kr reaction in a TDHF calculation. It is clear that the nuclei pass through one another, and very little compression takes place. The hydrodynamical calculation, on the other hand, indicates a total lack of transparency of the nuclei. The incoming matter is stopped and squeezed out to the side. Realistically, one would expect a mixture of the one-body dissipation inherent in the nucleon + mean field picture of TDHF and the two-body dissipation of hydrodynamics at intermediate energies [GR 84].

Therefore, a theory aimed at these reactions must include the nuclear mean field, Pauli blocking and two-nucleon collisions. A convenient framework for such a theory has been found in the Monte Carlo method used in intranuclear cascade calculations [BE 76, YA 79, YA 81, CU 81, CU 82, CU 82a, TO 83]. Most cascade calculations, however include two-body collisions only, with a crude approximation for the Pauli principle, rendering them ineffective for intermediate energy collisions. First attempts to fully incorporate the required physics use a Monte Carlo solution of the full Boltzmann equation [BE 84, MA 84]. This method agrees well with high energy data [KR 84] and shows promising results at intermediate energies [KR 84a]. Inclusive proton cross sections for 40-140 MeV/nucleon reactions, where 80-90% of the two-nucleon

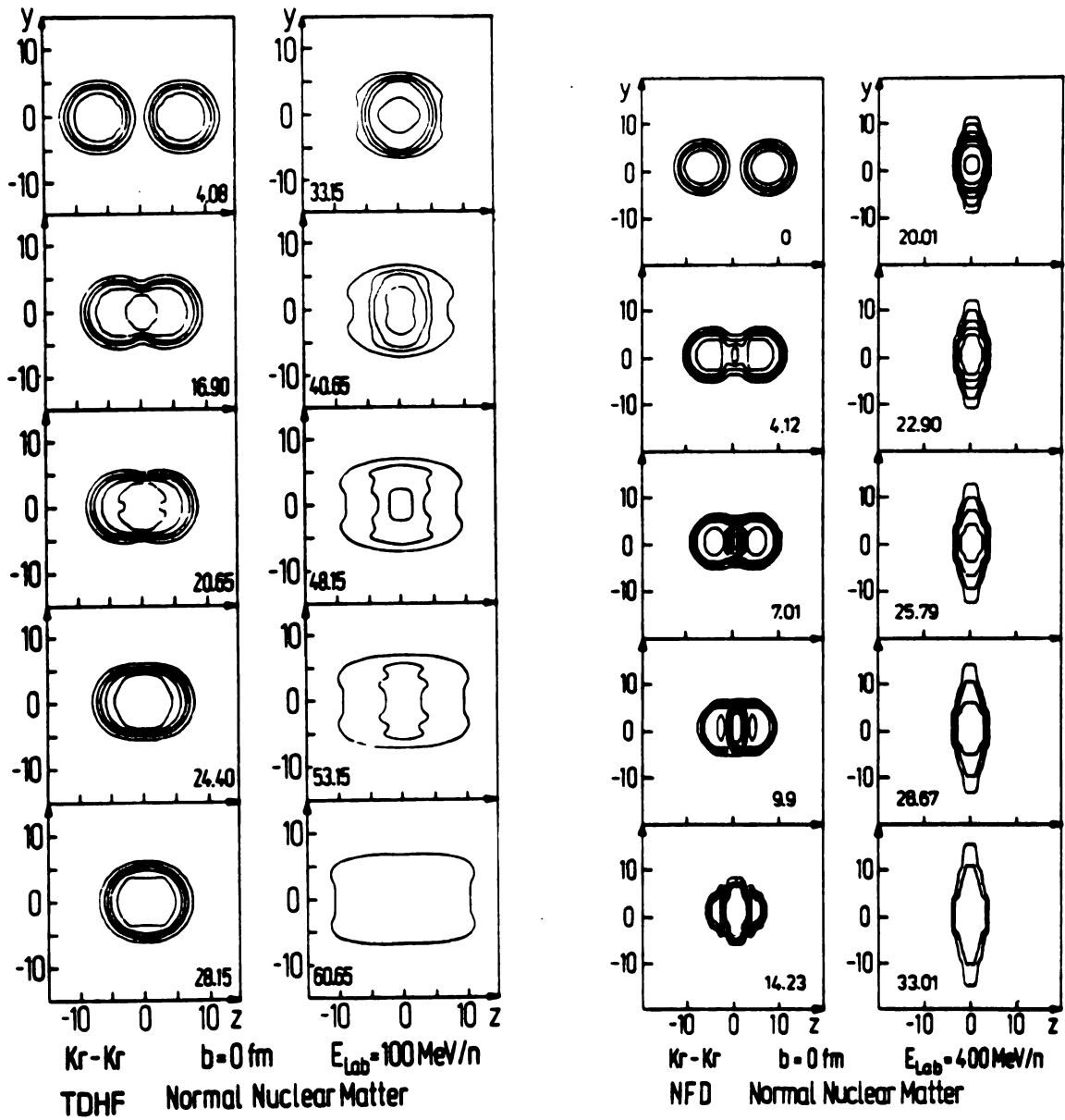


FIGURE I-4. Density contour plots exhibiting the reaction dynamics predicted by TDHF (left) and a nuclear fluid dynamical model (right).

collisions are Pauli blocked, are well reproduced. Thus, a first description of the dynamics of these reactions seems to be within our grasp.

B. ORGANIZATION

In this work we present single particle inclusive measurements of particles with $1 \leq A \leq 14$ from 42, 92, and 137 MeV/nucleon Ar + Au and Ar + Ca reactions. Also, we report light particle ($1 \leq A \leq 4$) measurements from 100 and 156 MeV/nucleon Ne + Au and 156 MeV/nucleon Ne + Al. The details of experimental setup, detector calibration techniques, data acquisition and data reduction are presented in the second chapter of this dissertation.

The double differential spectra look approximately exponential as a function of the energy of the observed particle. They are presented in Chapter III. The rapidity of the outgoing particles is calculated, and Chapter III also presents contours of constant cross section plotted in the plane of rapidity vs. perpendicular momentum/mass. These plots emphasize the rapidity of the source of the particles, and point to the existence of a source intermediate in rapidity between the projectile and the target, which gives rise to the particles in the high energy tails of the spectra.

In Chapter IV the spectra are parameterized via a single moving source prescription. The source temperature

and velocity and the integrated cross section for particle emission are determined via a least squares fit of a relativistic Boltzmann distribution in a moving frame to the measured spectra. The systematics of the source parameters are examined as a function of the projectile, target and beam energy.

Chapter V reviews several models of the reaction which incorporate thermalization of the incident energy. The light particle spectra are used to explore the low energy limits of applicability of the fireball model [WE 76]. The assumption of thermal and chemical equilibrium is used to extract information about bulk properties of nuclear matter from the inclusive data. If the heated subsystem freezes into various fragments, the relative yields of the fragments reflect the entropy in the system at the time of freezeout [ST 83, JA 83]. Alternatively, the fragments may be formed by coalescence of nucleons close together in phase space. The fragment spectra are compared to proton spectra to investigate the validity and extent of this phenomenon.

In Chapter VI, two dynamical models are discussed. The light particle data are used to test the performance of hydrodynamical [ST 79, ST 80a] models in this energy regime. These spectra are also used as a first test of the Boltzmann equation approach to intermediate energy heavy ion collision [KR 84a]. The dynamics of the Ar + Ca interaction are followed using a Monte Carlo solution of the equation [BE 84]. This model incorporates the Pauli blocking and nuclear

mean field necessary for low energy reactions and the nucleon-nucleon collision terms typical of high energy approaches, and is applied at all three bombarding energies.

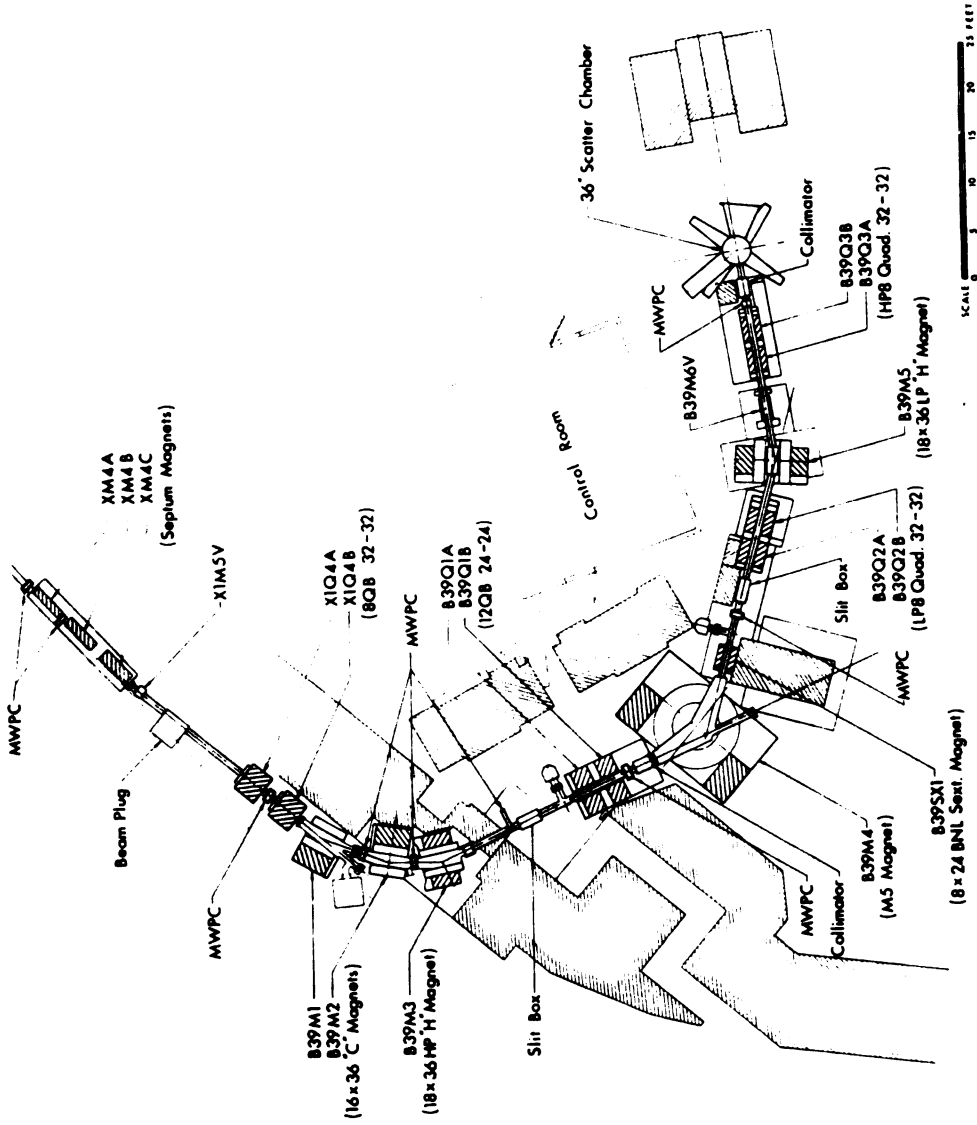
The last chapter is a summary of the present work. The experiments and calculations presented in this dissertation have shown that the transition between low and high energy nuclear reactions is a smooth one, and intermediate energy collisions show characteristics of both. We have also learned that single particle inclusive measurements provide a useful survey, but coincidence experiments, with kinematic selection of the measured quantities, are required to trace the evolution of specific reaction mechanisms.

CHAPTER II

EXPERIMENTAL

The experiments were done at the Lawrence Berkeley Laboratory Bevalac. Bevalac beams are first accelerated to 8.5 MeV/nucleon at the SuperHILAC, which consists of two Alvarez-type linac sections separated by a stripper foil to deliver higher charge-to-mass state ions into the second tank. The fully stripped ion beam leaves the SuperHILAC and is transported 500 feet to the Bevatron injector line. The Bevatron is a weak focusing synchrotron composed of four quadrant magnets separated by 6' long straight sections. The beam enters the Bevatron over many turns within a 500 microsecond interval, filling the vacuum ring completely. Toward the end of the injection pulse, the rf accelerating voltage is turned on and the ions maintain a constant radius as they gain energy in the rising magnetic guide field. The field is flattopped at a predetermined value to give the desired ion energy. The pulse rate is 10-15 pulses per minute.

The extracted beam pulses are delivered to the six physics and three biology/medicine beam lines. The present experiments took place in the Low Energy Beam Line; Figure II-1 shows the beam line layout. Quadrupole doublets are located at the entrance to the beam line and after each of the three bends. Waists are formed at the two slit boxes,



BEVALAC BEAM NO. 39

FIGURE II-1. Layout of the Low Energy Beam Line at the Bevalac.

and the two quad doublets between the second box and the target allow minimization of the beam spot size.

A. ARGON-INDUCED REACTIONS

The experimental setup consisted of three particle telescopes. One telescope consisted of two silicon ΔE detectors and a NaI E detector to detect particles of $Z=1,2$. This telescope was mounted on a movable arm inside the Low Energy Beam Line 60-inch scattering chamber, and was moved from 30° to 130° with respect to the beam direction. Mounted on a separately movable arm in the scattering chamber were two stacks of silicon detectors for measurement of particles with $Z=3-7$. The scattering chamber arrangement is shown in Figure II-2. All three telescopes achieved isotopic resolution for the elements detected. Events consisting of a particle detected in any one telescope were accepted into the computer and stored on magnetic tape in event by event mode. On line displays were used for monitoring the experiment, but the final analysis was performed off line.

The targets used were all self-supporting and consisted of 80 mg/cm^2 Au and 35 mg/cm^2 Ca for the 42 and 92 MeV/nucleon Argon beams, and 200 mg/cm^2 Au and 160 mg/cm^2 Ca for the 137 MeV/nucleon Ar beam. In all, six beam-target combinations were measured.

The relative normalizations were determined by the integrated beam current in an ionization chamber downstream

MSU-84-225

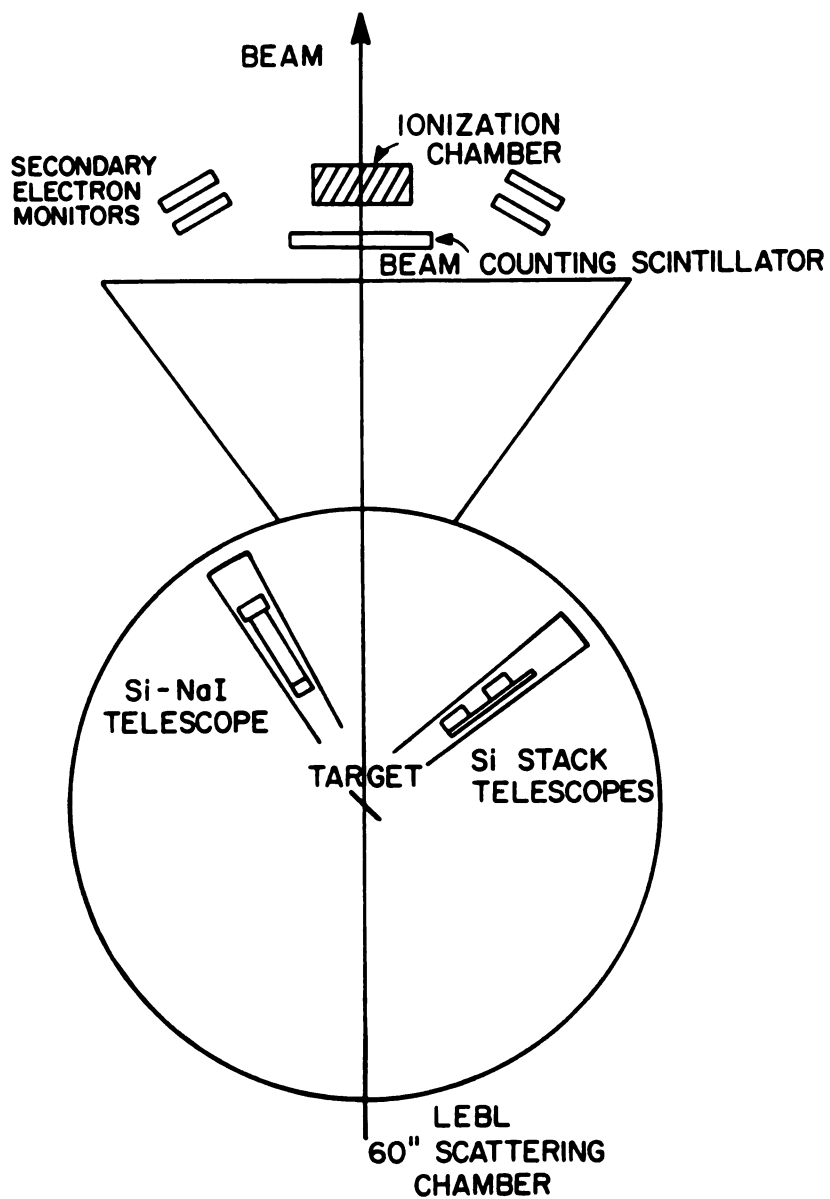


FIGURE II-2. Scattering chamber configuration for measurement of the argon induced reactions.

from the scattering chamber. This was compared to the rate of secondary electron production as the beam traversed the target, measured by pairs of plastic scintillators on either side of the ionization chamber. The procedures agreed to within 5%.

The secondary electron scintillators were also used to monitor the beam centering on the target and their count rates were written to tape, pulse by pulse. The ratio of secondary electrons on the left and right side of the chamber exit was calculated for each beam pulse, and data from pulses differing greatly from the average were rejected during the offline analysis. Several percent of the beam pulses were rejected this way.

The absolute normalization was based on the integrated beam current in the ionization chamber. This was calibrated by lowering the beam intensity such that individual beam particles could be counted in a plastic scintillator directly in front of the ionization chamber (Figure II-2). Comparison with the secondary electron monitors confirmed that the ionization chamber response is not rate dependent, so the energy loss per beam particle determined for low beam intensities can also be used for higher beam intensities. This normalization was compared to the rate of energy loss in the ionization chamber from the expected dE/dx of the beam particles after traversing the 5 mil mylar chamber exit window and the beam counting scintillator. The values agreed to within 20%, and the extracted cross sections for

the 137 and 92 MeV/nucleon beams should be accurate to 20%. In the case of the 42 MeV/ nucleon beam, however, the counting scintillator stopped the beam and had to be removed from the setup. Due to problems with repositioning the monitoring equipment, the absolute cross sections for the 42 MeV/nucleon beam are only known to within a factor of 3.

1. DETECTOR SYSTEMS

a) Si - NaI telescope

Light particles (p,d,t,³He,⁴He and ⁶He) were measured with a ΔE -E telescope consisting of two silicon ΔE detectors, 400 μ m and 5 mm in thickness, backed by a 4 inch NaI E detector. Light particles from 15 to 160 MeV/nucleon were stopped. This telescope subtended 7.2 msr, and was used to measure spectra from 30° to 130°, in 20° steps. Events were accepted by detection of a signal in the second silicon detector.

The energy calibration for the silicon detectors was done by injecting a known amount of charge by means of a chopper pulser in the input stage of the detector preamplifiers and using the measured values of the ionization energy of silicon, $\epsilon=3.67$ eV/ion pair [PE 68]. The NaI detector was calibrated with direct beams of protons and ⁴He at 150 MeV/nucleon, and with these beams degraded to 143, 125, 103, 81, 58 and 35 MeV/nucleon. The energy resolution was approximately 5%. The energy spectra were

corrected for the energy loss in half the target thickness and for the reaction losses of particles in the detectors.

The fraction of reaction loss for protons as a function of proton energy was taken from [ME 69]. This was fitted with the equation

$$\sigma_R = N\pi r^2 (1 - V_c/E)(1 + (\kappa/E)^{1.2}) \quad (\text{II-1})$$

where

$$N = \text{normalization constant} = \begin{cases} 1.1 & \text{Si} \\ 2.0 & \text{NaI} \end{cases}$$

$$r = 1.2(A_1^{1/3} + A_2^{1/3} - 1) \text{ fm}$$

$$V_c = 1.44(Z_1 Z_2 / r) \text{ MeV}$$

$\kappa = 20 \text{ MeV}$ (κ determines the energy at the peak in the cross section)

In order to make the correction, the detector was divided up into slices, and the particle energy in each slice calculated from the entrance energy using range-energy tables. The reaction cross section for each slice was then calculated from equation (II-1), and the reaction probability of a particle was given by integration over the slices

$$f = 1 - \exp\left(-\sum_i n_i \sigma_i\right) \quad (\text{II-2})$$

where

n_i = number of atoms/cm² in cell i

σ_i = average reaction cross section in cell i

This reaction probability was calculated for each energy bin in the spectrum of each particle, and the cross section corrected by the factor $1/(1-f)$. The corrections were approximately 3% for 50 MeV protons, 9% for 100 MeV protons, and 18% for 150 MeV protons.

b) Multi-Si telescopes

For the heavy fragments, from lithium to nitrogen, the detection system consisted of two stacks of silicon detectors: $100\mu\text{m} + 300\mu\text{m} + 5.0\text{ mm}$ and $2 \times 800\mu\text{m} + 3 \times 5.0\text{ mm}$ in thickness. The range of detected fragments in these two telescopes is given in Table II-1. The telescopes subtended 14.0 and 16.0 msr, with opening angles of 7.6° and 8.2° , respectively. Both telescopes were mounted at the same scattering angle, 10° out of plane, and were rotated together to measure spectra from 30° to 130° , in 20° steps. Events in either telescope were accepted upon detection of a signal in the second detector of the stack.

These telescopes were calibrated with the same pulser system as the silicon detectors in the light particle telescope. In addition they were calibrated with a direct beam of ^{20}Ne at 150 MeV/nucleon, and degraded to 137, 115, 93, 68 and 40 MeV/nucleon. The resulting energy calibration is good to 5%. The energy spectra were calculated for each

Table II-1. Energy range of fragments detected in the multi-element silicon telescopes used for the Ar-induced reactions.

Fragment	Thin Si Stack	Thick Si Stack
${}^6\text{Li}$	23 - 240 MeV	80 - 445 MeV
${}^7\text{Li}$	24 - 256 MeV	85 - 480 MeV
${}^8\text{Li}$	26 - 275 MeV	92 - 510 MeV
${}^9\text{Li}$	27 - 288 MeV	96 - 540 MeV
${}^7\text{Be}$	34 - 368 MeV	123 - 689 MeV
${}^9\text{Be}$	38 - 407 MeV	136 - 762 MeV
${}^{10}\text{Be}$	40 - 424 MeV	142 - 795 MeV
${}^{10}\text{B}$	52 - 554 MeV	185 - 900 MeV
${}^{11}\text{B}$	54 - 575 MeV	192 - 1000 MeV
${}^{12}\text{C}$	66 - 708 MeV	236 - 1320 MeV

telescope separately and corrected for the energy loss in half the target thickness. The energy spectra were combined, with the cross sections in the region of overlap of the two telescopes averaged together, weighted by the statistical error.

2. ELECTRONICS

The three telescopes were operated in a parallel fashion; each telescope had its own dead-time circuit, CAMAC bit register and CAMAC analog-to-digital converter (ADC). A block diagram of the electronic configuration for each telescope is shown in Figure II-3. A valid event for any telescope was defined by a signal in the second detector above the threshold in the constant-fraction discriminator. Pile-up rejection circuitry (PUR), with a pulse pair resolution of <100 ns, was used to set a bit in the telescope-dedicated bit register for a good event. Each telescope produced its own ADC gate and interrupt for the CAMAC branch driver of the PDP 11/34 computer.

The live time was determined separately for each telescope by setting a latch whenever a valid event was detected. A coincidence between a valid event and system live signal (as given by the status of the latch) was used to strobe the ADC and bit register, and start the acquisition. The live time was monitored by scaling the number of times each telescope received a valid event and

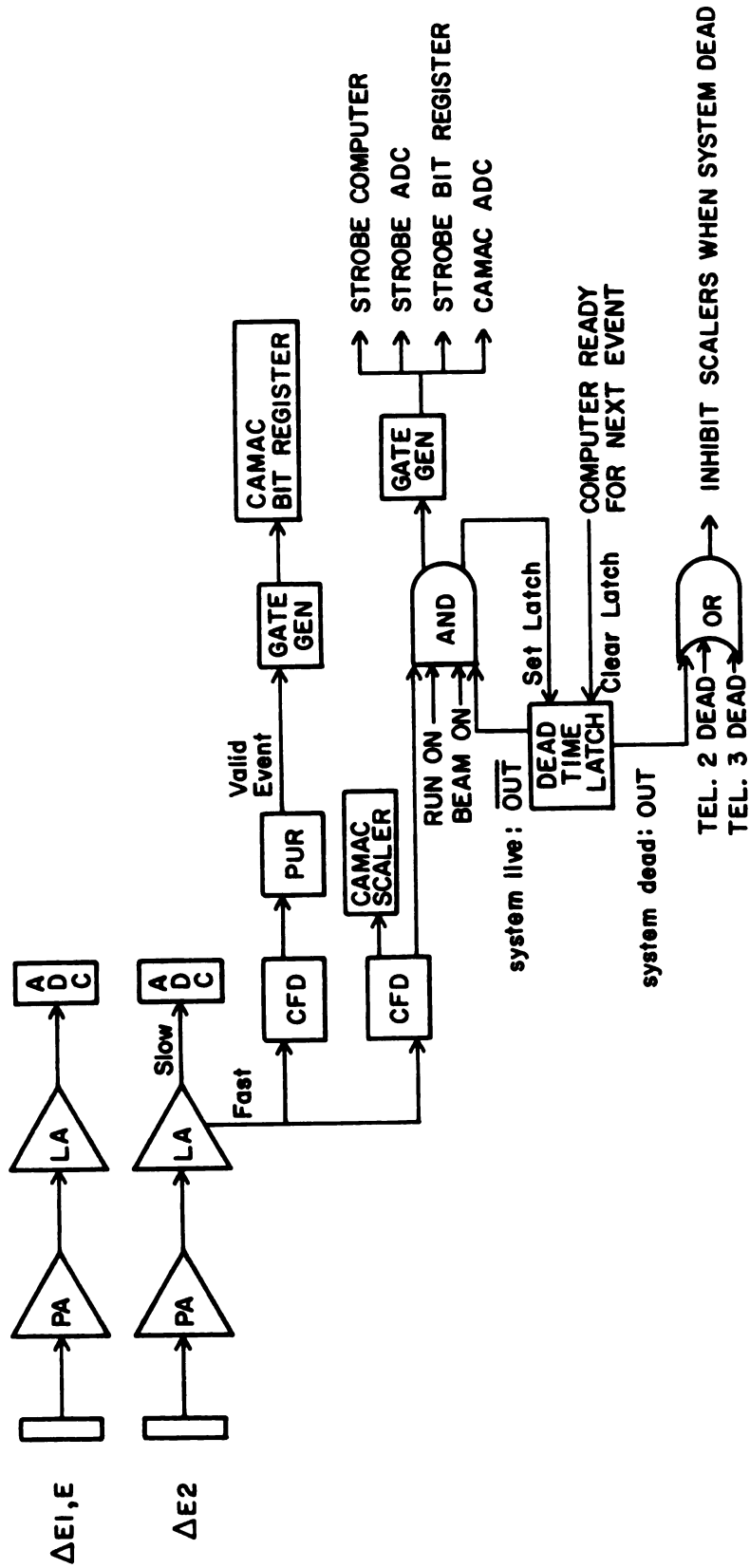


FIGURE II-3. Electronics diagram for measurement of the argon induced reactions.

the number of valid events resulting in interrupts to the branch driver.

3. DATA REDUCTION

The raw data were stored event-by-event on magnetic tape in variable length format. Each event had five header words identifying the event length, run number, event type and sequence numbers. This was followed by the bit register value and the ADC values for each detector in the telescope.

Each neighboring pair of detectors was used to generate a 512x512 channel color density plot of ΔE vs. E . Figure II-4 shows an example of a ΔE vs. E plot for heavy fragments. The figure is a contour plot of pulse heights from the 300 μm silicon detector, shown as ΔE , and the 5mm silicon detector behind it, shown as E . Three isotopes of lithium are clearly seen in this subset of the data, as are three isotopes of beryllium. The beryllium lines are clearly identified due to the absence of a line for ${}^8\text{Be}$. Some data for boron are also visible, however a larger sample of data was displayed to separate the isotopes. Two dimensional gates separating particle types were drawn using a joystick-controlled cursor. The events were analyzed by finding the stopping detector and determining the particle identification by binary search for the enclosing two-dimensional gates. The full resolution ADC values were converted to energies and corrected for energy loss in half the target thickness. Double differential spectra were

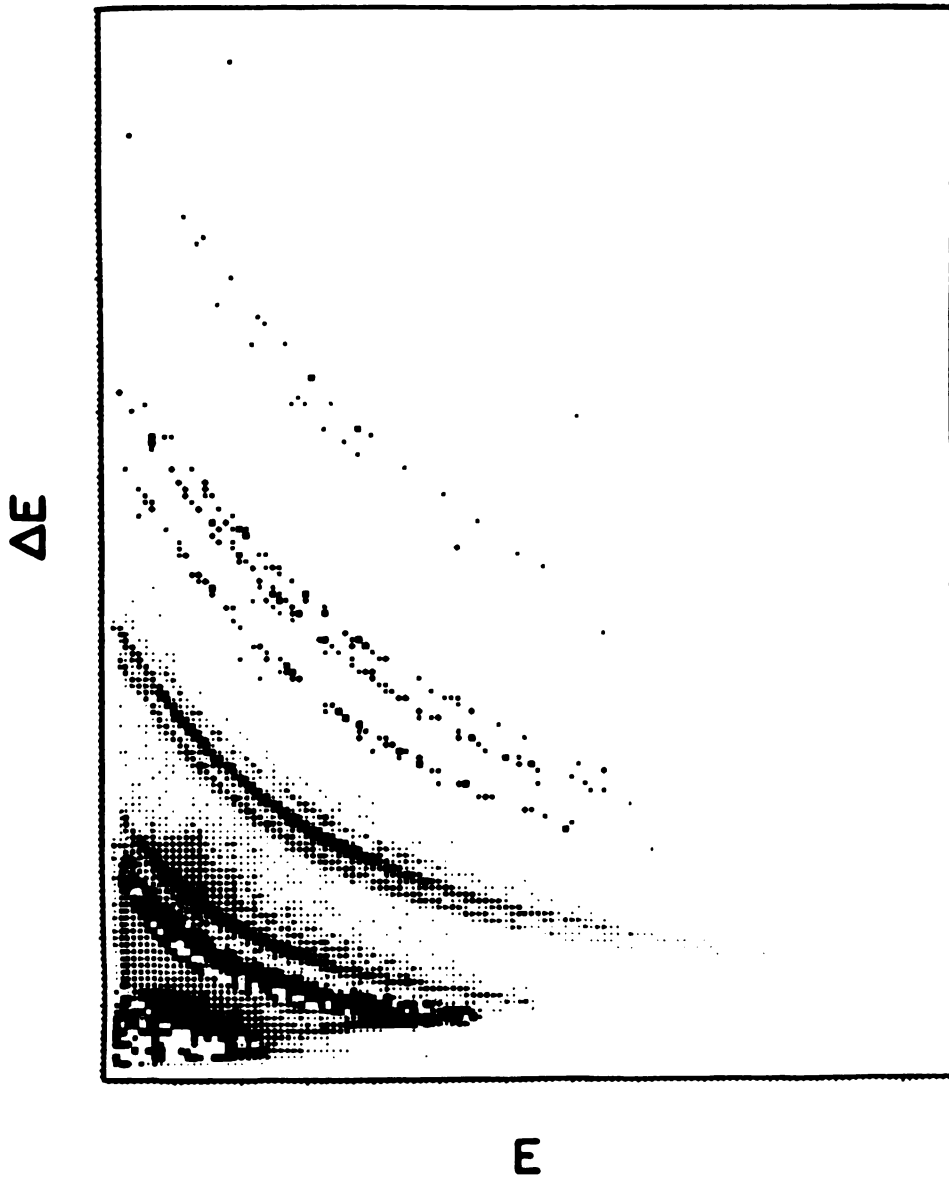


FIGURE II-4. Sample ΔE vs. E contour plot for heavy fragments.

generated by collecting the events into 5 MeV/nucleon bins for light fragments and 15 MeV bins for heavy fragments. The cross sections were generated by using the normalizations described above and correcting for the telescope solid angle and dead time.

B. NEON-INDUCED REACTIONS

The scattering chamber arrangement for the neon-induced reactions is shown in Figure II-5. Aluminum fans were mounted on the two movable arms, and several telescopes were mounted on each fan. The light particles were detected with seven ΔE -E telescopes. Two heavy ion telescopes, each consisting of 5 silicon detectors, were placed at $\pm 10^\circ$ with respect to the beam direction. However, we only report on the light particle measurements.

Two energies of ^{20}Ne were used, 156 MeV/nucleon and 100 MeV/nucleon. The 156 MeV/nucleon beam was used to bombard a 100 mg/cm² Au target, and a 103 mg/cm² Al target. Measurements with the 100 MeV/nucleon beam were done for the Au target only.

The relative normalizations and beam centering monitors were done in the same manner as described above, and the normalizations and energy calibrations checked by comparing the overlapping spectra. The relative normalizations agreed to within 5%, while the energy calibrations for the various types of detectors were good to about 10%. The absolute

MSU-84-223

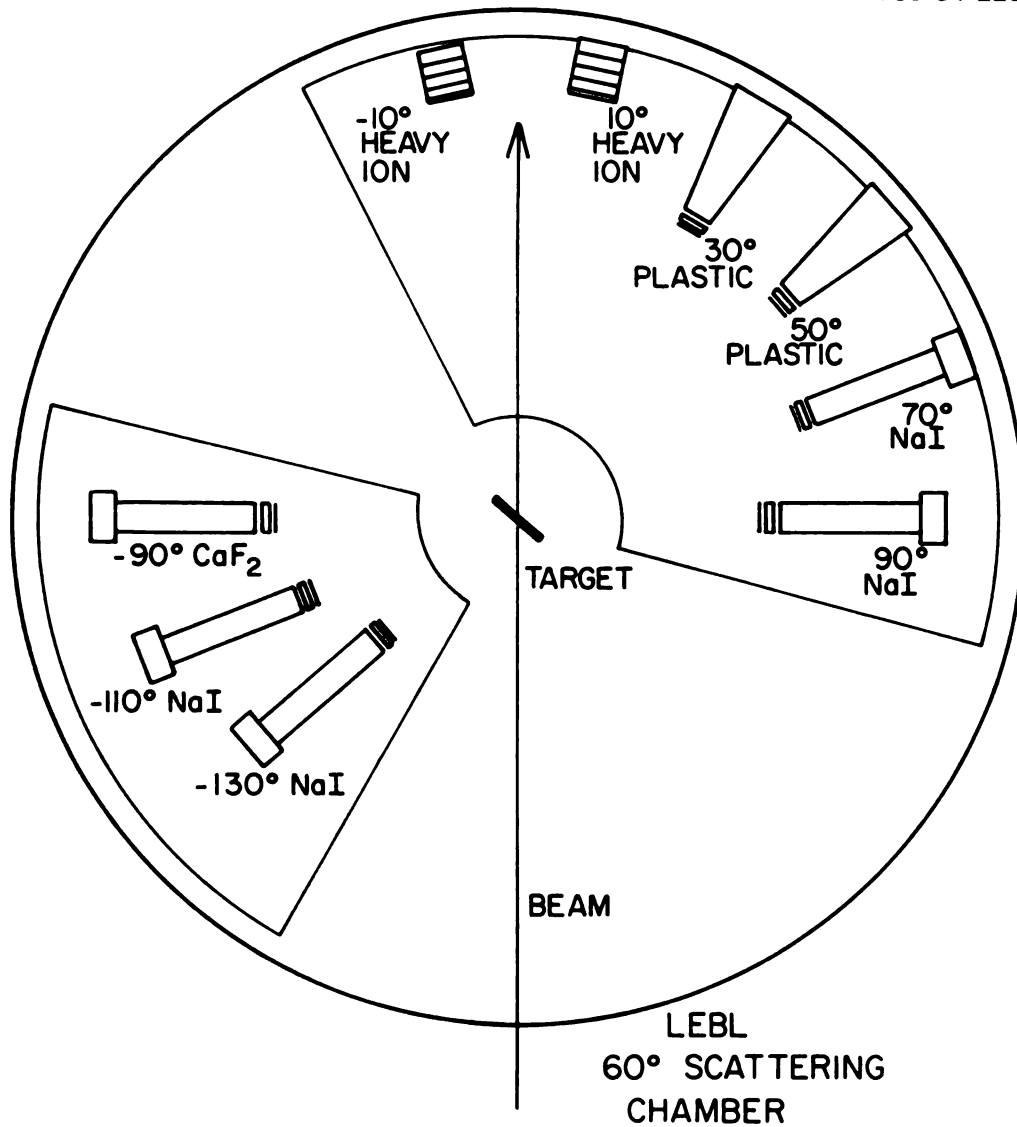


FIGURE II-5. Scattering chamber configuration for measurement of the neon induced reactions.

normalizations were obtained with the ionization chamber, as above, and were accurate to within 25%.

1. DETECTOR SYSTEMS

The seven light particle telescopes were arranged to measure spectra at six angles with respect to the beam direction. Each telescope had two silicon ΔE detectors, 400 μm and 5 mm thick, except at 30° and 50° where the first detector was 800 μm . All silicon detectors were calibrated with the pulser, as described above. The stopping detectors were of three different types: plastic scintillation detectors at 30° and 50°, NaI at 90°, 110°, and 130°, and CaF_2 at 90°. The arms were moved during the experiment by 20° in order to allow overlap spectra among the different types of detectors. A summary of the telescopes, opening angles, and solid angles is given in Table II-2.

The stopping detectors in the light particle telescopes were calibrated with direct beams of protons at 150, 90 and 50 MeV, and with a 150 MeV/nucleon ^4He beam. The calibrations yield overlap spectra among different types of detectors which agree to within 10%. The light particle spectra were corrected for reaction losses in the various detectors using the method described above.

2. ELECTRONICS

The seven telescopes were operated in parallel: a valid singles or coincidence event was allowed to strobe the

Table II-2. Composition, size, highest energy proton stopped, and opening and solid angles for light particle telescopes used for the Ne-induced reactions.

Lab Angle (deg)	Silicon ΔE	E	Max p Energy (MeV)	Opening Angle (deg)	Solid Angle (msr)
30	800 μ m, 5mm	8.0" plastic	176	8.2	16.1
50	800 μ m, 5mm	8.0" plastic	176	8.3	16.4
70	400 μ m, 5mm	3.0" NaI	158	5.3	6.9
90	400 μ m, 5mm	2.0" CaF ₂	138	5.4	6.9
90	400 μ m, 5mm	4.0" NaI	168	3.9	3.6
110	400 μ m, 5mm	2.0" NaI	126	4.6	5.0
130	400 μ m, 5mm	2.0" NaI	126	6.7	10.7

computer. Each telescope had a circuit for prescaling the singles events, however this was only used for the telescopes forward of 70° . For these telescopes every tenth event was accepted. A diagram of the electronics is shown in Figure II-6.

The pulse height from each detector was recorded via a CAMAC ADC, and each telescope with a valid event set a bit in a CAMAC bit register. Any event consisting of coincident particles in two or more telescopes was accepted as a valid event and a common start issued to a bank of CAMAC time-to-digital converters (TDC's). The prompt signal from the constant fraction discriminator of each telescope was delayed and used to stop one channel of the TDC. A strobe to the branch driver was issued whenever a coincidence event was detected, or a valid event in one telescope was accompanied by a signal in the $\Delta E1$ or E detector. When a signal in the $\Delta E2$ detector was not accompanied by $\Delta E1$ or E, the computer was not strobed and front panel fast clear commands were issued to the ADC's, TDC's and bit register.

The system live time was determined by setting a latch whenever a valid event was detected. The busy status of this latch was used to block further ADC strobes, and was cleared when the computer was ready to accept another event or a $\Delta E2$ signal alone was detected. The live time was monitored by scaling the number of times each telescope received a valid event and the number of times the telescope was able to issue a computer interrupt.

MSU-84-374

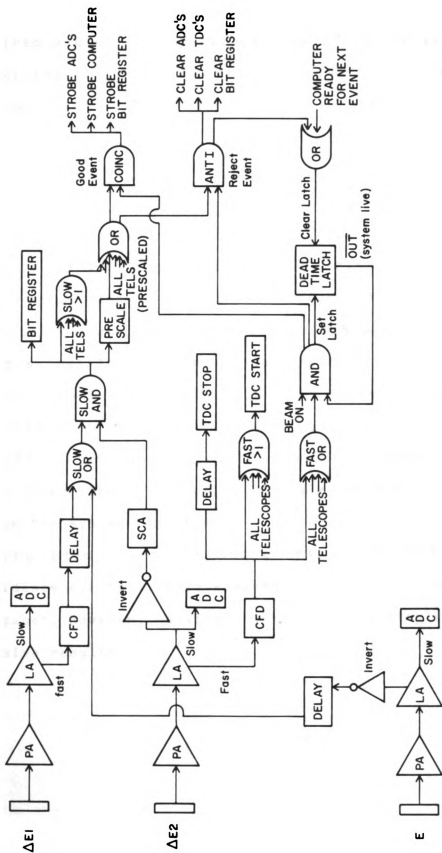


FIGURE II-6. Electronics diagram for measurement of the neon induced reactions.

3. DATA REDUCTION

The raw data were stored in variable-length format, as described above. The particle identification was done by determining the stopping detector and calculating the function [GO 75]

$$\text{PID} = (\Delta E + E)^j - (E)^j \quad (\text{II-3})$$

using the stopping detector to determine E, and the detector before it for ΔE . The exponent j was varied so that a plot of PID values showed vertical peaks for each particle type. The value of j was typically between 1.5 and 2.0. During analysis the PID function was calculated for each event and used to determine the particle type. The energies were determined using the calibrations and reaction loss corrections described above. The cross sections were corrected for the telescope solid angle and prescale factor, and for the system dead time.

The identification and energies of particles in coincidence events were determined in a similar manner. In this paper, however, we will only report the single particle inclusive results.

CHAPTER III

RESULTS

A. DOUBLE DIFFERENTIAL CROSS SECTIONS

Figures III-1 to III-4 show the double differential cross sections of hydrogen and helium isotopes produced in Ar + Au and Ar + Ca at 137, 92 and 42 MeV/nucleon. The spectra consist of measurements taken at 30°, 50°, 70°, 90°, 110° and 130° in the laboratory, with each angle represented by a different symbol. The error bars show statistical errors only. The missing points in the spectra of Fig. III-1 in the region of 20-30 MeV/ nucleon arise from the use of triple element telescopes. Small dead layers in the silicon detectors and the entrance window into the NaI crystal cause nonlinearities. Rather than try to correct for these detection artifacts, we have suppressed the affected energy bins. The slight discontinuities visible in some of the spectra (for example in the deuteron spectra, at 100 MeV/nucleon), are effects of the bin size chosen.

Above 35 MeV/nucleon, the energy spectra decay approximately exponentially with increasing energy. For larger angles the cross sections decrease by several orders of magnitude. A distinct low energy component of quite different slope is visible below 25 MeV/nucleon. The spectra are steeper and the angular distribution is flatter,

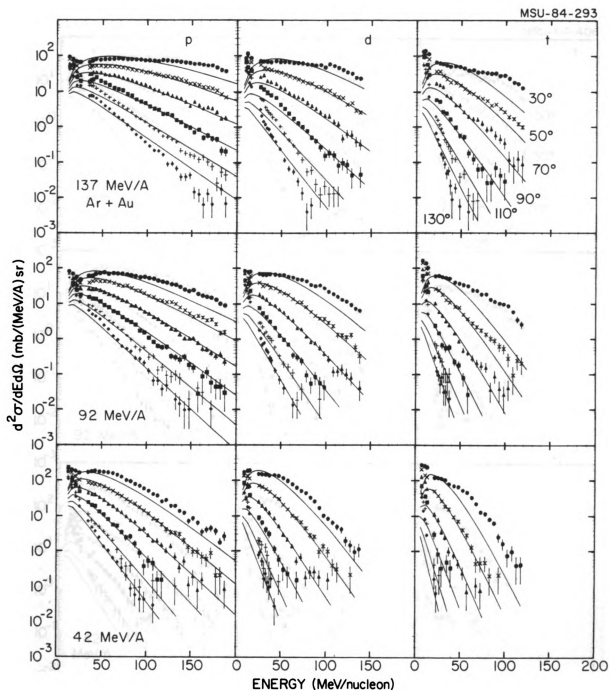


FIGURE III-1. Double differential cross sections for hydrogen isotopes produced in Ar + Au reactions. Data at 30, 50, 70, 90, 110, and 130° are shown for each particle. The solid lines are fits with a single moving source parameterization.

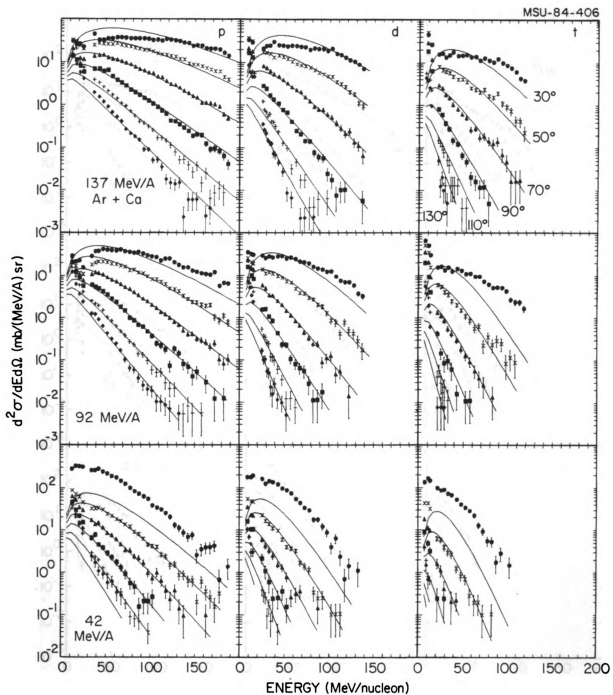


FIGURE III-2. Double differential cross sections for hydrogen isotopes produced in Ar + Ca reactions.

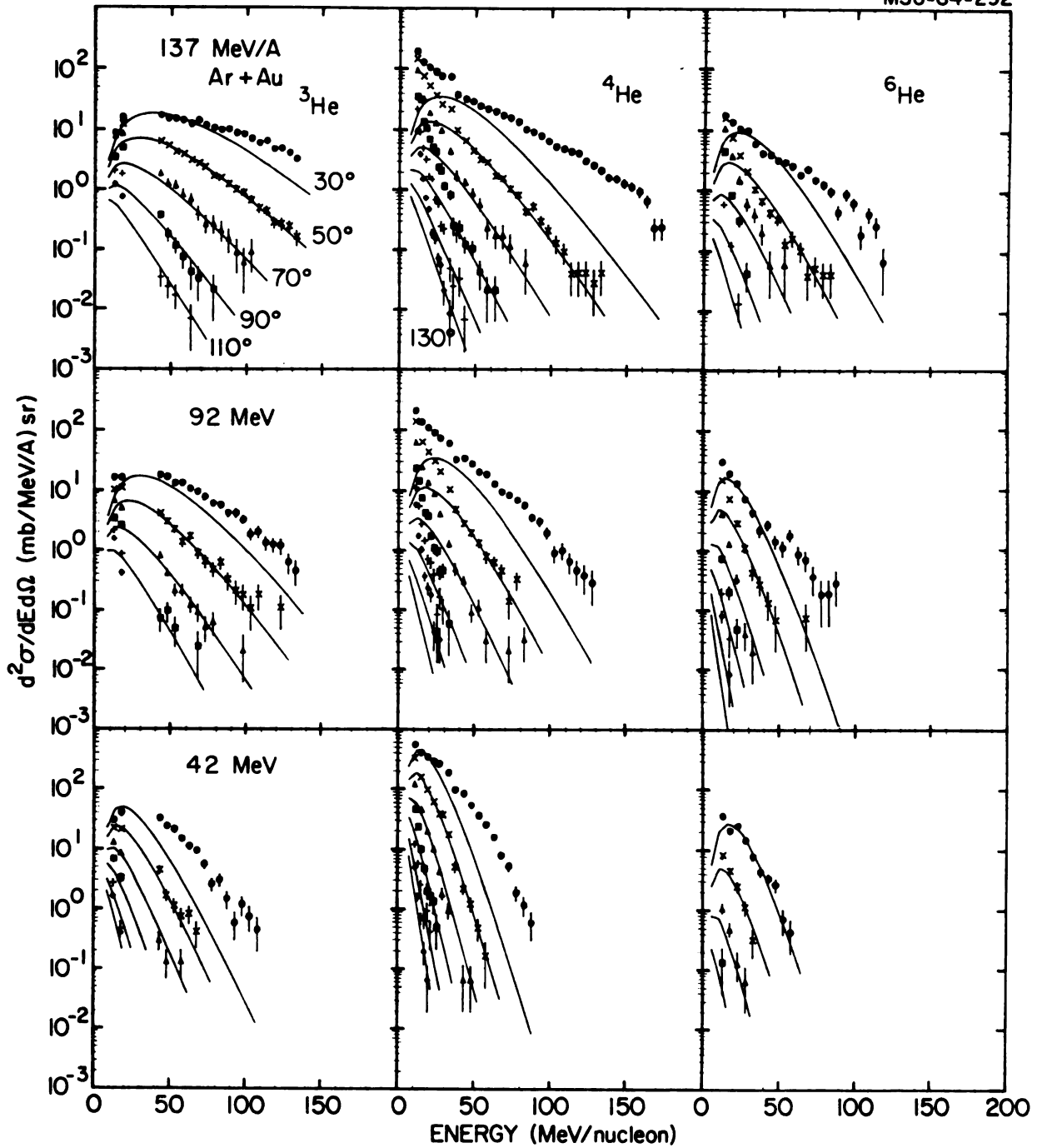


FIGURE III-3. Double differential cross sections for helium isotopes produced in Ar + Au reactions.

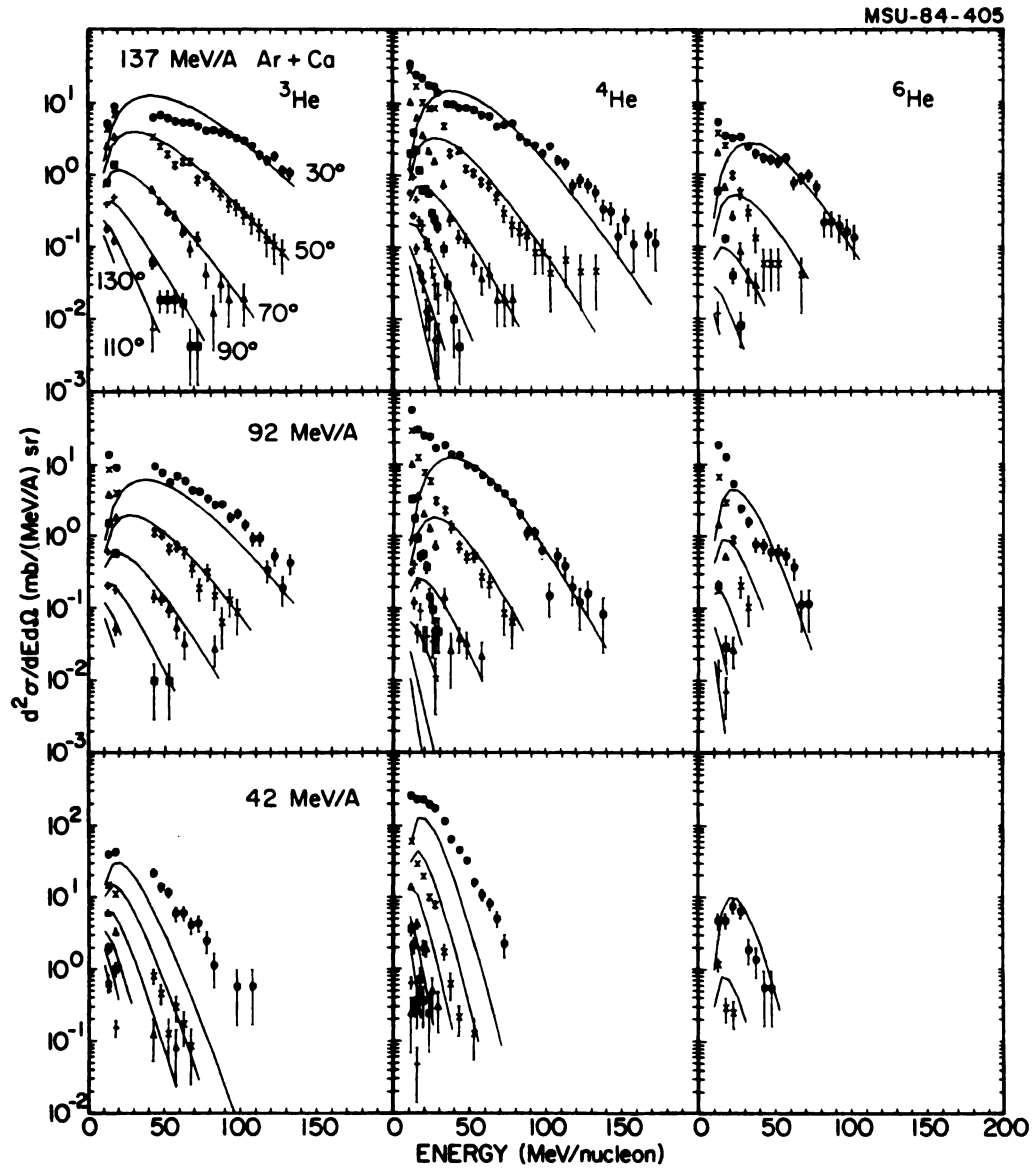


FIGURE III-4. Double differential cross sections for helium isotopes produced in Ar + Ca reactions.

suggesting that these particles are emitted nearly isotropically in the laboratory frame.

The high energy tails become somewhat steeper for heavier particles, and much steeper as the bombarding energy is decreased. The maximum in the double differential cross section does not change rapidly as one goes from 137 to 92 MeV/nucleon bombarding energy. The large cross sections for the 42 MeV/nucleon reaction are uncertain by a factor of 2-3 in the absolute normalization due to difficulties in beam monitoring. Comparison of the low energy part of the spectra shows that the general features, including the slope, do not change with bombarding energy.

Light particles are produced with smaller cross sections in Ar + Ca reactions, with somewhat steeper energy spectra than from Ar + Au at the same bombarding energies. At 42 MeV/nucleon particle emission to 30° is enhanced, possibly due to emission from an excited projectile fragment. This effect is more visible in data from the Ca target because there are fewer nucleons participating in the reaction, and the projectile contribution has a greater effect on the observed spectra. At the higher bombarding energies the projectile fragment moves with a larger velocity and the emitted particles are kinematically focussed to smaller angles.

Measurements of heavier fragments are reported for 30° , 50° , 70° and 90° . Results for Li (Figures III-5 and III-6), Be (Figures III-7 and III-8) and B (Figure III-9) isotopes

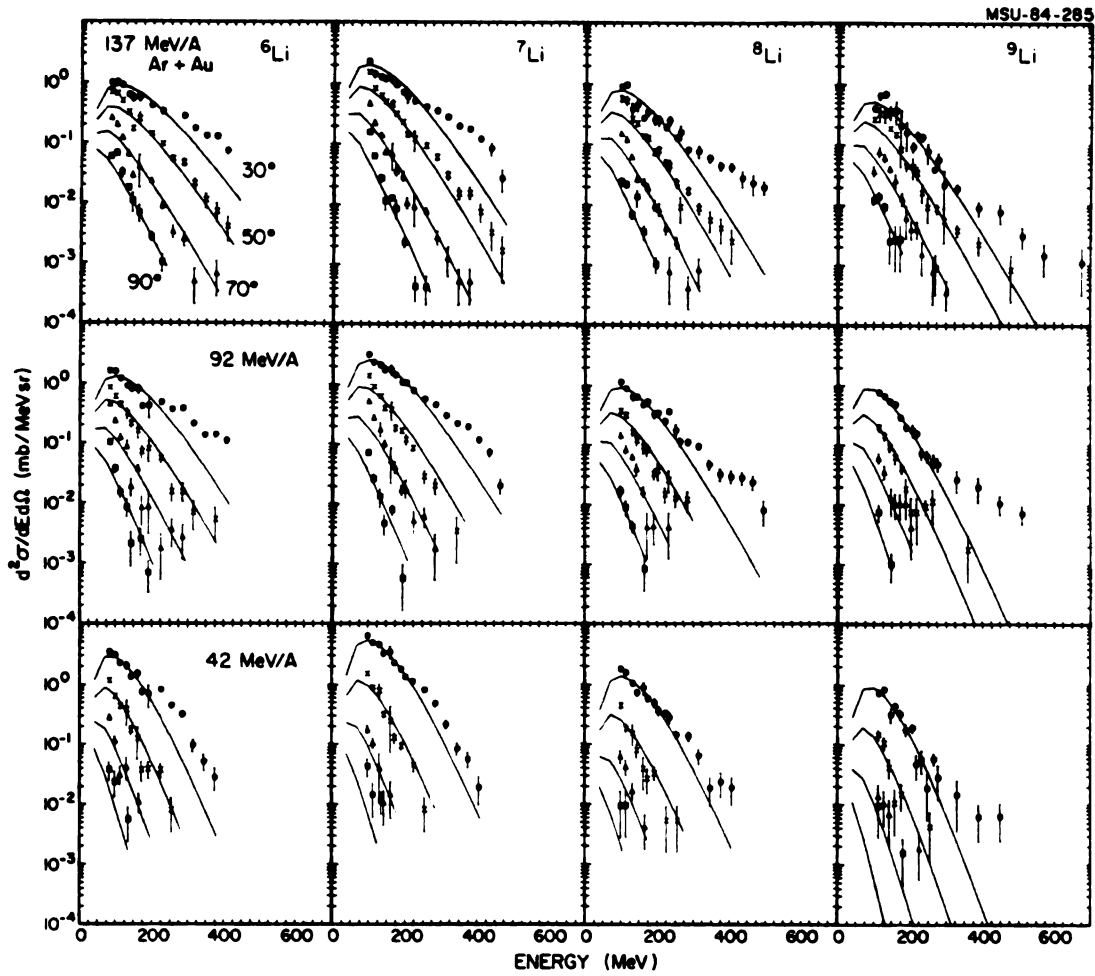


FIGURE III-5. Double differential cross sections for lithium isotopes produced in Ar + Au reactions. Data at 30° , 50° , 70° , and 90° are shown for each particle. The solid lines are fits with a single moving source parameterization.

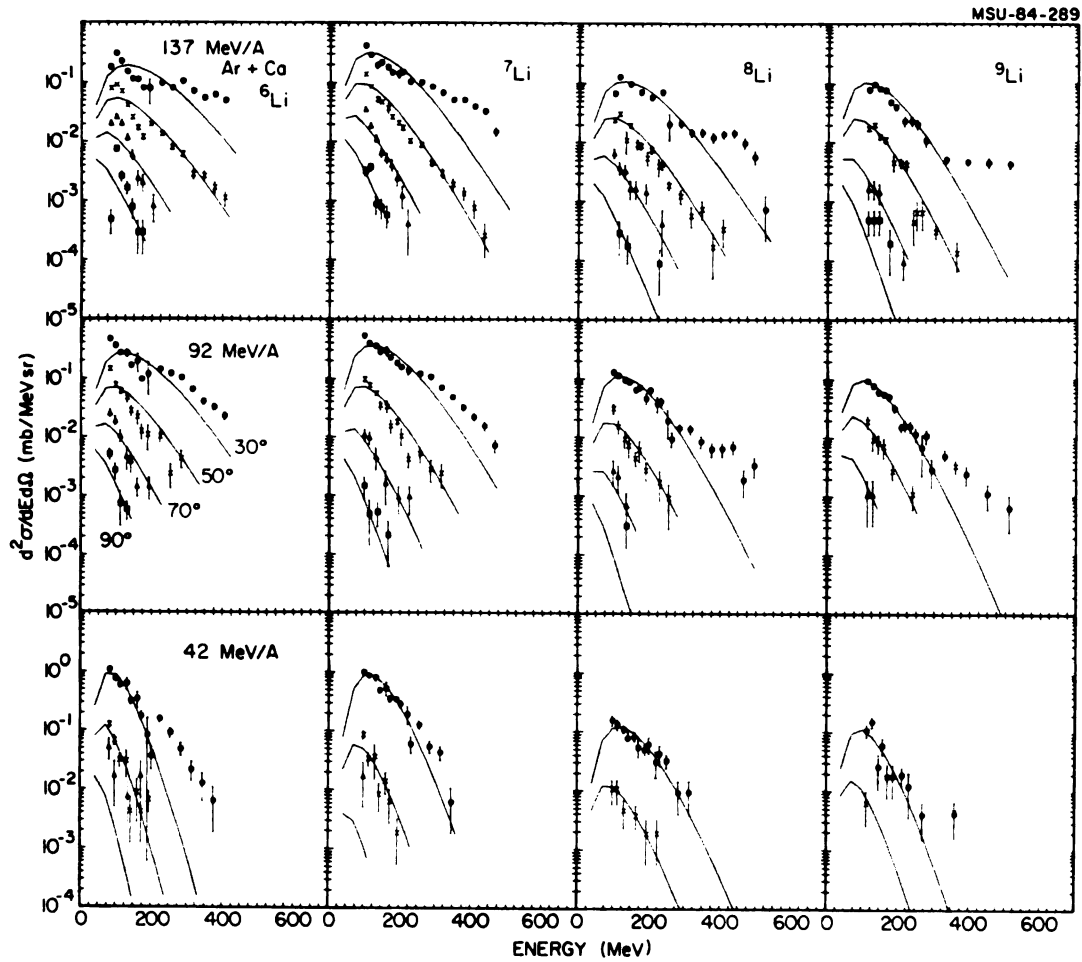


FIGURE III-6. Double differential cross sections for lithium isotopes produced in Ar + Ca reactions.

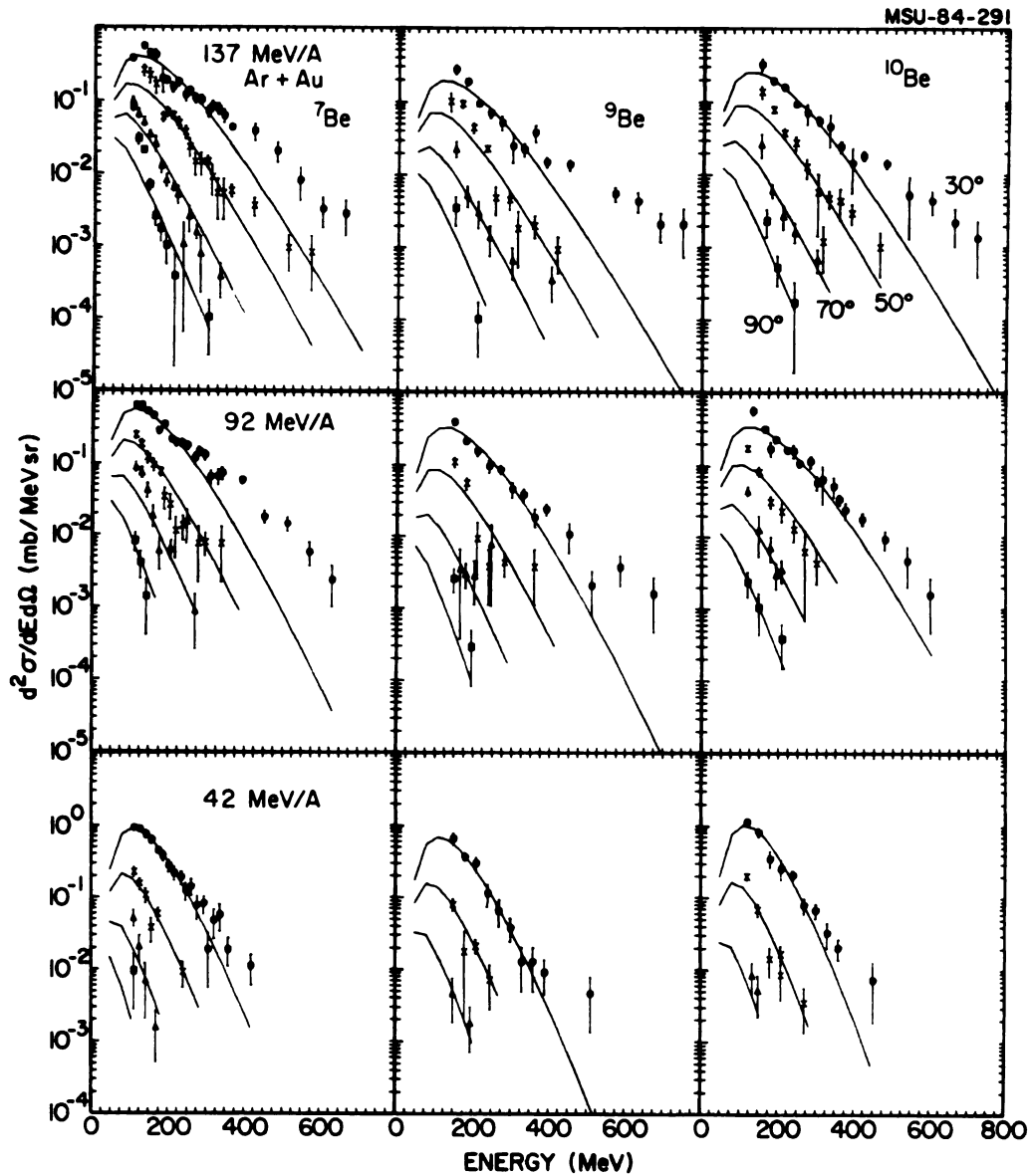


FIGURE III-7. Double differential cross sections for beryllium isotopes produced in Ar + Au reactions.

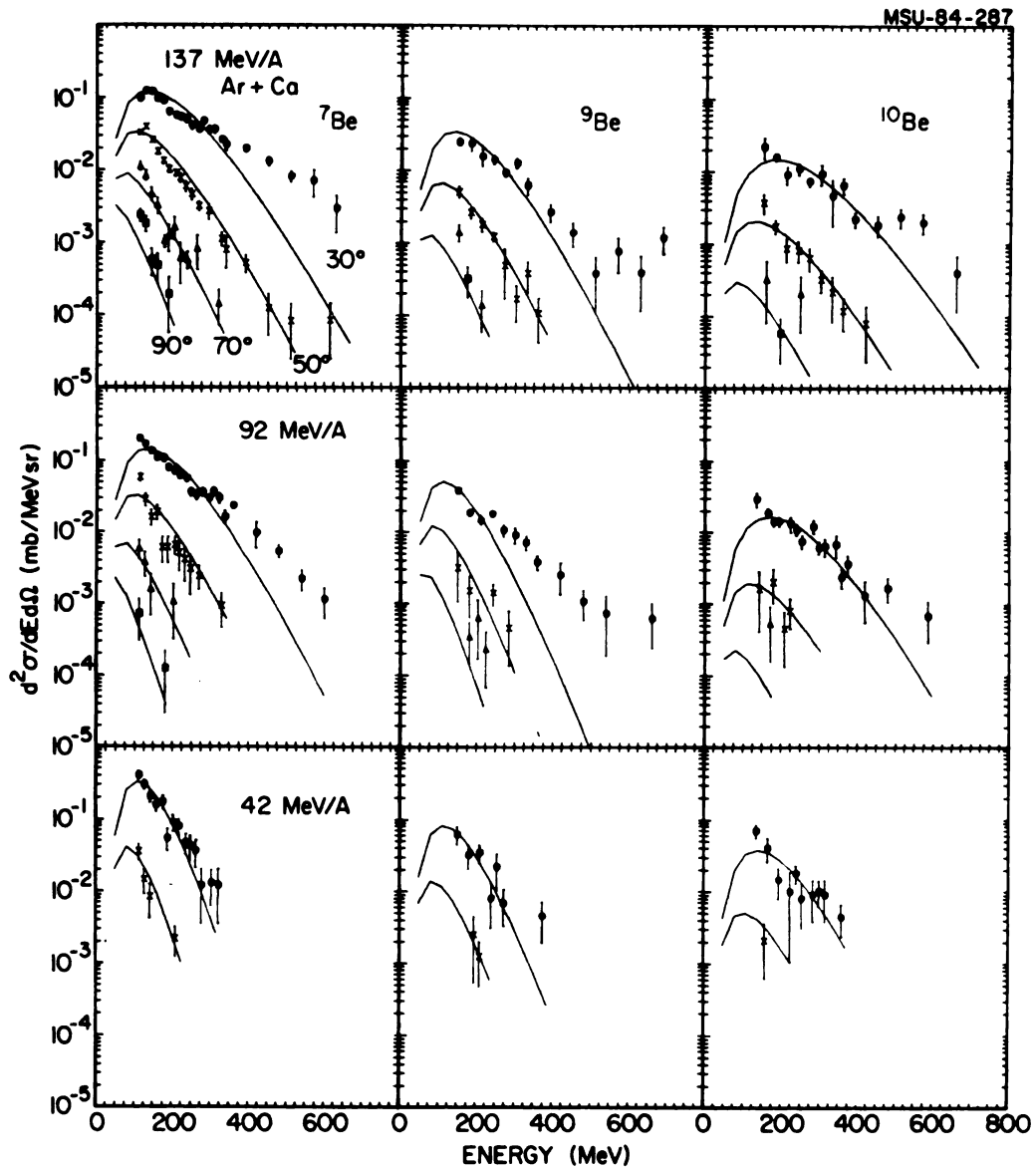


FIGURE III-8. Double differential cross sections for beryllium isotopes produced in Ar + Ca reactions.

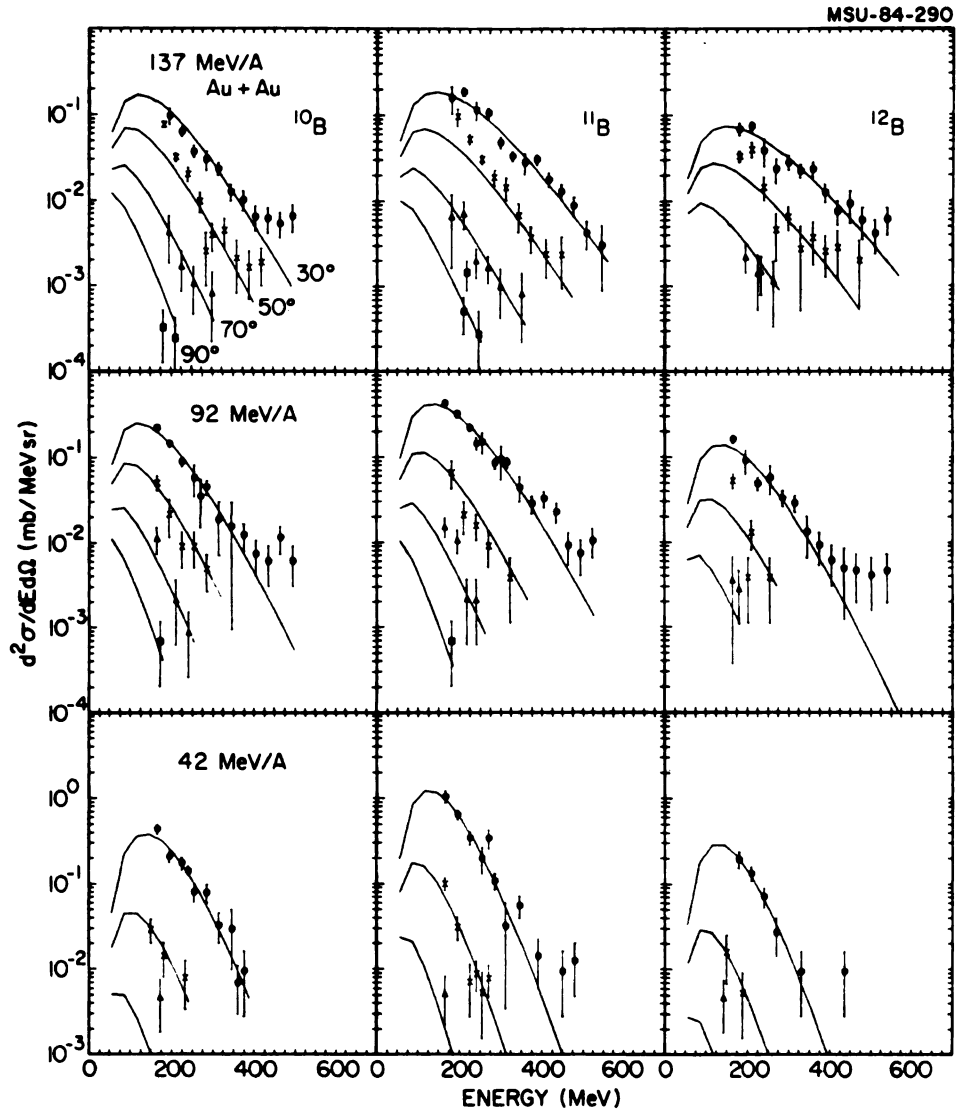


FIGURE III-9. Double differential cross sections for boron isotopes produced in Ar + Au reactions.

are shown for all the beam-target combinations. The energy spectra are shown in MeV, rather than MeV/nucleon to emphasize the spectral details. The error bars depict statistical errors and errors which arise from joining spectra measured by thin and thick silicon telescopes. Figure III-10 shows the isotope-integrated double differential cross sections for carbon and nitrogen fragments from Ar + Au. Isotope-integrated spectra for boron and carbon fragments from Ar + Ca are given in Figure III-11. At all three bombarding energies, the cross sections for these fragments are considerably lower for Ar + Ca than for Ar + Au reactions.

The energy spectra for the heavier fragments show high energy tails which decay exponentially with increasing energy, similar to the light particle spectra. The slopes of these spectra also get steeper as the bombarding energy is decreased. The heavy fragments, however, differ from the light particles in the behavior of the energy spectra at 30° for fragments with $E > 43$ MeV/nucleon. The 30° spectra are much flatter than the spectra at more backward angles. This is observed for both the Au and Ca target, and for all three bombarding energies.

Figures III-12 and III-13 show the double differential cross sections of light particles produced in Ne + Au at 156 and 100 MeV/nucleon and 156 MeV/nucleon Ne + Al, respectively. Spectra were measured at 50° , 70° , 90° , 110° and 130° in the laboratory and are presented for comparison

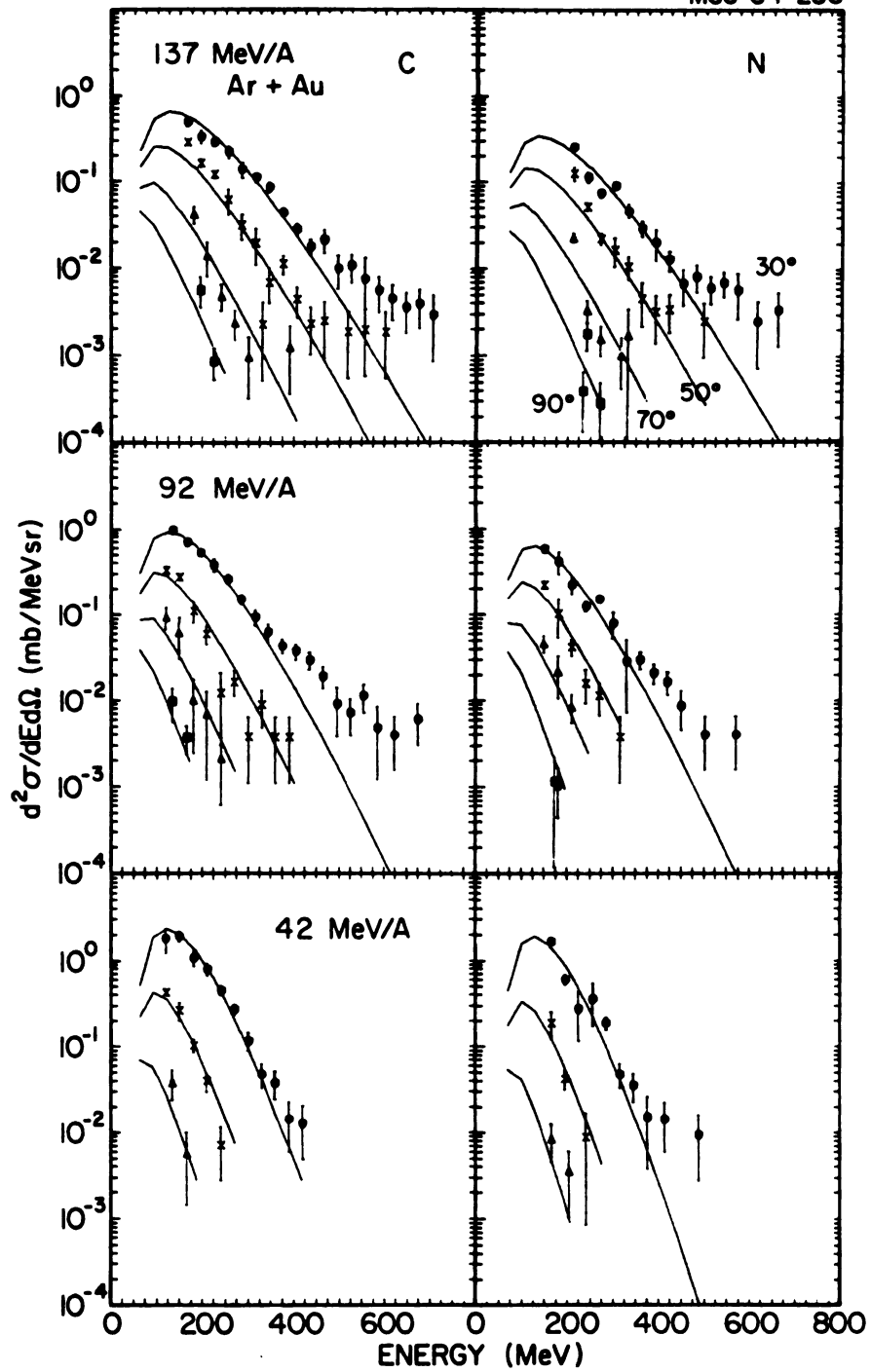


FIGURE III-10. Double differential cross sections for carbon and nitrogen produced in Ar + Au reactions, without isotope separation.

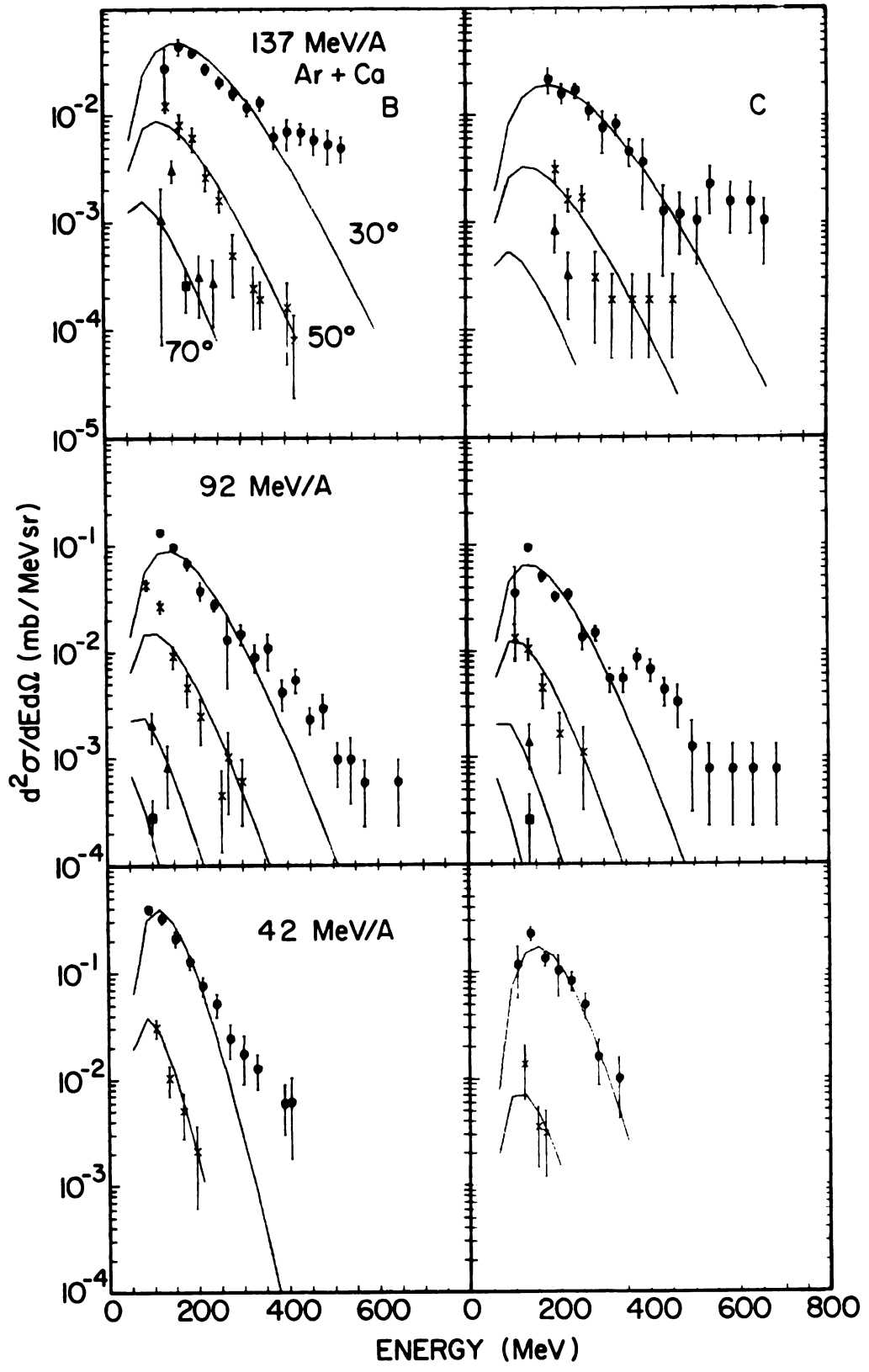


FIGURE III-11. Double differential cross sections for boron and carbon produced in Ar + Ca reactions, without isotope separation.

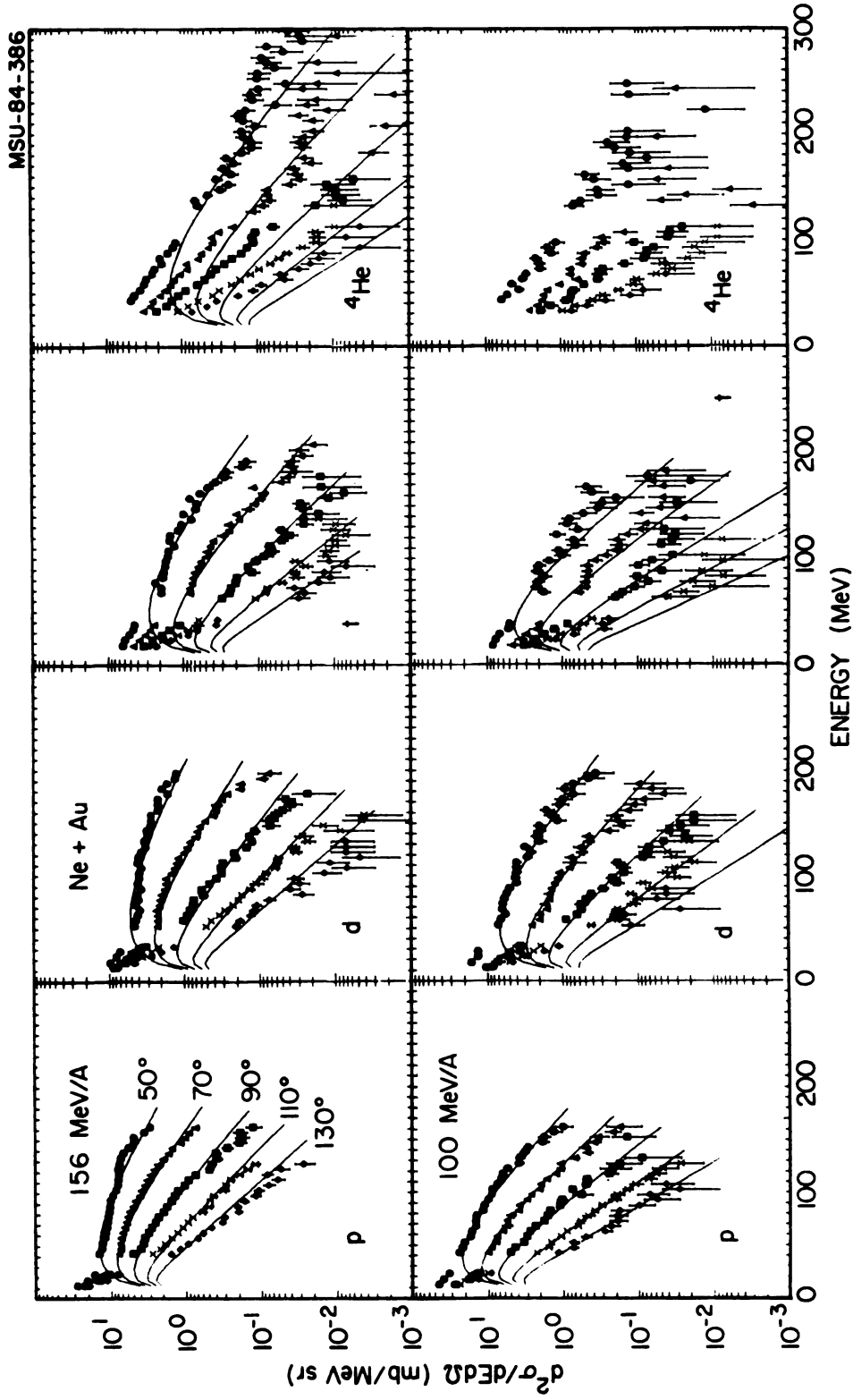


FIGURE III-12. Double differential cross sections for p, d, t, and ${}^4\text{He}$ from Ne + Au reactions. Data at 50, 70, 90, 110, and 130° are shown. The solid lines are fits with a single moving source parameterization.

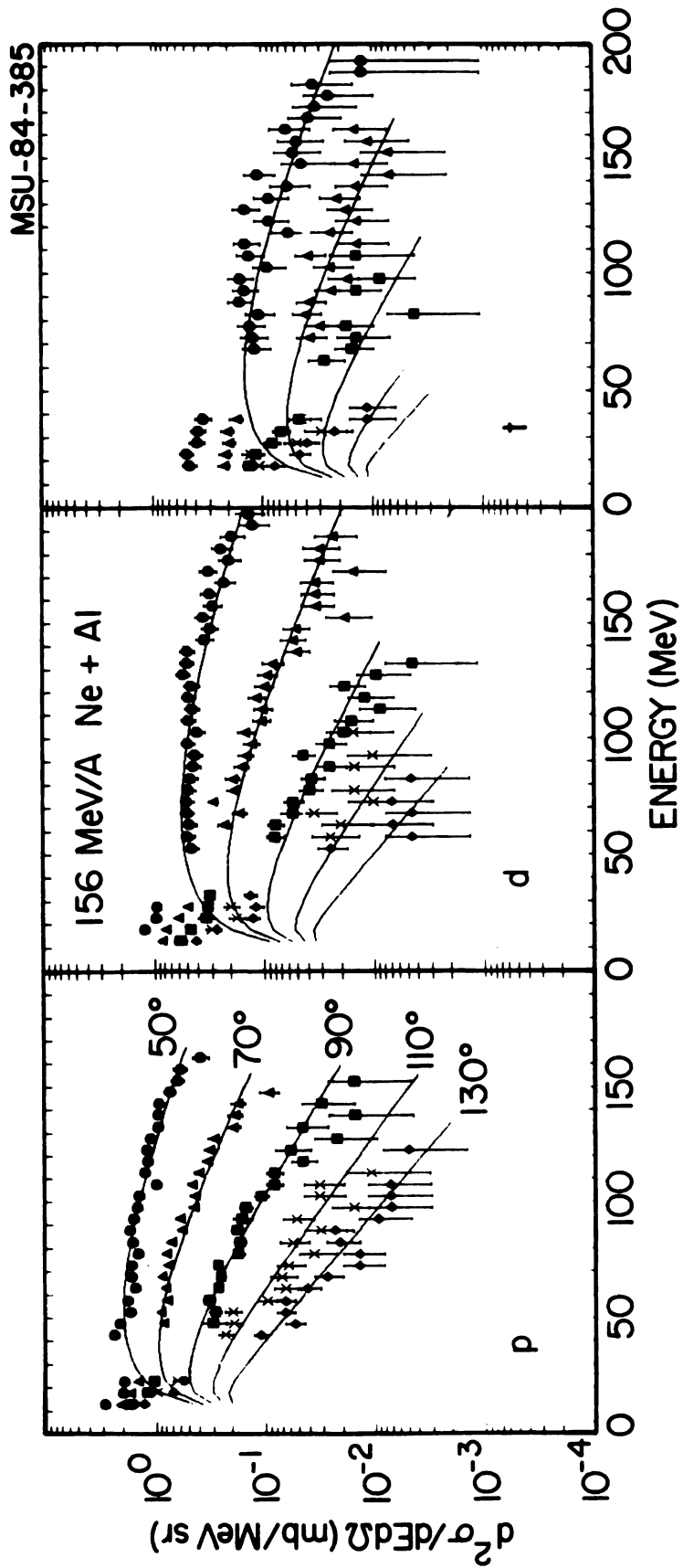


FIGURE III-13. Double differential cross sections for p, d, and t from 156 MeV/A Ne + Al. Data at 50, 70, 90, 110, and 130° are shown for each particle. The solid lines are fits with a single moving source parameterization.

with the data from argon-induced reactions. The general features of the light particle spectra are the same for both projectiles.

B. RAPIDITY PLOTS

The distribution of longitudinal motion can be analyzed in terms of the rapidity variable

$$y = \frac{1}{2} \ln \left[\frac{E + p_{\parallel}}{E - p_{\parallel}} \right] \quad (\text{III-1})$$

where E and p_{\parallel} are the total energy and longitudinal momentum of a particle, and $c = \hbar = 1$. Under Lorentz transformations, the rapidity is shifted by a constant value. The shift is given by the difference in the rapidities of the old and new reference frames:

$$y = \frac{1}{2} \ln \left[\frac{1 + \beta_{\parallel}}{1 - \beta_{\parallel}} \right] \quad (\text{III-2a})$$

as

$$\beta_{\parallel} = \frac{p_{\parallel}}{E} \quad (\text{III-2b})$$

Upon transformation from a frame moving with a velocity β'

$$\beta'' = \frac{54}{1 + \beta\beta'} \quad (\text{III-3})$$

where the rapidity of the moving frame is

$$y' = \frac{1}{2} \ln \left[\frac{1 + \beta'}{1 - \beta'} \right] \quad (\text{III-4})$$

The transformed rapidity is given by

$$y'' = \frac{1}{2} \ln \left[\frac{1 + \frac{\beta + \beta'}{1 + \beta\beta'}}{1 - \frac{\beta + \beta'}{1 + \beta\beta'}} \right] \quad (\text{III-5a})$$

$$= \frac{1}{2} \ln \left[\frac{1 + \beta\beta' + \beta + \beta'}{1 + \beta\beta' - \beta - \beta'} \right] \quad (\text{III-5b})$$

$$= \frac{1}{2} \ln \left[\frac{(1 + \beta)(1 + \beta')}{(1 - \beta)(1 - \beta')} \right] = \frac{1}{2} \ln \left[\frac{1 + \beta}{1 - \beta} \right] + \frac{1}{2} \ln \left[\frac{1 + \beta'}{1 - \beta'} \right] \quad (\text{III-5c})$$

so

$$y'' = y + y' \quad (\text{III-5d})$$

In the non-relativistic limit ($T \ll m$), the rapidity reduces to longitudinal velocity:

$$y = \frac{1}{2} \ln \left[\frac{m + mv_{||}}{m - mv_{||}} \right] = \frac{1}{2} \ln \left[\frac{1 + v_{||}}{1 - v_{||}} \right] \quad (\text{III-6a})$$

so

$$y = \frac{1}{2} \left[v_{\parallel} - (-v_{\parallel}) \right] = v_{\parallel} \quad (\text{III-6b})$$

Contours of constant relativistically invariant cross section $\frac{d^2\sigma}{dp^2} = \frac{1}{p} \frac{d^2\sigma}{dE d\Omega}$ may be plotted in the plane of rapidity versus p_{\perp}/m . In such a contour plot, fragments emitted isotropically from a single source will give contour lines centered around the rapidity of the source. In the non-relativistic limit,

$$y \rightarrow v_{\parallel} \quad (\text{III-7a})$$

$$\frac{p}{m} \rightarrow v_{\perp} \quad (\text{III-7b})$$

In the rest frame of the emitting source the contours are circles if the source emits isotropically. When the plot is drawn in the laboratory reference frame, the circles are simply shifted by the rapidity of the emitting source since y is a scalar under Lorentz transformations. In the extreme relativistic limit, the contours of particles emitted from a single source are no longer circles. The rapidity is given in terms of β_{\parallel} (eqn. III-2a), and

$$\frac{p_{\perp}}{m} = \frac{\beta_{\perp}}{(1-\beta_{\parallel}^2)^{1/2}} \quad (\text{III-8})$$

The resulting contours are triangular about the y -axis and asymptotic to the x -axis, with a discontinuity at $y=0$ in the limit $\beta=1$.

Figure III-14 shows rapidity plots in the laboratory frame for protons produced in the Ar induced reactions for all beam energy - target combinations. The solid curves show the constant cross section contours in y and p_{\perp}/m . There are three evenly spaced contours in each decade of invariant cross section. The projectile and target rapidities are indicated in the figure by arrows. The dashed circle centered about $y=0$ on each plot shows a sample contour expected for protons emitted from the target remnant. The coulomb repulsion of the proton from the target is important in the non-relativistic limit, where $y \approx v_{\parallel} = v \cos \theta$. Including the coulomb contribution to the particle velocity:

$$v' = v + (2V_{CM}/m)^{1/2} \quad (\text{III-9})$$

so

$$y \approx v' \cos \theta \quad \text{and} \quad \frac{p_{\perp}}{m} \approx v' \sin \theta \quad (\text{III-10})$$

resulting in contours which are still circular about the target rapidity. The contours of observed proton cross section are not circles, but are somewhat elongated, indicating contribution from more than one source.

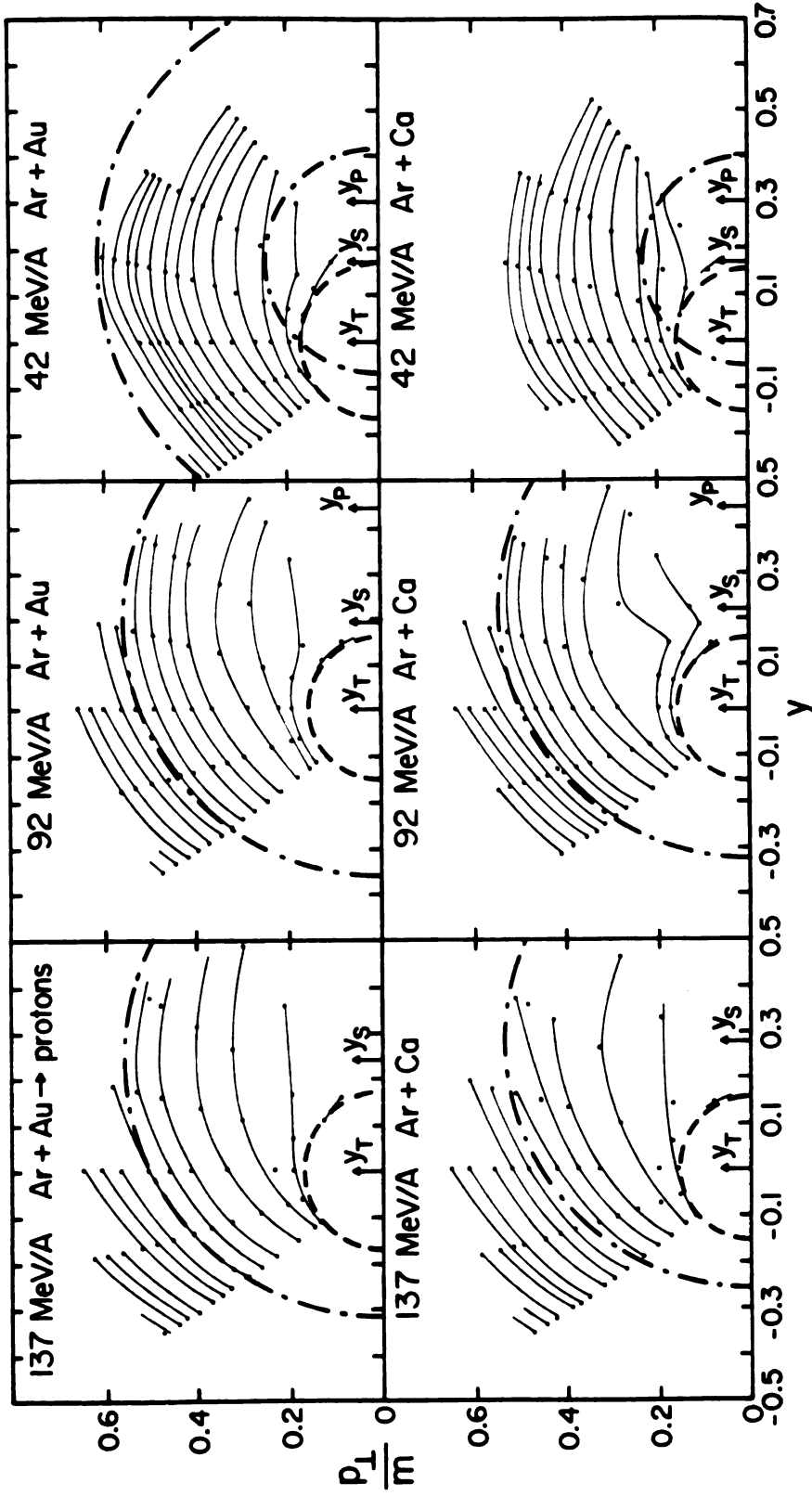


FIGURE III-14. Contours of constant cross section in the rapidity vs. perpendicular momentum plane for protons produced in Ar + Au and Ar + Ca reactions. Dashed semicircles indicate contours expected for emission from a target-like source, and dot-dashed semicircles indicate contours from a midrapidity source.

Comparison of the proton contours with the dashed circles suggests that some protons are emitted from a target-like source. The low cross section contours (corresponding to the high energy tails of the spectra: $E > 35$ MeV) are nearly circular about a rapidity intermediate between the projectile and target rapidities. Each arrow labeled y_s indicates the rapidity of a single source best describing the observed high energy proton distribution. The dot-dashed circle represents a sample contour of protons emitted isotropically from this intermediate source. The outer contours approach this circle, suggesting that one may describe the observed proton spectra by emission from two sources: one target-like source and one intermediate rapidity source.

The contours look quite similar for the two targets even though the magnitudes of the cross sections are different. The contours span a smaller region along the rapidity axis as the bombarding energy is lowered. The projectile rapidity gets smaller, causing the particle sources to become close together and difficult to separate.

The Ar + Ca system is symmetric about the center of mass and thus yields an opportunity to expand the information provided by the rapidity plots. The projectile and target are indistinguishable in the center of mass reference frame and the contours may be reflected about the rapidity of the center of mass. Figure III-15 shows a Lorentz-transformed plot in which $y=0$ corresponds to the center of mass rapidity, and the information given by the

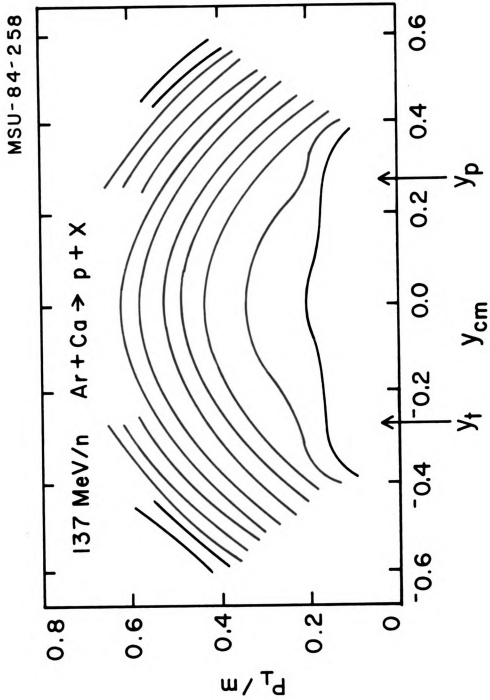


FIGURE III-15. Schematic illustration of a rapidity plot for a symmetric system. The plot is Lorentz transformed into the center of mass frame, and the data reflected through the center of mass rapidity.

data points in the lower left section of Figure III-14 has been reflected through the center of mass rapidity. The contours have been drawn smoothly through the measured and reflected data points, and schematically show the contributions from various sources of particles. Protons from the projectile and target are visible in the contours as bumps centered about the corresponding rapidities. The remaining contours indicate proton emission from a source moving with approximately the center of mass rapidity.

Figure III-16 shows the contours of constant cross section for ${}^4\text{He}$ produced in argon induced reactions, and is analogous to Figure III-14. The ${}^4\text{He}$ fragments also show contributions from a target-like source and an intermediate rapidity source. The rapidity plots for ${}^7\text{Be}$ produced in the Ar + Au and Ar + Ca reactions are presented in Figure III-17 for comparison with the light fragment results. Comparison of the observed contours with the dashed circles for target emission indicates that the ${}^7\text{Be}$ spectra cannot be accounted for by target fragmentation alone. The outer contours approximate the dot-dashed circles from the intermediate rapidity source and show that beryllium fragments arise from an intermediate rapidity as well as target source, similarly to the light particles. We will characterize this source, and use emission from the intermediate rapidity source as a convenient way to parameterize and compare the data for various fragments.

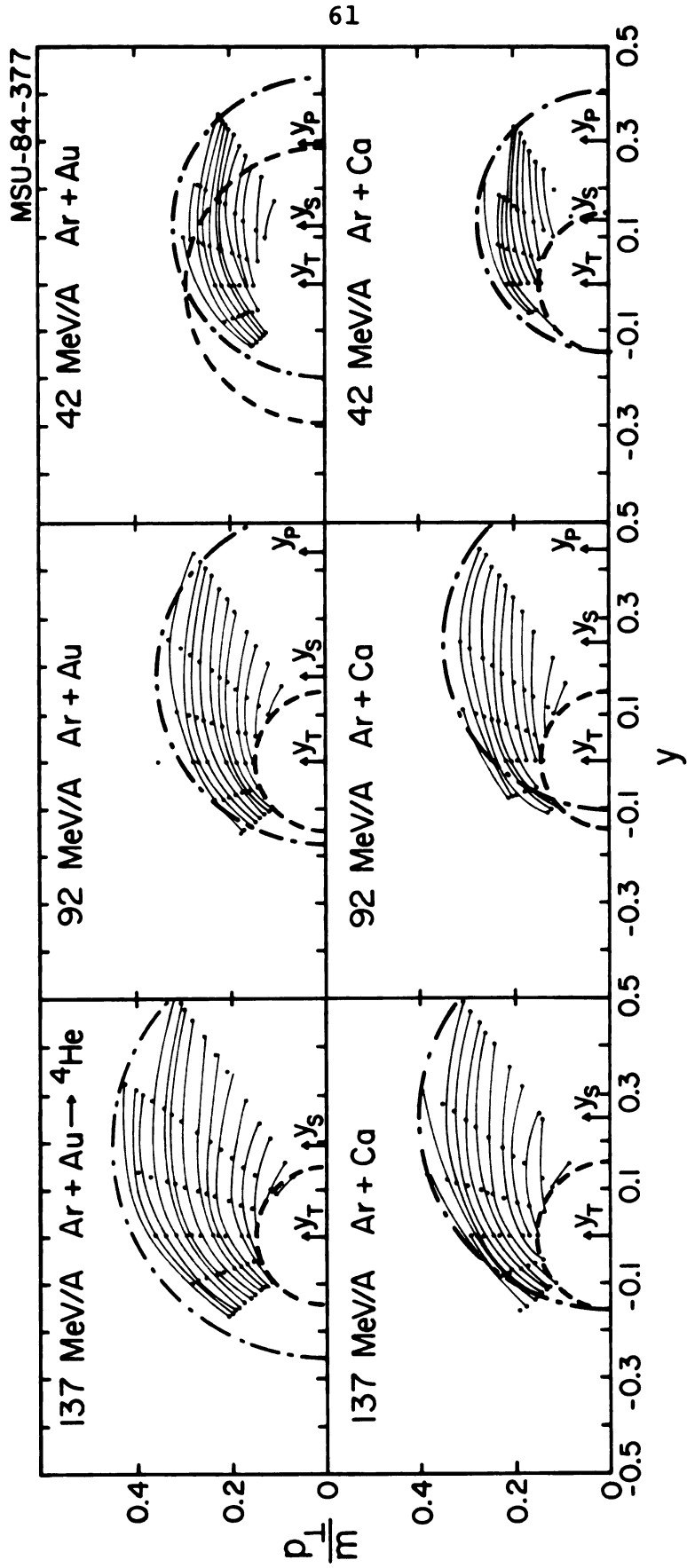


FIGURE III-16. Same as Figure III-14, for ${}^4\text{He}$.

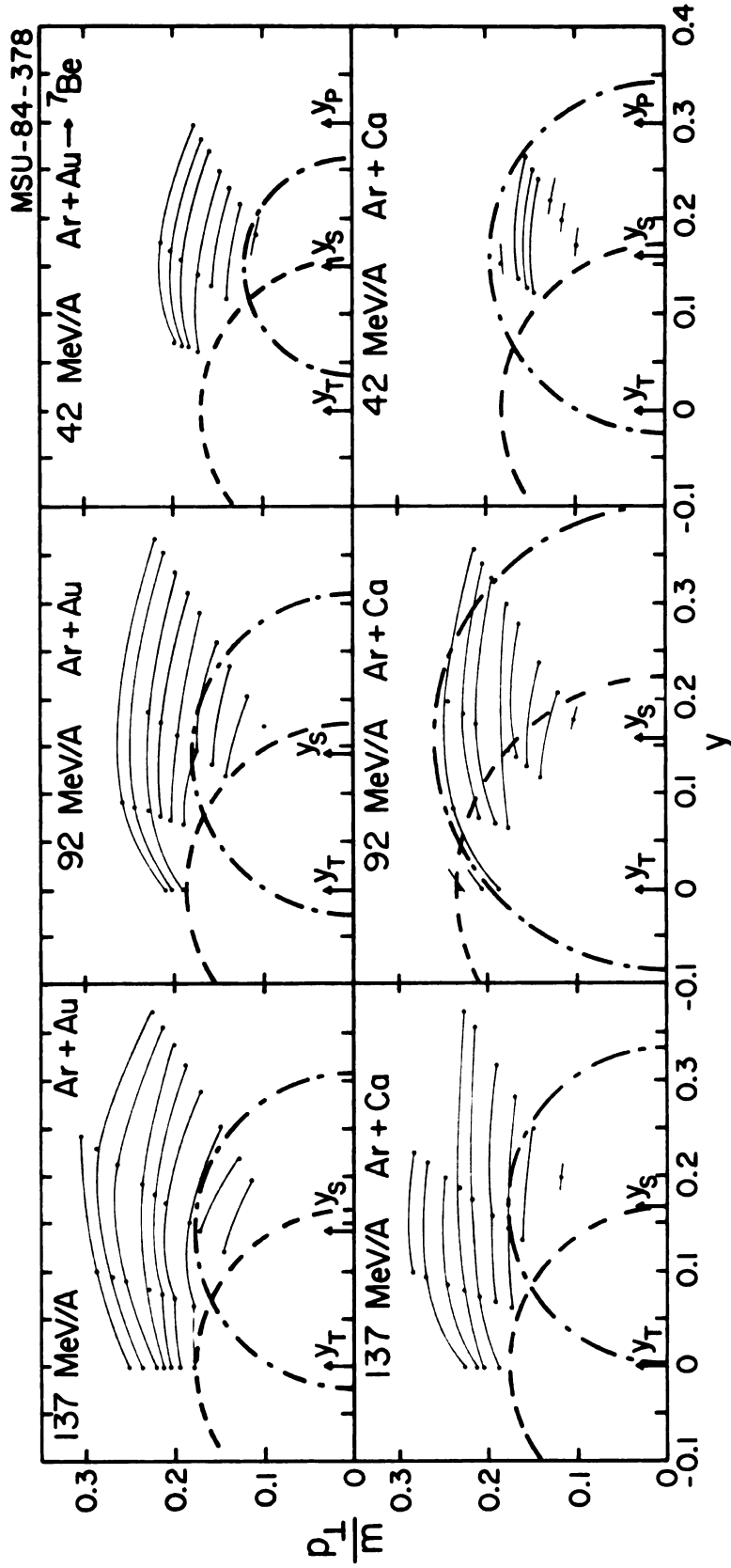


FIGURE III-17. Same as Figure III-14, for ${}^7\text{Be}$.

CHAPTER IV
SINGLE MOVING SOURCE PARAMETERIZATION

A. RATIONALE

The high energy tails ($E > 40$ MeV/nucleon) of the spectra shown in Figures III-1 through III-13 can be rather well described in terms of a Maxwellian distribution observed in a moving frame. Such a distribution would result if the particles were emitted from a thermalized gas of nucleons. The solid lines in these figures show a parameterization of the high energy, exponential region of the spectra in terms of emission from a single, thermalized source. The slopes of the spectra indicate a large excitation energy, and the angular distributions suggest that the source moves in the laboratory frame. This contrasts with the features of the low energy portion of the spectra, where the steeper slopes suggest emission from a cooler region almost stationary in the laboratory frame. Similar spectral shapes and angular distributions in relativistic heavy ion collisions have led to the participant-spectator picture of nuclear collisions [WE 76]. In this approximation, the reaction is described in terms of a highly excited "participant" region consisting of nucleons present in the overlap of the projectile and target, and the cold "spectator" remnants of the target and projectile.

A single source parameterization has been used to characterize emission of nucleons and composite fragments

from the "participant" region [GO 77]. The concept of dividing the reaction (and the resulting energy spectra) into major regions has also been applied for bombarding energies as low as 10-20 MeV/nucleon [AW 81]. The high energy tails of the spectra have been successfully described by emission from a single moving source, and the extracted parameters vary smoothly from 20 to 2000 MeV/nucleon [WE 82].

The moving source parameterization is clearly an oversimplification of the reaction mechanism. Theories describing particle production by knockout [HA 79] or fragmentation [AI 84, AI 84a] processes have also been applied. The concept of the formation of a thermalized subregion has, however, had greater success in describing data over a wide range of bombarding energies and fragment sizes. We therefore use a parameterization based on formation of such a region in order to compare various sets of data and explore the evidence for thermalization.

B. FITTING PROCEDURE

In order to isolate the component of the inclusive spectra originating from an intermediate velocity source, a selection criterion in the spectra was established. Projectile fragments populate forward angles near the projectile velocity, with angular distributions which gradually broaden about 0° for lighter fragments. We therefore associate light particles (p,d,t, ^3He , ^4He and ^6He)

emitted at angles $\geq 50^\circ$ with an intermediate source. Heavier fragments at angles $\geq 30^\circ$ are included in the fits. Target fragmentation leads to low energy particles distributed almost isotropically in the laboratory frame.

Figure IV-1 illustrates the relative contributions of particles from different sources to the inclusive energy spectra. In order to investigate the selection criteria, the sizes of the projectile, target and intermediate sources of protons from 137 MeV/nucleon Ar + Au were estimated using the clean-cut geometry of the fireball model at the most probable impact parameter [WE 76, GO 77, and Chapter V of this work]. The dashed lines show the energy spectra of protons emitted by a source with 30 MeV temperature moving at a velocity 0.45 times the beam velocity. The solid lines show the energy spectra obtained by summing the spectra from the intermediate source with the spectra expected for protons emitted from the projectile and target remnants with temperatures of 8 MeV. It is evident that the inclusive spectra at angles $> 40^\circ$ and $E > 70$ MeV consist primarily of particles emitted from the intermediate source.

We have determined the intermediate source parameters from the large angle, high energy portion of the observed spectra by describing the energy distribution in the source with a relativistic Boltzmann distribution of the form [LI 80]

MSU-83-618

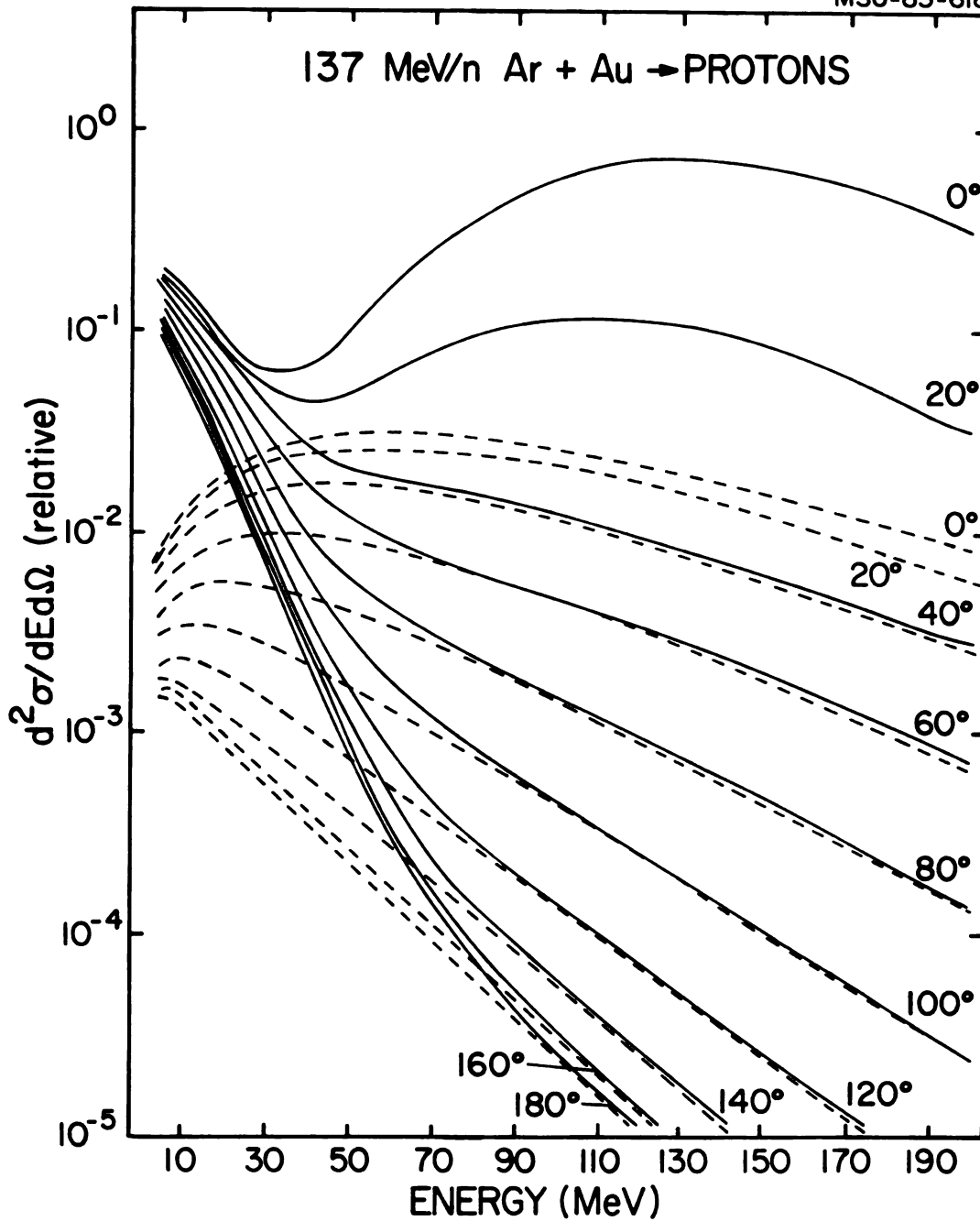


FIGURE IV-1. Proton spectrum for 137 MeV/A Ar + Au, calculated from complete disassembly of the fireball at the most probable impact parameter (dashed lines), and disassembly of the fireball + spectator fragments (solid lines).

$$\frac{d^2\sigma}{p^2 dp d\Omega} = \frac{\sigma_0}{4\pi m^3} \frac{e^{-E/\tau}}{2(\tau/m)^2 K_1(m/\tau) + (\tau/m) K_0(m/\tau)} \quad (\text{IV-1})$$

where p and E are the momentum and total energy of a particle in the source rest frame. The particle mass is given by m , σ_0 is the energy-integrated cross section, and τ is the source temperature. K_0 and K_1 are MacDonalld functions [AB 72]. The nonrelativistic expression corresponding to eqn. IV-1 is

$$\frac{d^2\sigma}{p^2 dp d\Omega} = \sigma_0 (2\pi m \tau)^{-3/2} e^{-(E/T)} \quad (\text{IV-2})$$

We have used the relativistic expression in the calculations presented in this paper.

The distribution is assumed to be isotropic in a frame moving with the velocity, β , in the laboratory frame. The laboratory spectra of particles emitted from the source are obtained by transforming relativistically from the source rest frame to the laboratory using

$$\frac{d^2\sigma}{dE d\Omega} = p E' \frac{d^2\sigma}{p'^2 dp' d\Omega'} \quad (\text{IV-3})$$

where

$$E' = \gamma (E - \beta p \cos \theta_{lab}) \quad (\text{IV-4})$$

and

$$\gamma = 1/(1-\beta^2)^{1/2}$$

(IV-5)

The primed quantities refer to the source frame and the unprimed quantities refer to the laboratory frame. The parameters σ_0 , τ , and β are determined by using a least squares method to fit that part of the measured spectra identified with the intermediate source.

The value of the low energy cut to exclude particles arising from the target was determined by iteratively fitting the data, raising the energy cut until the fit parameters no longer changed. The low energy cutoffs for light particles in experiments reported in this paper are given in Table IV-1. All measured heavy fragments were used for the moving source fits.

A correction for the Coulomb interaction between the observed fragment and the charged emitting region was used in the fitting procedure. In Figures III-5 through III-11, it is clear that the data do not determine the location of the Coulomb peak in the energy spectra. Since we did not measure this quantity, we were forced to estimate it. We assumed that particles are emitted from a subsystem containing the nucleons present in the projectile-target overlap region in a collision at the most probable impact parameter, and that the particles come out late enough in the collision that the emitting system is separated in space from the target remnant. We have further simplified the Coulomb correction by performing it in the laboratory rather

Table IV-1. Low energy cutoffs for moving source fits to spectra.

PARTICLE	AR + AU (MeV)	AR + CA (MeV)	NE + AU (MeV)	NE + AL (MeV)
p	52.5	52.5	37.5	37.5
for 42 MeV/A	52.5	42.5		
d	85	85	42.5	42.5
for 42 MeV/A	85	65		
t	67.5	67.5	42.5	42.5
for 42 MeV/A	67.5		52.5	
³ He	112.5	112.5	57.5	57.5
for 42 MeV/A	52.5	52.5		
⁴ He	150	150	101.5	101.5
for 42 MeV/A	70	70		
⁶ He	135	135	-	-
for 42 MeV/A	135	75		

than in the rest frame of the intermediate source. The correction was applied by shifting the laboratory spectra prior to fitting, and then shifting the calculated spectrum back by the same amount. It is clear that these Coulomb shifts were determined in an oversimplified manner, but we sought only an approximate magnitude as the fits to these data are rather insensitive to small changes in the coulomb shift applied. The shifts used for Ar + Au and Ar + Ca are given in Table IV-2, and the shifts for Ne + Au and Ne + Al in Table IV-3.

We have compared the parameters obtained using our fitting procedure [WE 82] with that used by other authors. These authors [AW 81, FI 84] have used non-relativistic prescriptions for a Maxwellian distribution

$$\frac{d^2\sigma}{dEd\Omega} \propto E^{1/2} e^{-(E/\tau)} \quad (\text{IV-6})$$

for volume emission from the source [GO 78a], and

$$\frac{d^2\sigma}{dEd\Omega} \propto E e^{-(E/\tau)} \quad (\text{IV-7})$$

for surface emission. The parameters agree within error bars in those cases where both fitting prescriptions have been done on the same data set. The effect of the prefactor should be greatest at low ejectile energies; the part of the energy spectrum which we fit does not seem to be very sensitive to it.

Table IV-2. Coulomb shifts used in moving source fits to spectra of particles from Ar-induced reactions.

PARTICLE	AR + AU (MeV)	AR + CA (MeV)
H	10.0	4.5
He	18.0	8.0
Li	25.0	11.2
Be	34.0	14.7
B	40.0	18.0
C	48.0	21.0
N	55.0	24.0

Table IV-3. Coulomb shifts used in moving source fits to spectra of particles from Ne-induced reactions.

PARTICLE	NE + AU (MeV)	NE + AL (MeV)
p	10	10
d	10	10
t	10	10
⁴ He	18	18

C. LIMITATIONS

The best fits with the moving source prescription are shown as the solid lines in Figures III-1 through III-13. For light particles ($1 \leq A \leq 4$) the 30° spectra are consistently underpredicted if emission from a single moving source is assumed. This is because these spectra include substantial contributions from decay of projectile fragments which move with the original beam velocity and are expected to be less excited than the participant matter. The projectile fragment temperature is similar to that of the target fragment, and each emits particles isotropically in its rest frame. When the spectra of light particles emitted from the projectile fragments are transformed to the laboratory frame some are observed at 30° . Because of this, we do not expect single source emission to reproduce the 30° spectra, and do not include these data when determining the parameters.

Projectile fragments heavier than alpha particles result after the primary fragment emits light particles. The angular distribution in the laboratory for such fragments is forward peaked, and emission of such fragments to 30° is kinematically suppressed [HE 78, NA 81a, BO 83a, RA 84]. Due to this, and since the thicknesses of the first detector in the complex fragment telescopes minimized measurement of target remnants, we included all measured data into the fits for fragments heavier than helium. The general trends of the data are consistent with a single

moving source parameterization, although several difficulties are present in fitting the heavier fragments.

The 30° spectra for fragments with $E > 43$ MeV/nucleon are quite flat, and the angular distribution cannot be reproduced with emission from a single source. This effect is observed at all three bombarding energies and for both targets. The same effect is present for boron fragments from 400 MeV/nucleon Ne + U [GO 77]. The fragments at 30° are observed with cross sections ranging from 10^{-1} to 10^{-3} mb/(MeV sr). These cross sections are too large to be explained by the tail in the angular distribution for projectile fragmentation, as the grazing angle is less than 5° for these reactions. It is also unlikely that these are projectile fragments deflected to 30° by the coulomb field of the target. If this were the case, the forward angle spectra should vary for different targets, but the observed cross sections and onset energy of the effect are the same for Au and Ca targets.

In the fits for lithium and heavier fragments, it is difficult to reproduce the energy spectra below 150 MeV. This is reminiscent of the situation encountered with the lighter ejectiles, where the separation from target evaporation was very clear. The heavier fragment spectra do not show an obvious break in slope, but the ability to reproduce the high energy tails with a single source and the difficulty with the low energy fragments suggests that fragment emission may also be a superposition of target and

participant sources. Full characterization of the participant source is difficult due to the limited data at back angles. At 42 MeV/nucleon, the spectra at angles larger than 30 degrees extend less than 200 MeV past the target evaporation region, so the single source can only fit a small fraction of the back angle data. This emphasizes the difficulty in separating the fragment sources at low bombarding energies and the necessity of measuring the particles comprising the tails of the spectra (which are produced with very small cross sections) if one wishes to identify fragments arising from the "participant" zone.

D. DISCUSSION OF PARAMETERS

The values of the three moving source parameters: the temperature, τ , the source velocity, β , and the particle cross sections, σ_0 , are given in Tables IV-4 through IV-6. Results for Ar + Au reactions are in Table IV-4, for Ar + Ca in Table IV-5, and for the Ne-induced reactions in Table IV-6.

The temperature parameter, τ , describes the slopes of the particle spectra. The dependence of the slope on the temperature for particles emitted from a thermalized region can be seen from equation (IV-1); a steeper spectrum corresponds to a lower temperature. Figure IV-2 shows the temperatures extracted from the spectra for each particle observed in the argon-induced reactions [JA 83]. These temperatures are considerably greater than those expected

Table IV-4. Moving source parameters extracted for Ar + Au reactions.

PART.	137 MeV/A AR + AU			92 MeV/A AR + AU			42 MeV/A AR + AU		
	T (MEV)	S (MB)	V/C	T (MEV)	S (MB)	V/C	T (MEV)	S (MB)	V/C
P	30.2	40400	0.24	22.1	26100	0.19	15.5	36800	0.17
d	35.6	19500	0.24	25.7	13800	0.20	17.5	22000	0.18
t	34.2	10100	0.20	24.5	6810	0.17	17.7	12300	0.16
³ He	38.2	3140	0.23	27.3	2100	0.20	17.3	3740	0.13
⁴ He	34.5	4120	0.19	25.1	3050	0.18	15.0	22900	0.12
⁶ He	36.8	820	0.19	22.8	910	0.15	19.1	1540	0.17
⁶ Li	33.5	410	0.14	28.6	500	0.14	19.1	820	0.14
⁷ Li	30.2	810	0.13	28.2	970	0.14	19.1	1640	0.15
⁸ Li	29.0	300	0.12	26.2	330	0.12	19.4	420	0.14
⁹ Li	29.5	200	0.10	21.9	270	0.11	16.3	246	0.12
⁷ Be	34.3	180	0.14	28.0	215	0.14	20.3	280	0.15
⁹ Be	33.3	86	0.13	26.8	130	0.14	21.0	225	0.13
¹⁰ Be	33.2	110	0.13	30.0	150	0.14	17.8	335	0.13
¹⁰ B	32.7	75	0.12	28.0	97	0.12	18.8	150	0.15
¹¹ B	39.1	100	0.13	28.7	180	0.14	18.1	420	0.13
¹² B	42.5	36	0.13	26.0	56	0.13	16.4	110	0.13
C	33.6	240	0.11	27.0	340	0.11	17.7	710	0.12
N	34.8	125	0.10	26.4	220	0.09	16.6	550	0.12

Table IV-5. Moving source parameters extracted for Ar + Ca reactions.

PART.	137 MeV/A Ar + Ca			92 MeV/A Ar + Ca			42 MeV/A Ar + Ca		
	T (MeV)	S (mb)	V/C	T (MeV)	S (mb)	V/C	T (MeV)	S (mb)	V/C
P	27.8	23400	0.27	21.4	14400	0.22	15.5	16100	0.17
d	33.1	9750	0.27	25.2	5840	0.23	16.9	6600	0.17
t	34.1	3260	0.23	24.2	1850	0.19	16.2	2490	0.15
³ He	33.6	2010	0.25	28.8	820	0.23	15.5	2090	0.13
⁴ He	32.0	1870	0.25	25.1	1490	0.25	13.8	6220	0.13
⁶ He	38.7	305	0.24	23.0	280	0.18	17.4	415	0.19
⁶ Li	32.0	77	0.18	27.7	100	0.18	11.8	245	0.15
⁷ Li	28.6	110	0.15	24.4	135	0.17	13.4	320	0.17
⁸ Li	27.9	39	0.16	20.8	38	0.16	17.0	43	0.17
⁹ Li	23.3	32	0.14	20.0	28	0.13	14.1	29	0.13
⁷ Be	30.8	46	0.17	26.1	55	0.16	14.7	91	0.16
⁹ Be	25.6	12	0.16	20.8	15	0.13	18.2	24	0.14
¹⁰ Be	31.4	8	0.18	26.4	9	0.18	22.0	15	0.16
B	28.3	19	0.15	22.1	33	0.14	12.7	105	0.12
C	29.7	9	0.15	21.4	22	0.12	13.6	77	0.15

Table IV-6. Moving source parameters extracted for Ne-induced reactions.

PART.	156 MEV/A NE + AU			100 MEV/A NE + AU			156 MEV/A NE + AL		
	T (MEV)	S (MB)	V/C	T (MEV)	S (MB)	V/C	T (MEV)	S (MB)	V/C
p	32.1	10500	0.24	22.5	11400	0.21	31.5	1650	0.29
d	34.9	4860	0.23	25.6	4780	0.20	34.2	643	0.27
t	26.7	1940	0.16	17.8	1930	0.13	29.9	127	0.19
³ He	25.6	995	0.15	14.2	3690	0.16	-	-	-

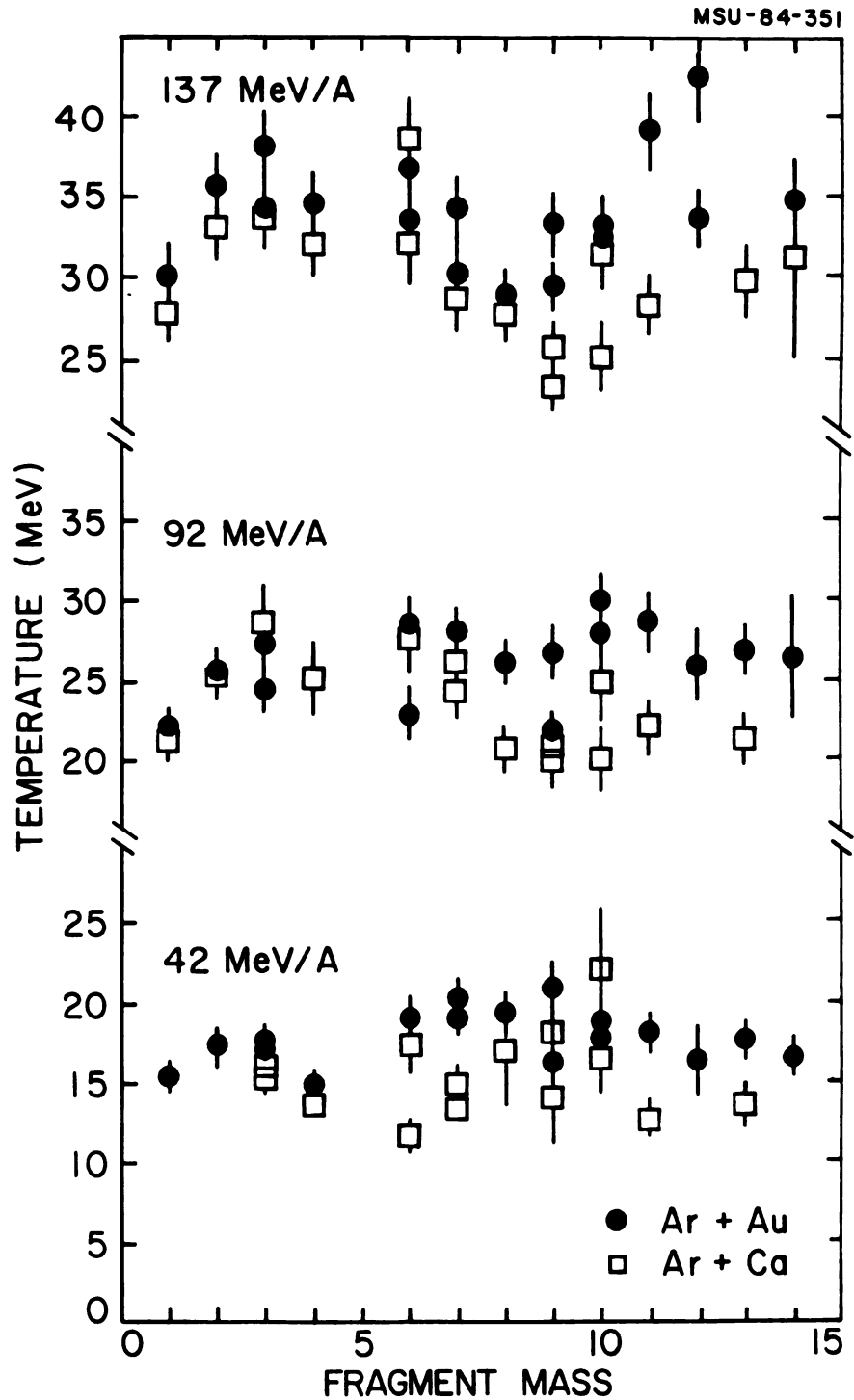


FIGURE IV-2. Temperatures extracted from the spectra of fragments emitted from argon-induced reactions, as a function of the fragment mass.

for a compound nucleus, and increase with bombarding energy: $T(\text{average}) = 18, 25, 35$ MeV for 42, 92, 137 MeV/nucleon Ar + Au. The temperatures for light particles from Ar + Ca are comparable to those from Ar + Au, and the heavier fragment temperatures for Ar + Ca are systematically lower by a few MeV.

The most apparent feature of the figure is the lack of variation of the temperature with fragment mass. The fluctuations in the temperatures from 137 MeV/nucleon reactions may be due to the fact that the heavy fragment telescopes only measured particles to 80 MeV/nucleon, thus sampling only a portion of the intermediate rapidity data. The similarity of the temperature over the measured range of fragment masses suggests that the fragments originate from a thermal source, and that the same type of source gives rise to the heavy and the light fragments. It would be difficult to account for the production of $A=14$ fragments at intermediate rapidity by only a few nucleon-nucleon scatterings; therefore the trends of the temperatures support the idea of thermalization of the emitting system.

Figure IV-3 shows the velocity parameter of the emitting source (expressed as a fraction of the projectile velocity), again plotted as a function of the fragment mass. This parameter depends strongly on the angular distribution of the observed particles, and is the least well-determined of the three parameters. This is particularly true for the

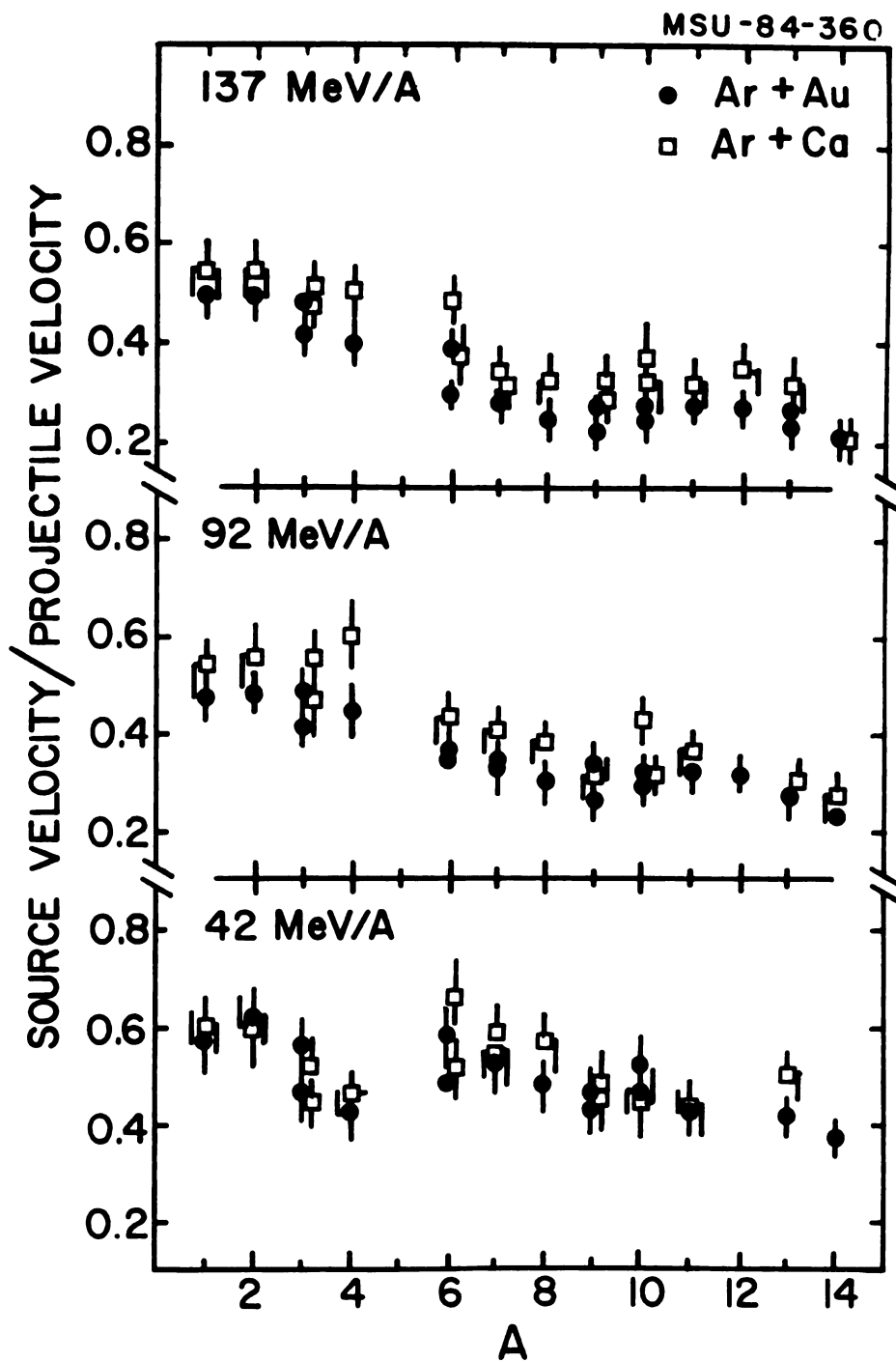


FIGURE IV-3. The ratio of the source velocity extracted from the fragment spectra to the projectile velocity for argon induced reactions, as a function of the fragment mass.

heavy fragments, where spectra at only four angles were measured.

The velocities extracted from the light particle spectra are approximately half the projectile velocity for Ar + Ca, and somewhat lower for Ar + Au. This corresponds to equal numbers of projectile and target nucleons expected in the overlap region for Ar + Ca collisions, and to the excess of target nucleons in Ar + Au. As the fragment mass increases, the velocity decreases, possibly due to limitations in the measured angular distribution. It is, however, likely that the lower velocity reflects a more central collision. In such a collision, a larger thermal system would be created, with enough nucleons to emit a heavy fragment, and with a lower velocity in the laboratory due to a higher fraction of target nucleons.

The third parameter, σ_0 , is the integrated cross section for each type of particle. This cross section results from the integration of the moving source fit, and focusses on emission from the intermediate rapidity source, excluding particles originating from the projectile and target. Figures IV-4 and IV-5 show the values of these parameters as a function of the fragment mass for Ar + Au and Ar + Ca reactions, respectively. The cross sections fall approximately exponentially with fragment mass and the distribution becomes slightly steeper as the bombarding energy is increased. Similar fragment distributions from high energy proton and heavy ion - induced reactions have

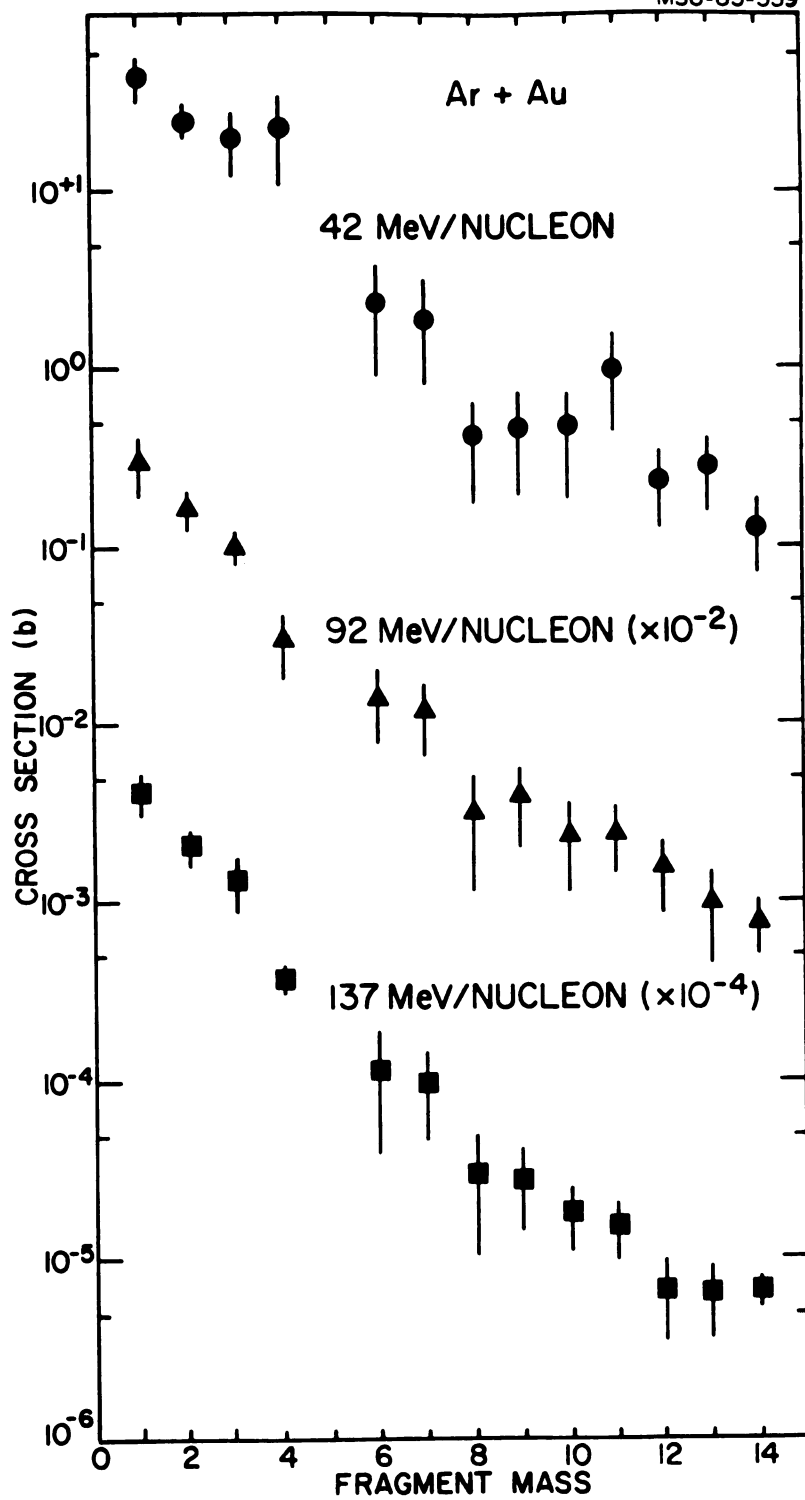


FIGURE IV-4. The integrated fragment production cross sections for Ar + Au, as a function of the fragment mass.

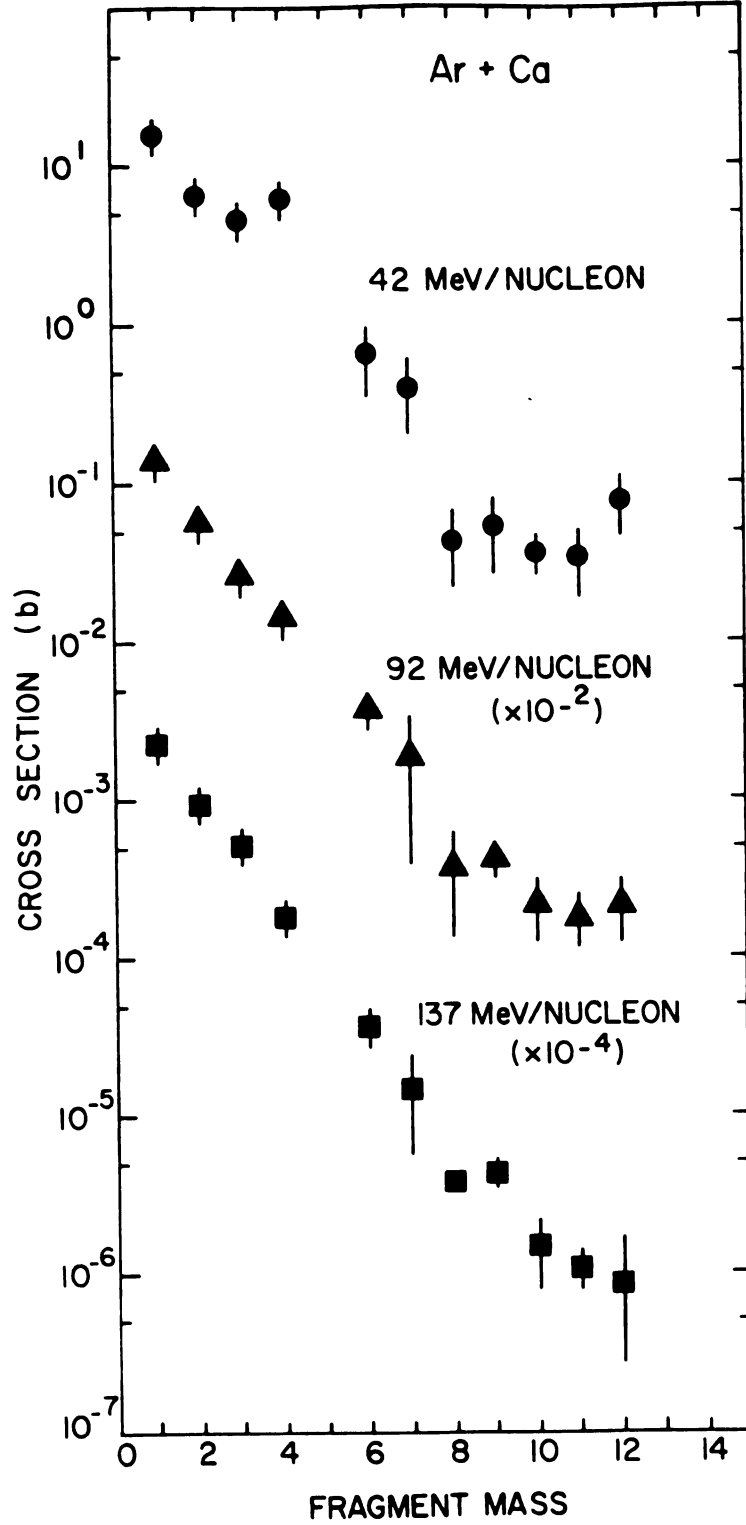


FIGURE IV-5. The integrated fragment production cross sections for Ar + Ca, as a function of the fragment mass.

been described with a power law dependence on the mass number of the emitted fragment [FI 82, PA 84].

The fragment distributions resulting from integration of the measured spectra (extrapolated to all energies and angles) look approximately the same as shown in Figures IV-4 and IV-5. The error bars in the figures reflect the differences between the integrated single source cross section and the extrapolation of the measured spectra.

Figure IV-6 provides a comparison of fragment production for the different targets and bombarding energies. The cross section ratios of composite fragments and protons are plotted up to ${}^9\text{Li}$. These ratios fall with increasing fragment mass, but exhibit an enhancement at ${}^4\text{He}$ due to its large binding energy. This enhancement is prominent at 42 MeV/nucleon, where the excitation energy of the system is relatively low, and one might expect many alpha clusters to coexist with free nucleons. The shapes of the distributions are very similar for both the gold and calcium targets, with the formation of composites slightly less probable in Ar + Ca reactions.

In Figure IV-7, the projectile dependence of the extracted source parameters is presented. Reactions of neon and argon projectiles with gold targets at approximately the same bombarding energies are compared. The temperatures and velocities describing the triton and ${}^4\text{He}$ spectra are roughly comparable to the proton and deuteron parameters in the case of argon-induced reactions, but fall with increasing

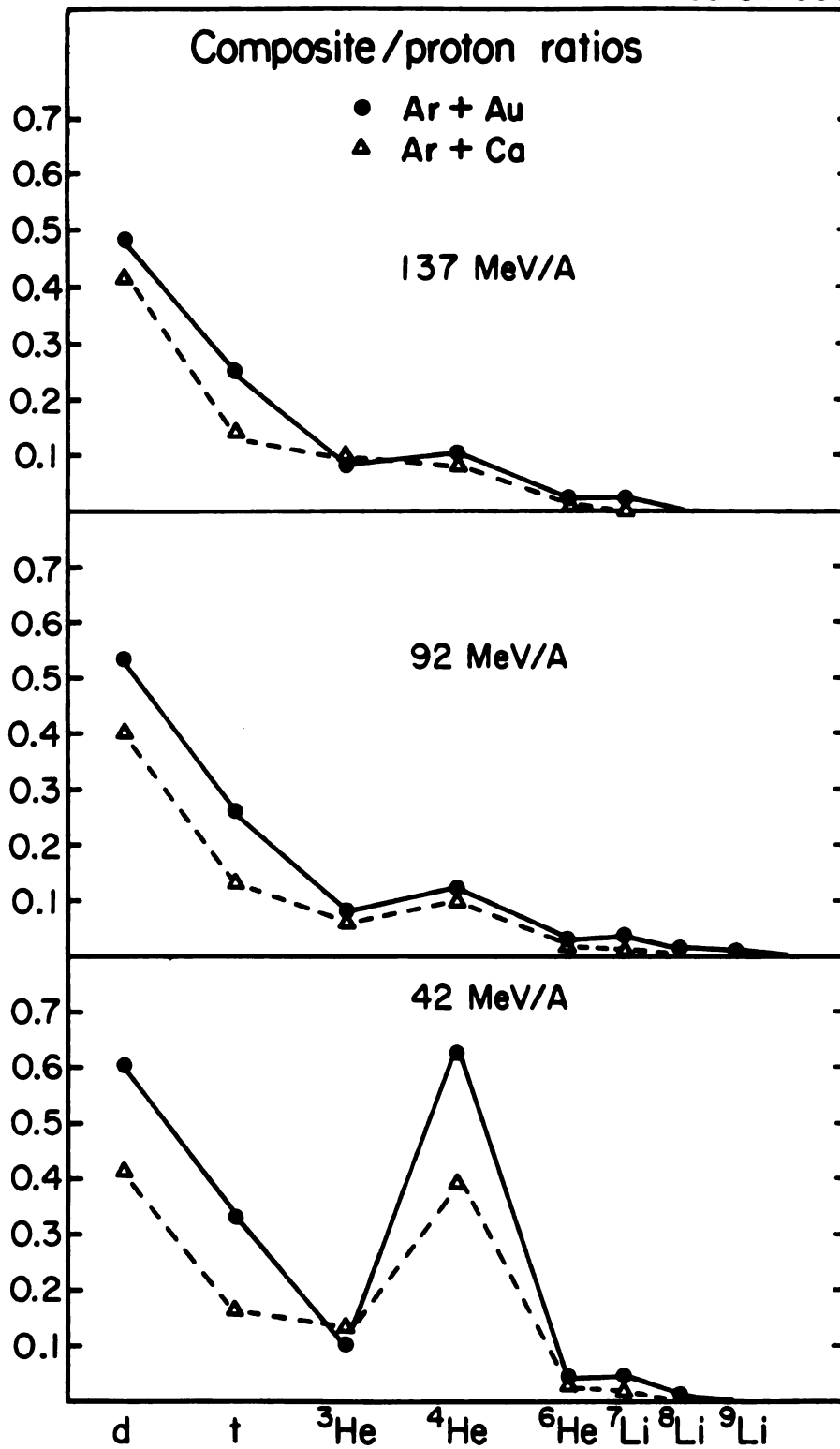


FIGURE IV-6. The ratio of composite fragment cross sections to the proton cross sections for argon induced reactions on Au and Ca targets.

MSU-84-402

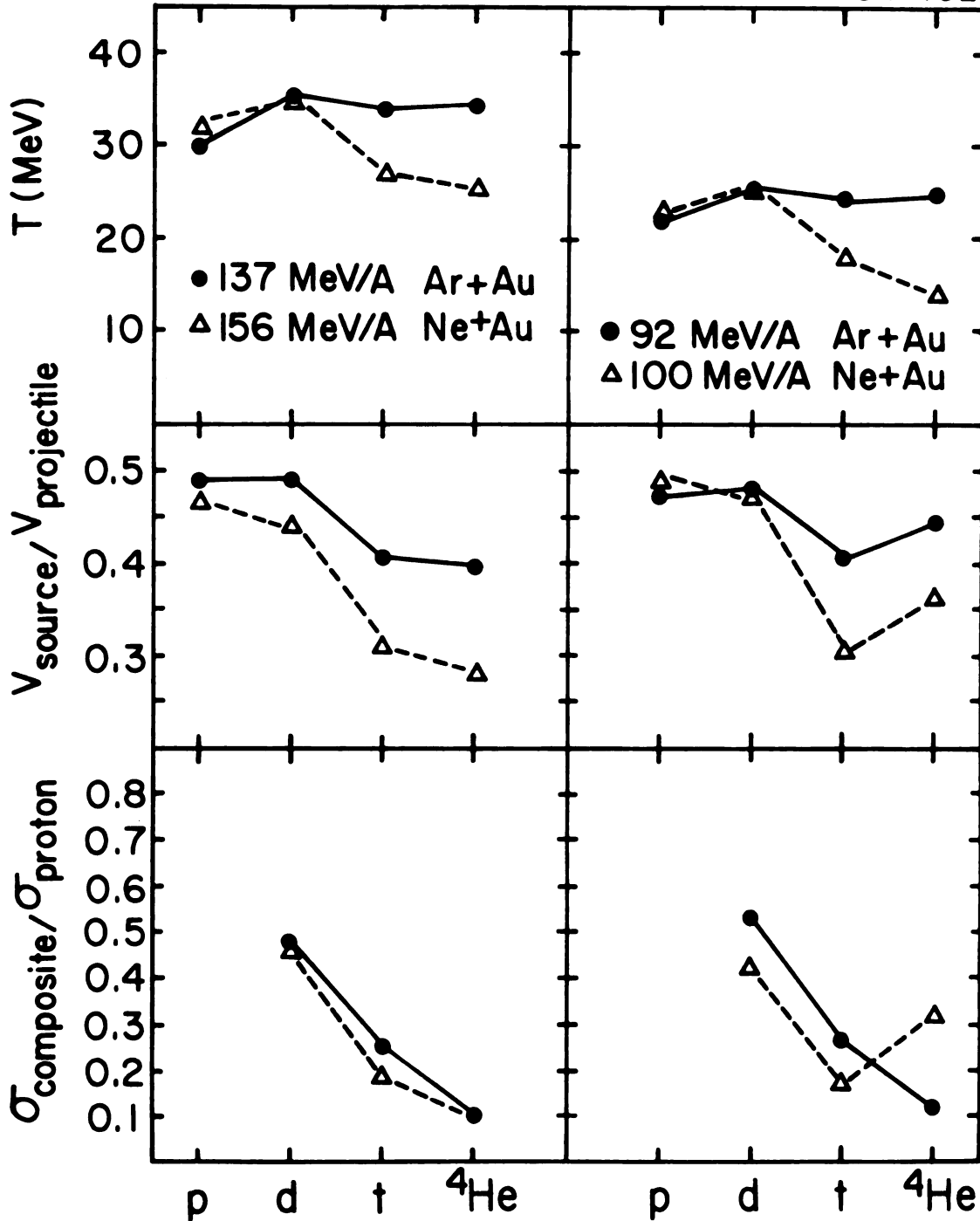


FIGURE IV-7. Projectile dependence of the moving source parameters describing light particle spectra, for Ar and Ne beams on Au targets.

fragment mass in neon-induced reactions. This decrease may reflect a smaller interaction region in neon-induced reactions, leading to a larger target-like source contribution to the triton and ${}^4\text{He}$ spectra. The particles emitted from the target would cause the extracted temperatures and velocities to look lower than if the fitted spectra consisted purely of particles from the intermediate rapidity source.

E. SYSTEMATICS OF THE TEMPERATURE

The excitation energy of the source, given by the temperature parameter and the relative numbers of nucleons and complex nuclei, should vary smoothly with incident energy if a local, thermalized zone is formed [GO 78]. In fact the parameters in the simple one-source description do vary smoothly with bombarding energy [WE 82]. Source temperatures extracted for reactions at 10 to 800 MeV/nucleon are shown in Figure IV-8 (the data are from [AW 81, WE 82, LY 83, NA 81A, SA 80, NA 81]). Although not included in this figure, data from higher energy reactions may also be parameterized in terms of a moving source [MA 82, AD 84].

The solid line in Figure IV-8 is simply a straight line through the data and emphasizes the regularity of the extracted temperature as a function of the available energy per nucleon in the reaction. The dashed line shows the temperature expected for the participants if the projectile

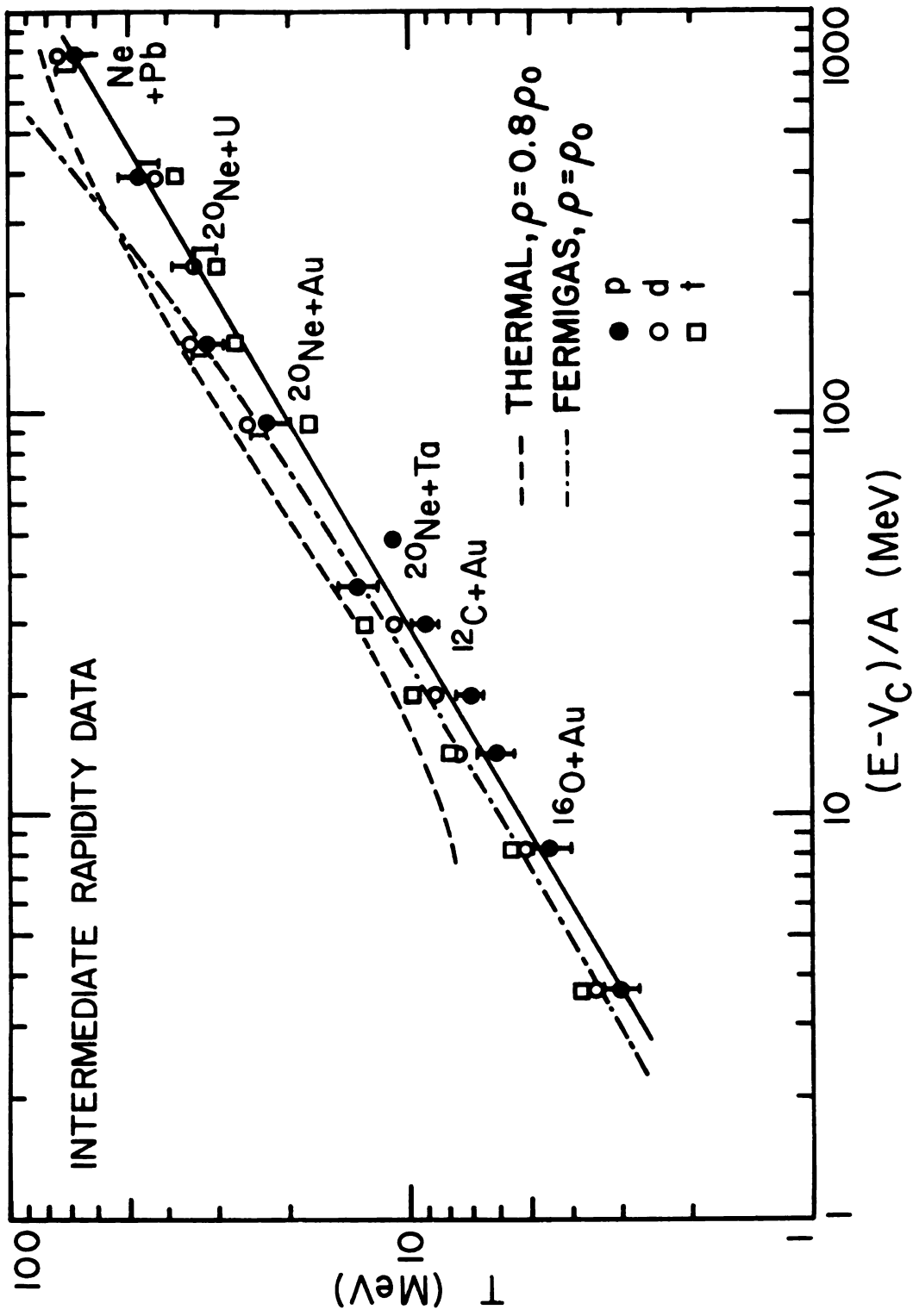


FIGURE IV-8. Bombarding energy dependence of the temperatures extracted from the spectra of p, d, and t. The solid line is to guide the eye through the data, the dashed line is the temperature expected from a Fermi gas model, and the dot-dashed line is the prediction of the fireball model.

and target cut cleanly and the nucleons in the overlapping region come to thermal equilibrium. This temperature is calculated via the fireball model described in the next chapter, and includes pion production when the excitation energy of the system is high enough, causing the flattening of the line above 400 MeV.

The dot-dashed line shows the temperature expected for an ideal Fermi gas of nucleons. The internal energy per nucleon, U/N , is given to the lowest order in τ by [PA 72]

$$\frac{U}{N} = \frac{3}{5} \epsilon_F \left[1 + \frac{5\pi^2}{12} \left(\frac{\tau}{\epsilon_F} \right)^2 \right] \quad (\text{IV-8})$$

During the reaction, the excitation energy per nucleon is related to the incident kinetic energy per nucleon above the Coulomb barrier, $(E-V_c)/A$, by

$$\epsilon^* = \left[m_0^2 - \frac{1}{2} m_0 (E-V_c)/A \right]^{1/2} - m_0 \quad (\text{IV-9})$$

where m_0 is the nucleon rest mass. Writing the excitation energy per nucleon of the gas as

$$\epsilon^* = \langle \epsilon(\tau) \rangle - \langle \epsilon(\tau=0) \rangle = \langle \epsilon(\tau) \rangle - \frac{3}{5} \epsilon_F \quad (\text{IV-10})$$

where $\langle \epsilon(\tau) \rangle$ is the average energy per nucleon at temperature τ , shows the relation between temperature and incident kinetic energy.

The regularity of the temperature parameter as a function of bombarding energy observed over this great range supports the idea that at least some of the nucleons in the projectile and target are involved in a thermalized region during the reaction. The temperatures deduced from the spectra are similar to those expected for such a thermalized system, resembling a Fermi gas at low energies, and including pion production at higher energies. Several models of the reaction mechanism incorporating a thermalization step are discussed in the next chapter.

F. THREE MOVING SOURCES

In order to further investigate the applicability of the participant-spectator picture of reactions at these bombarding energies, we have fitted the light particle data from 137 MeV/nucleon Ar + Au assuming emission from three sources [SC 82]. One source is the intermediate source, analogous to the single moving source described above. The other two sources treat emission of light particles from the relatively cool spectator fragments. We include a projectile-like source, moving with the original projectile velocity and with a temperature of 8 MeV. The target evaporation spectrum is accounted for with a slow source, moving with approximately the compound nuclear velocity.

When fitting the data, it was necessary to hold some of the parameters fixed. The projectile source, for example, was not sufficiently defined by the measured data

as we have no information forward of 30° . Upon successive attempts at fitting the data, we discovered that allowing the projectile-like source parameters to vary resulted in lack of convergence. We therefore held the velocity of this source fixed at the projectile velocity, and the temperature fixed at 8.0 MeV, which is approximately the expected temperature due to the deformation energy in the projectile remnant after the collision [WE 76]. For the protons, the cross section for the projectile-like source was a fitted parameter, but for the other particles we were obliged to hold this parameter fixed as well. For these cases the fitting was done by iteratively changing the cross section, and subsequently choosing the fit with the best chi-square value. The fits were not, however, very sensitive to the cross section of the projectile-like source.

Not all of the parameters for the target-like source could be varied either. We were forced to fix the source velocity. The upper limit of the recoil of the target-like source was estimated with the velocity expected for the compound nucleus. The target-like source temperature and cross section were fitted parameters, and the temperatures were found to be somewhat lower than the 8 MeV expected from a clean-cut geometry.

Within these limitations, we were able to obtain fits for protons through ^3He . We were not able to fit the ^4He spectra, even when holding the spectator source parameters fixed. It is possible that the lack of forward angle and

very low energy data reduced our knowlegde of the alpha emission from the spectator sources so that the three source fit was not significantly better than the single source fit.

Figure IV-9 shows the three source fits for protons, deuterons and ^3He from 137 MeV/nucleon Ar + Au. It is clear that the fits are much closer to the data at forward angles and low energies than the single moving source fit, since particle emission from the spectators is taken into account. The extracted source parameters are given in Table IV-7. The parameters of the intermediate source in the three source fit are very similar to the parameters extracted for the intermediate rapidity source in the single moving source fit. This argument supports the usefulness of the single source parameterization of the intermediate rapidity data, and gives us confidence in the selection criteria applied when making those fits.

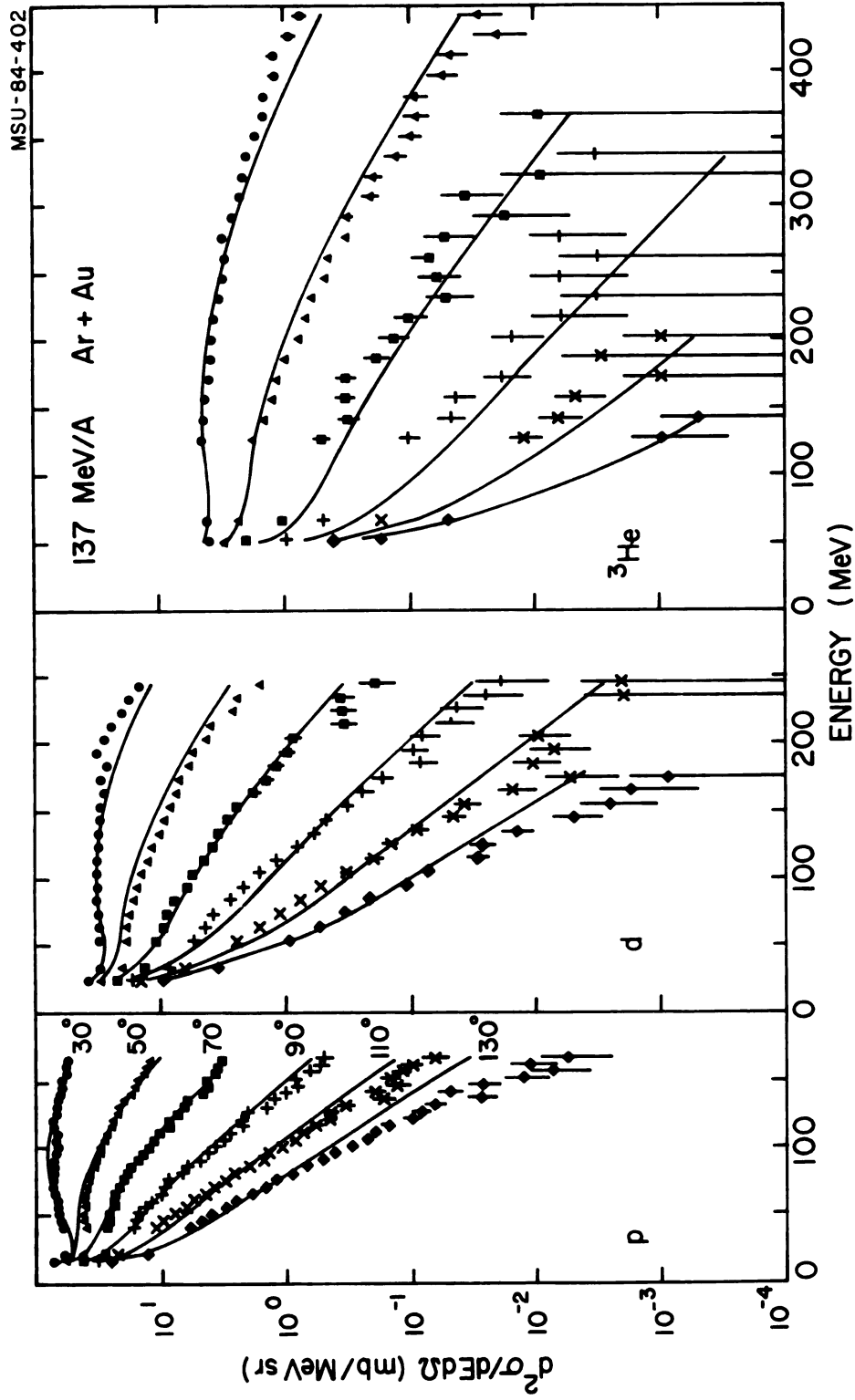


FIGURE IV-9. Fits to the p, d, and ^3He spectra from 137 MeV/A Ar + Au with three moving sources.

Table IV-7. Parameters for fit to 137 MeV/A Ar + Au data with three moving sources.

PART.	PROJECTILE-LIKE			INTERMEDIATE			TARGET-LIKE		
	T (MEV)	S (B)	V/C	T (MEV)	S (B)	V/C	T (MEV)	S (B)	V/C
P	8.00*	43.6	0.51*	28.6	34.5	0.23	4.23	8.1	0.02*
d	8.00*	20.0*	0.51*	32.9	18.4	0.24	8.00*	6.0	0.02*
³ He	8.00*	3.0*	0.51*	37.2	2.8	0.27	6.89	7.0	0.02*

* = PARAMETER HELD FIXED DURING FITTING

CHAPTER V

THERMAL MODELS

A. THE FIREBALL MODEL

As data from relativistic heavy ion collisions became available, a variety of models to explain the reactions were formulated. One class of models treats the reaction as a superposition of nucleonic cascades, an approach which will be discussed in Chapter VI. In hydrodynamical models the nucleons have a very short mean free path, and nuclear matter is treated as a compressible fluid. These models will also be discussed in more detail in Chapter VI. Thermal models assume that an equilibrated system is formed during the reaction [BA 75, AM 75, SO 75, WE 76, DA 81] and ascribe a density and hadronic temperature to the matter during the collision [SO 75, CH 73]. The fireball model [WE 76, GO 77] predicts such quantities by using an idealized geometry for the reaction and statistical formulations of the state of the system.

In the fireball model there is a fast primary reaction stage where the interaction is localized to the overlapping volume of target and projectile nuclei. Later, the compressional and surface energy of the remnants of the two nuclei is dissipated and the remnants decay by particle and γ emission. The excitation energy of the remnants is relatively low, so the particles from the remnants have

lower energies than those from the participants. The nuclear "fireball" consists of the nucleons contained in the region formed via cylindrical cuts swept out of the target by the projectile in the primary part of the reaction, as illustrated in Figure V-1. The projectile nucleons transfer all of their momentum into excitation energy of the fireball, which moves forward in the lab at a velocity intermediate between those of the projectile and target. The fireball is treated as an equilibrated nonrotating ideal gas and the excitation energy and velocity are calculated from the number of nucleons contributed by the projectile and target to the participant region.

The number of nucleons participating in the fireball from a spherical projectile or target nucleus of mass number A_1 and radius R_1 is given by [BO 73, GO 77]

$$N_1 = A_1 F(v, \beta) \quad (V-1)$$

where F is a function (given below) of the dimensionless parameters v , specifying the relative sizes, and β , specifying the impact parameter of the two nuclei.

$$v = \frac{R_1}{R_1 + R_2} \quad (V-2)$$

$$\beta = \frac{b}{R_1 + R_2} \quad (V-2b)$$

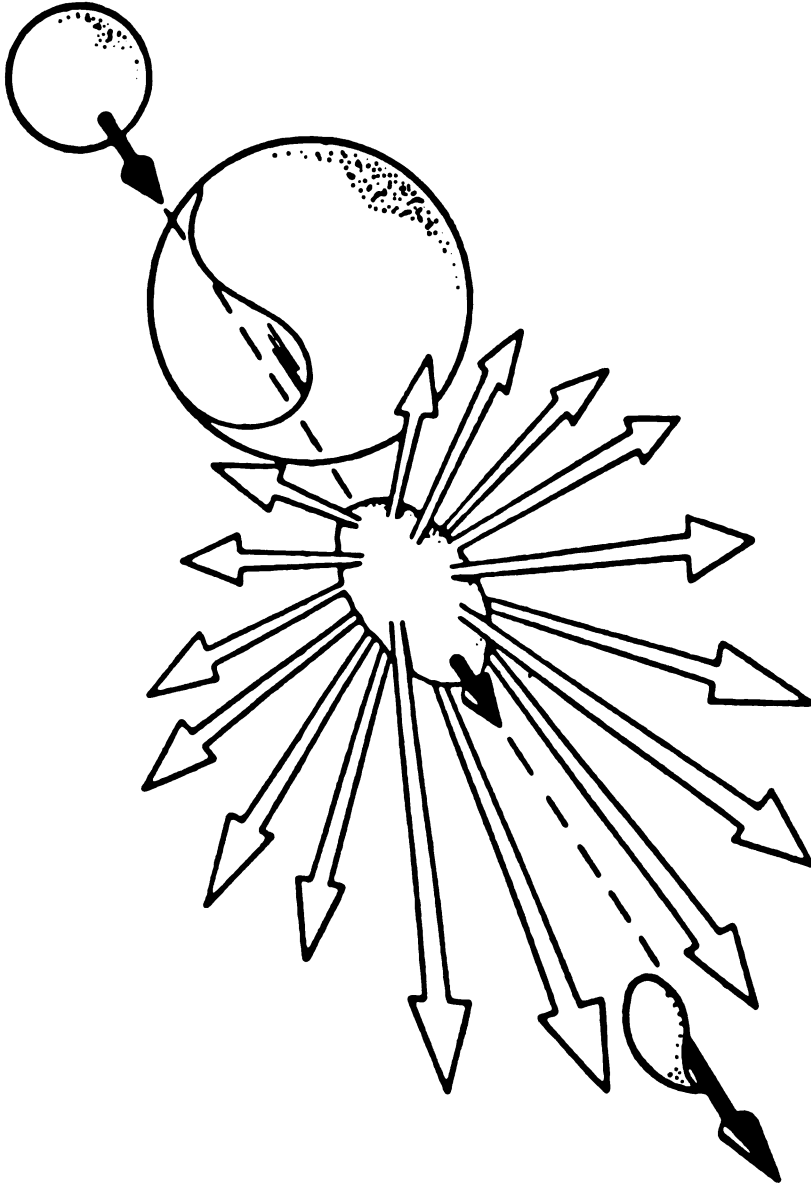


FIGURE V-1. Schematic diagram of the reaction geometry in the fireball model, illustrating the participant -spectator picture with a central "participant" region where the projectile and target overlap, and the cooler "spectator" remnants.

v and β range from zero to one.

The approximate formulas for F are:

$$F_1 = \left[1 - (1-\mu^2)^{3/2} \right] \left[1 - (\beta/v)^2 \right]^{1/2} \quad (V-3a)$$

$$F_2 = \frac{3}{4} (1-v)^{1/2} \left(\frac{1-\beta}{v} \right)^2 - \frac{1}{8} \left(\frac{3(1-v)^{1/2}}{\mu} - \frac{\left[1 - (1-\mu^2)^{3/2} \right] \left[1 - (1-\mu)^2 \right]^{1/2}}{\mu^3} \right) \left(\frac{1-\beta}{v} \right)^3 \quad (V-3b)$$

$$F_3 = \frac{3}{4} (1-v)^{1/2} \left(\frac{1-\beta}{v} \right)^2 - \frac{1}{8} \left[3(1-v)^{1/2} - 1 \right] \left(\frac{1-\beta}{v} \right)^3 \quad (V-3c)$$

$$F_4 = 1 \quad (V-3d)$$

where

$$\mu = \frac{1}{v} - 1 = \frac{R_2}{R_1} \quad (V-4)$$

The four reaction configurations for which F is given are:

- 1) A cylindrical hole is gouged in the nucleus A_1 , and $A_1 > A_2$.
- 2) A cylindrical channel with $R < R_1$ is gouged in A_1 .
- 3) A cylindrical channel with $R > R_1$ is gouged in A_1 .
- 4) All of A_1 is obliterated by A_2 ($R_2 > R_1$).

The velocity of the fireball in the laboratory is given by

$$\beta_{FB} = \frac{P_{LAB}}{E_{LAB}} = \frac{N_p \left[t_i (t_i + 2m') \right]^{1/2}}{(N_p + N_t)m' + N_p t_i} \quad (V-5)$$

with P_{LAB} the momentum of the system in the lab and E_{LAB} the total energy (kinetic plus mass) of the system in the lab. t_i is the projectile incident kinetic energy per nucleon, and m' is the mass of a bound nucleon (931 MeV). The total energy in the center of mass of the fireball is

$$E_{FB} = (E_{LAB}^2 - P_{LAB}^2)^{1/2} = \left[(N_p + N_t)^2 m'^2 + 2N_p N_t m' t_i \right]^{1/2} \quad (V-6)$$

If the available kinetic energy is randomized and we describe the fireball as a relativistic ideal gas of nucleons, the temperature, τ , can be expressed as [LI 80]

$$\frac{E_{FB}}{(N_p + N_t)\tau} = 3 + \frac{m}{\tau} \frac{K_1(m/\tau)}{K_2(m/\tau)} \quad (V-7)$$

where K_1 and K_2 are MacDonalld functions and m is the mass of a free nucleon (939 MeV).

The lab inclusive spectra are calculated by summing over impact parameters (weighted by $2\pi b$) and letting the fireball with temperature, τ , and velocity, β , emit particles with energies given by a relativistic Boltzmann distribution in the fireball rest frame. It is assumed that chemical as well as thermal equilibrium is achieved in the fireball, and composite fragments as well as protons are

emitted. [ME 77, JE 82]. The relative cross sections for protons and composites are determined by the temperature and the numbers of neutrons and protons in the system, the binding energies of the composites, and the density at which the fragments no longer interact. The density used in the present calculation is $\rho = 0.8 \rho_0$, but the results are relatively insensitive to ρ for $0.5 \rho_0 < \rho < 1.5 \rho_0$ [WE 84a].

Figure V-2 shows the results of a fireball calculation for proton, deuteron, and ^3He spectra observed in the 137 MeV/nucleon Ar + Au reaction. The nuclei in the chemical equilibrium are truncated at $A=5$, resulting in unreliable predictions for ^4He production. It is known that at this energy a considerable number of heavier fragments are formed, many of which decay to ^4He . The model is thus expected to underpredict the ^4He cross sections and this is in fact the case. The points show the data with statistical error bars. The solid lines show the results of the calculation at 30, 50, 70, 90, 110, and 130 degrees in the laboratory. The agreement between the theory and the data is rather poor, especially at forward angles, where the fireball seriously underpredicts the high energy tails of the spectra. The temperature of the fireball is reflected by the slopes of the calculated spectra. This may be best compared with the data at 90° , where the transformation to the laboratory has the smallest effect. For all three particles the 90° theory and data show a very similar slope, even though the absolute cross section from the calculation

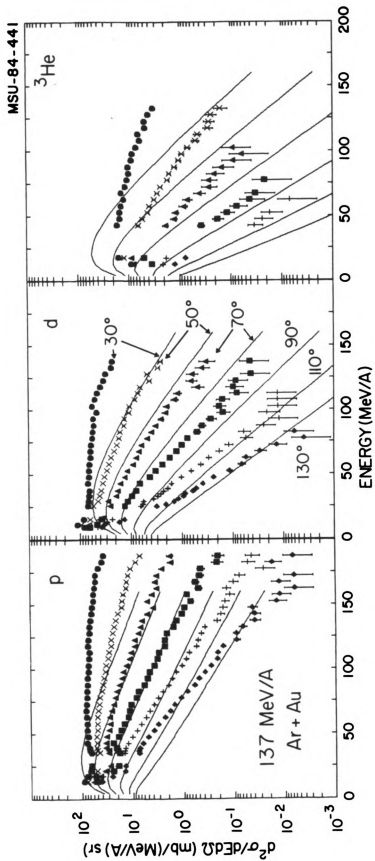


FIGURE V-2. Predictions of the fireball model (solid lines) and data for p, d, and ³He from 137 MeV/nucleon Ar + Au.

is incorrect. In fact, at the most probable impact parameter for Ar + Au, $b=5.2$ fm, the temperature of the fireball is 31 MeV, compared with 30 MeV extracted from the proton spectra with the single moving source fit.

The angular distribution of the calculation, which may be inferred from the spacing of the lines, reflects the velocity of the fireball. A slowly moving fireball would cause relatively small changes in each angle upon transformation to the laboratory frame, yielding closely spaced lines in Figure V-2. It is clear that the calculated angular distribution is too isotropic since the spacing between the angles is considerably smaller for the fireball calculation than for the data. If we once again consider the fireball at the most probable impact parameter, we find that the fireball moves with a velocity of $0.20c$, whereas the fitted moving source velocity was $0.24c$.

The fireball predictions reproduce the data much better for relativistic collisions [GO 77] than the results shown in Fig. V-2. It is quite clear that the simple geometrical assumptions of the fireball model should break down for the intermediate energies. Several estimates have been made for the times required for various phases of the reaction. Bertsch and Cugnon estimated that the entropy per participant nucleon decreases to a constant value (the entropy increases, but the number of struck nucleons increases faster) in about 3×10^{-23} seconds [BE 81]. At this point the participant zone has reached its maximum size

and begins to expand. The cooling of the hot zone has been calculated to be in the 10^{-23} second range as well [BO 84b]. In addition, the freezeout time has been estimated at 4×10^{-23} seconds by following the time development of fragment distributions and comparing to observed distributions [BO 83b]. In order to evaluate the fireball geometrical picture, these source lifetimes of $4 - 5 \times 10^{-23}$ seconds should be compared with the transit time of a 137 MeV/nucleon Ar nucleus through a Au target. Taking the distance to be traveled by the projectile as

$$d = 2 \times 1.2 (A_1^{1/3} + A_2^{1/3}) \quad (V-8)$$

and a projectile velocity of $0.49c$, we arrive at a time of 15×10^{-23} seconds. It is clear that the projectile is not well separated from the target by the time the source emits particles, and that the interaction of the hot, compressed matter with the surrounding spectator nucleons should be taken into account for intermediate energy collisions.

B. DEUTERON-TO-PROTON RATIOS AND ENTROPY

Even though the dynamics of the reaction are not as simple as assumed in the fireball model, a consistent picture emerges from thermal, TDHF, hydrodynamical [ST 80, ST 81b], and intranuclear cascade calculations [CU 81, CU 81a, BE 81]. As the nuclei interpenetrate each other,

nuclear matter is compressed and highly excited. From the state of highest density ($\rho > 2-4 \rho_0$) and temperature the system expands at approximately constant entropy towards lower densities, $\rho \leq \rho_0/2$. During the expansion the temperature drops, and in the late stages of the reaction the system disintegrates and the finally observed fragments are formed [ME 77, SU 81]. Our goal in performing these studies was to learn about the conditions present during the hot dense stage of the reaction. It is clear, however, that the temperature values derived from the observed slopes do not directly reflect the actual initial temperature, so we must study other properties of the system. A state variable which is expected to stay constant during the expansion is the entropy per nucleon, S/A [ST 84]. Hence we need to determine a measure for the entropy to gain information on the properties of the system early in the reaction.

It has been suggested that if chemical equilibrium is indeed reached, the entropy can be deduced from the observed deuteron-to-proton ratio, R_{dp} , [SI 79a]. This situation comes about if the system can be described in terms of an ideal gas; then the entropy per nucleon is given by the Sackur-Tetrode equation

$$S/A = 5/2 - \mu_p/\tau \quad (V-9)$$

where μ_p is the proton chemical potential. The chemical potential for a composite particle of A nucleons, μ_A , is given by [PA 72]

$$\mu_A = \tau \ln \left[\frac{n_A}{n_A^c} \right] - \epsilon_A \quad (V-10)$$

where n_A and ϵ_A are the density and binding energy of species A and n_A^c is the critical density or inverse cube of the thermal wavelength

$$n_A^c = g_A \left(\frac{m_A \tau}{2\pi \hbar^2} \right)^{3/2} \quad (V-11)$$

Here g_A and m_A are the spin degeneracy and mass of particle A. If the number of protons greatly exceeds the number of deuterons and if other clusters can be neglected, the entropy per nucleon is [Si 79a, MI 80]

$$\frac{S}{A} = \frac{5}{2} + \left\{ \frac{\epsilon_d}{\tau} + \ln \left[\frac{g_d}{g_p} \left(\frac{m_d}{m_p} \right)^{3/2} \right] - \ln R_{dp} \right\} \quad (V-12)$$

Neglecting the deuteron binding energy,

$$S/A = 3.95 - \ln R_{dp} \quad (V-13)$$

Since experimentally $R_{tp} \ll R_{dp} \lesssim 0.4$ at $E \gtrsim 400$ MeV/nucleon [NA 81, NA 82], this simple formula was expected to be

applicable. However, the entropy extracted from the data in this way is much larger than expected.

Figure V-3 shows the entropy obtained from a hydrodynamical calculation [ST 84] compared with the entropy extracted from the data via equation (V-13). The experimental R_{dp} is almost constant with bombarding energy, leading to a flat energy dependence of the entropy. This behavior is inconsistent with the expected drop with decreasing bombarding energy of the entropy generated in the collision. Even for $E_{LAB} \geq 400$ MeV/nucleon, the values of "S" extracted from the data exceed the calculated entropies. On the other hand, the deuteron-to-proton ratios obtained from the hydrodynamical model combined with a chemical equilibrium calculation [ST 84] agree well with the experimental data over the whole range of bombarding energies considered. This apparent paradox can be explained by the decay of particle-unstable excited nuclei $A^* \rightarrow (A-1)+p$, which becomes increasingly important at intermediate and low bombarding energies. Hence the relation between the entropy and the observed R_{dp} is not given by the simple formula of eqn. (V-13).

To learn about the entropy, we must include these additional states into any equations connecting the entropy with experimentally observable quantities, requiring much more complicated theoretical treatment. Including the decay of particle-unstable nuclei influences the experimental approach to measuring the entropy as well. Many protons are

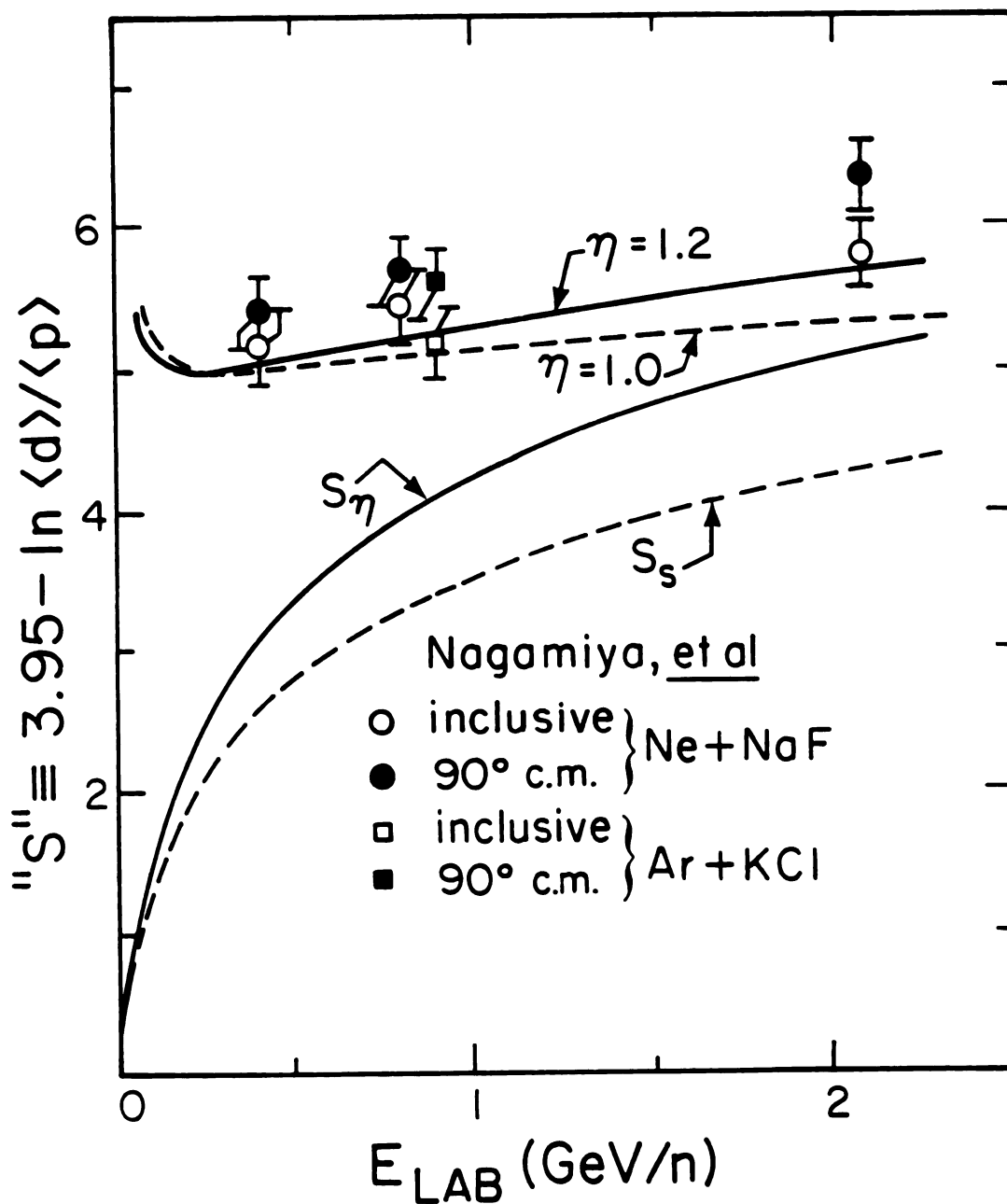


FIGURE V-3. Bombarding energy dependence of the entropy as calculated for viscous (S_{η}) and non-viscous (S_s) fluids. Also shown are the "S" values obtained from measured and calculated deuteron- to-proton ratios.

created by the decay of complex fragments with $A > 4$, a mass region not covered by many experiments. As the beam energy is lowered into the intermediate energy regime, the cross sections for heavier fragments relative to the light particle cross sections increase considerably. Thus, it becomes especially important to take heavier fragments into account when studying the entropy from intermediate energy collisions.

C. QUANTUM STATISTICAL MODEL

1. DESCRIPTION

Many statistical models have been formulated to describe the production of fragments heavier than deuterons. These models range from the sequential decay of the Hauser-Feshbach approach [FR 83] to explosion-evaporation models incorporating classical [RA 81, FA 82] or quantum statistics. We have used a quantum statistical model of nucleons and nuclei in thermal and chemical equilibrium at a given temperature and density. We have extended current quantum statistical models [GO 78, SU 81] to take into account ground state and γ -unstable nuclei up to $A=20$, and the known particle-unstable nuclear states up to $A=10$ [ST 83]. The truncation of available states makes the predictions of this model less reliable above $A=10$, however comparisons with data are not done above $A=14$. The model treats fermions and bosons with the correct statistics, and

incorporates excluded volume effects, pions and the delta resonance. The model does not include dynamical aspects of the reaction; it presupposes the existence of a thermalized subsystem and requires a choice of how much expansion takes place before the fragments cease to interact. This freezeout density is typically taken as 0.3-0.5 times normal nuclear matter density ($\rho_0 = 0.17$ nucleons/fm³). Recently, it has been estimated at $0.25 \rho_0$ by a measurement of correlations between protons emitted from the thermalized system [GU 84].

Baryon number and charge conservation are achieved via

$$\bar{Z} = \sum_{i=1}^N n_i(Z_i, N_i) \cdot Z_i \quad (V-14)$$

$$\bar{N} = \sum_{i=1}^N n_i(Z_i, N_i) \cdot N_i \quad (V-15)$$

where n_i is the number of particles of species i with Z_i protons and N_i neutrons. The equilibrium is established in a volume V_{ext} (or a density ρ) and temperature τ . Each particle moves freely in the volume V left over from the external volume V_{ext} after subtracting the volume occupied by each particle

$$V = V_{\text{ext}} - \sum_i n_i V_i \quad \rho = (\bar{Z} + \bar{N})/V_{\text{ext}} \quad (V-16)$$

where V_i is the i^{th} particle's volume. So the point-like particles move freely in a reduced volume V with the density determining the chemical equilibrium of $p_{pt} = (\bar{Z} + \bar{N})/V$. For fermions we have

$$\frac{\lambda_i^3 n_i}{g_i V} = \left(\frac{2}{\pi^{1/2}} \right) F_{FD}(v_i) \quad i = p, n, {}^3\text{He}, t, {}^5\text{Li}^*, \dots \quad (\text{V-17})$$

where

$$\lambda_i = \frac{h}{(2\pi m_i kT)^{1/2}} \quad (\text{V-18})$$

is the thermal wavelength of the i^{th} particle with mass m_i . The spin degeneracy factor $g_i = 2S_i + 1$. The chemical potential of the i^{th} particle is μ_i ,

$$v_i = \beta\mu_i = \mu_i/kT \quad (\text{V-19})$$

and

$$F_{FD}(v_i) = \int_0^\infty dx x^{1/2} / (\exp(x-v_i) + 1) \quad (\text{V-20})$$

We use the function $F_{FD}(v)$ as tabulated in the literature [SU 81]. For bosons

$$n_i = 1/(\exp(\alpha_i) - 1) + (g_i V / \lambda_i^3) F_{BE}(\alpha_i) \quad i = d, {}^4\text{He}, d^*, \dots \quad (\text{V-21})$$

where $\alpha_i = -\beta\mu_i$. The first term gives the number of condensed particles, and [SU 81]

$$F_{BE}(\alpha) = \sum_{n=1}^{\infty} \exp(-n\alpha)/n^{3/2} \quad (V-22)$$

The constraint of chemical equilibrium implies that the chemical potential

$$\mu_i = Z_i \mu_p + N_i \mu_n + E_i \quad (V-23)$$

where

$$E_i = Z_i m_p c^2 + N_i m_n c^2 - m_i c^2 \quad (V-24)$$

is the binding energy of the cluster (Z, N).

2. CALCULATED DEUTERON-TO-PROTON RATIOS

Figure V-4 shows the deuteron-to-proton ratio obtained from the quantum statistical calculation. The curves are labeled by the point particle densities, $\rho_{pt}/\rho_0 = 0.5$ and 0.1 , corresponding to breakup densities $\rho_{bu}/\rho_0 = 0.32$ and 0.09 , respectively. The excluded volume effects become important only at high densities, $\rho_0 > 0.25 \rho_0$. The value of R_{dp} in chemical equilibrium is given by the curve labeled $R_{dp}^{\text{primordial}}$. In contrast to expectations from the data,

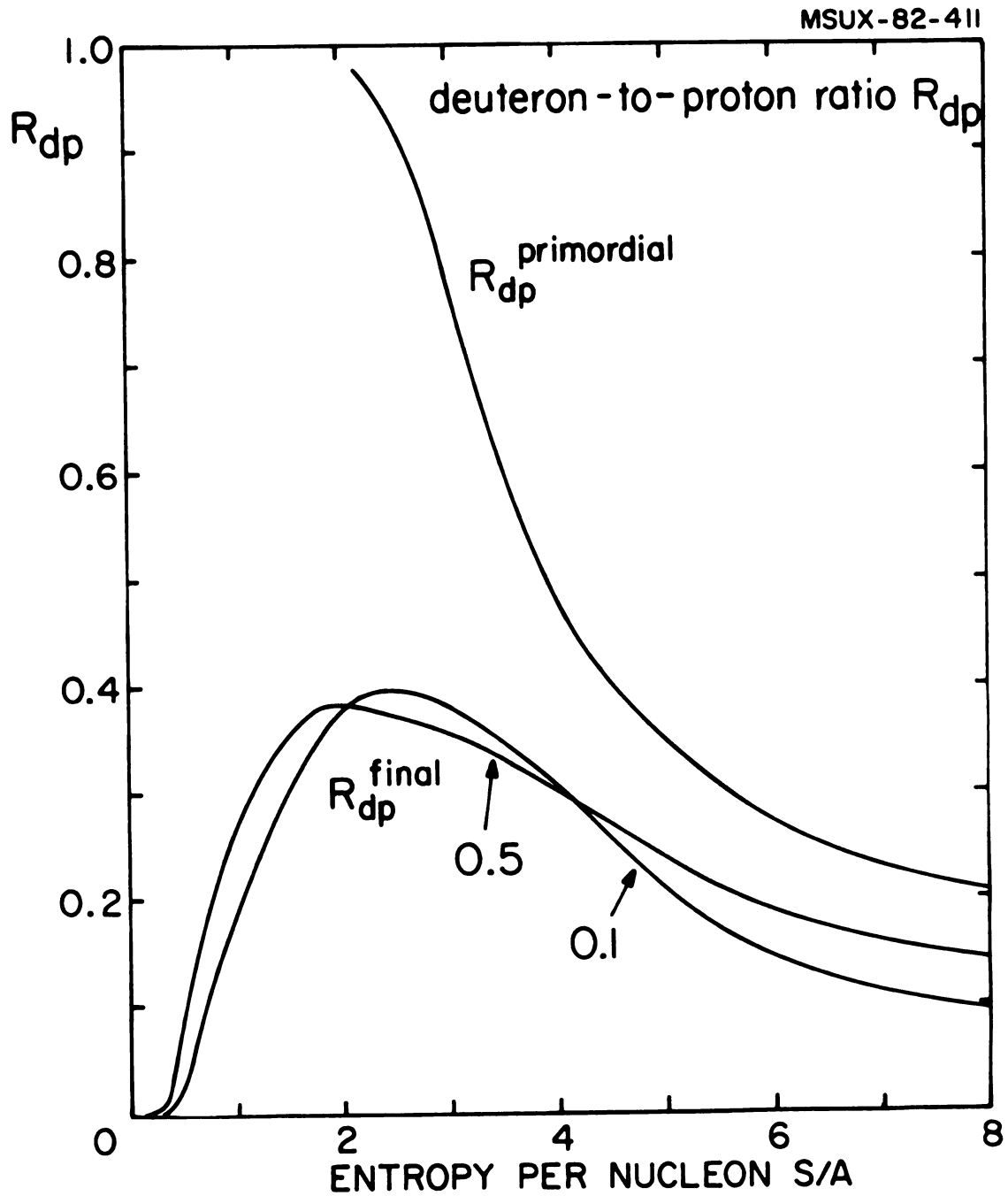


FIGURE V-4. Deuteron-to-proton ratios calculated from the quantum statistical model at two breakup densities, $\rho=0.1 \rho_0$, and $0.5 \rho_0$. The primordial and final (after decay of excited states) ratios are shown.

R_{dp} is not much smaller than unity, but in fact approaches unity at $S/A = 2$. However, due to the decay of the particle-unstable nuclides, R_{dp} drops substantially. It is noteworthy that R_{dp}^{final} is nearly independent of the exact value of the breakup density [ST 84], and $S(R_{dp})$ varies by about 10% despite variations in the point-particle densities of a factor of 5.

Also evident from Figure V-4 is the fact that R_{dp} is a multi-valued function of the entropy. The rise of "S" (eqn. V-8), or depletion of R_{dp} predicted [ST 84] to occur at intermediate energies ($E \lesssim 100$ MeV/nucleon) has indeed been observed [WE 82] and lends support to this calculation. The triton and ${}^3\text{He}$ to proton ratios are also multivalued functions of S/A , and may carry information about the entropy for high ($E > 400$ MeV/n) or low ($E < 100$ MeV/n), but not for intermediate energy collisions.

The independence of the ratios on the breakup density eliminates the only unknown parameter, ρ_{bu} , from the calculation. The extracted entropy per nucleon, however, depends on whether the matter from which the fragments are formed has actually participated in the violent interaction or whether it has been a projectile or target spectator. Therefore, we expect a distribution of entropy values in coordinate as well as in momentum space even in a single collision (i.e. the mean entropies of the participant matter, the projectile-like fragments and the target-like fragments). Since R_{dp} , R_{tp} and $R_{{}^3\text{He}p}$ reach plateaus in the

intermediate energy regime, we need a different messenger to provide information on the entropy.

It has been suggested [BE 81, KA 84] that the entropy may be studied via $R_{"d"Z}$, the ratio of "deuteron-like" to "proton-like" particles, i.e. the ratio of observed correlated nucleon pairs in light clusters ($1 \times d + 3/2(t + {}^3\text{He}) + 3 \times {}^4\text{He}$) to the total number of observed protons (including bound protons). This approach takes into account formation of clusters heavier than deuterons, but neglects particle-unstable clusters. Figure V-5 shows the primordial $R_{"d"Z}$, which includes only the ground states of the nuclides $2 \leq A \leq 4$, and the finally observable $R_{"d"Z}$, which also includes the decay products as a function of the entropy. The behavior is qualitatively the same as for $R_{dp} : R_{"d"Z}^{\text{final}}$ is strongly affected by the decay of excited clusters and shows a maximum at $S/A \approx 2$. In fact, when the entropy was extracted using this method, the resulting value was never below $S/A = 3.5$, even for low incident energies [KA 84].

D. ENTROPY EXTRACTED FROM FRAGMENT DISTRIBUTIONS

We can use the quantum statistical model to learn about the entropy using measured mass distributions including heavy fragments. The temperatures extracted from the observed spectra and shown in Figure V-6 give us some confidence that the heavy and light fragments originate from the same type of source, and the relative cross sections

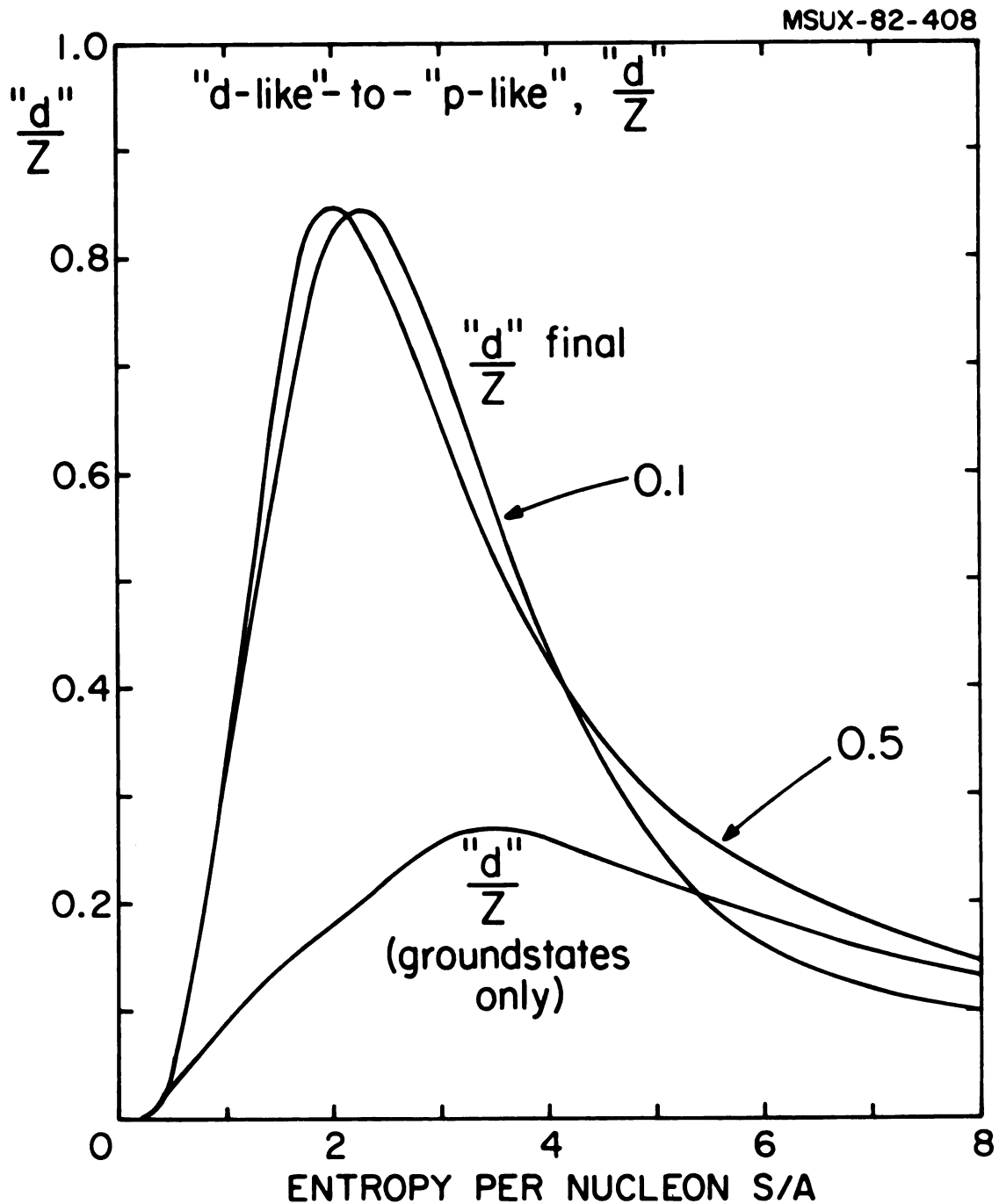


FIGURE V-5. Ratio of deuteron-like to proton-like particles from the quantum statistical model at two breakup densities, as in Figure V-4. The primordial $R_{nd}Z$ only includes the ground states of nuclei with $2 \leq A \leq 4$.

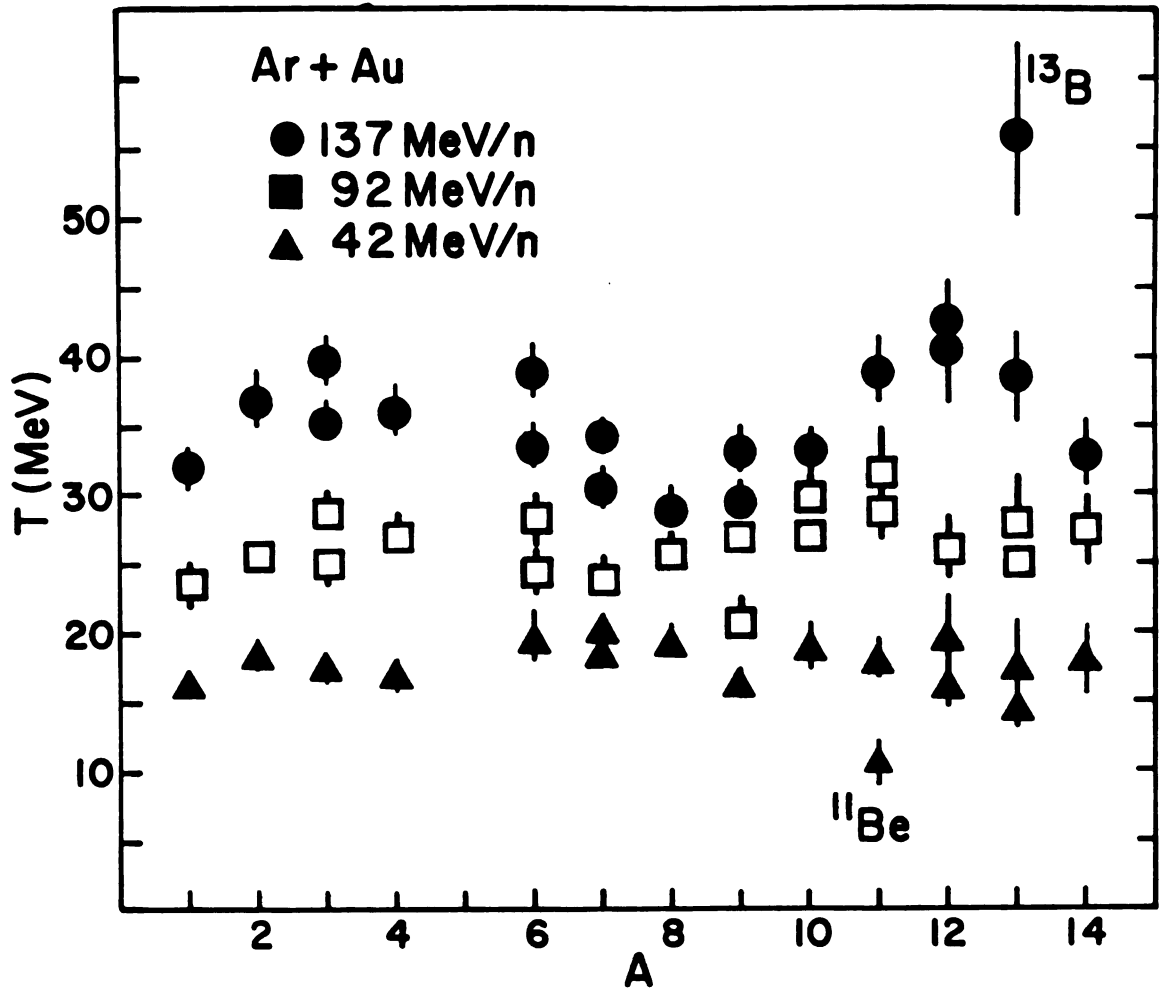


FIGURE V-6. Temperatures from single moving source fits to fragment spectra from Ar + Au, as a function of the fragment mass.

should carry information about the entropy of that source. The entropy is extracted by performing the calculation at a given S/A and density, ρ , thus fixing the temperature. The density used corresponds to the breakup density, where the emitted particles no longer interact. A density of $0.5\rho_0$ was used for these calculations, but the fragment distributions are not very sensitive to the assumed breakup density for $0.3\rho_0 < \rho < 0.8\rho_0$ [ST 83]. The N and Z of the initial system are chosen to be those of the fireball at the most probable impact parameter. The entropy is then determined by a least-squares fit of the calculated yields to the observed fragment distributions. It should be noted that in the calculation, excited states are populated and then decay only via their normal decay channels; this corresponds to decay of excited fragments only after freeze-out has occurred. Recent experiments [MO 84] have suggested that final state interactions may be present, causing the observed distribution to be somewhat different from the distribution resulting from the ground + decayed excited states [BO 84a].

1. INTERMEDIATE RAPIDITY FRAGMENTS

The top part of Figure V-7 shows the measured mass distributions for the Ar + Au reactions. The solid histograms show the results of the best fit with the quantum statistical model. The lower part of the figure shows the

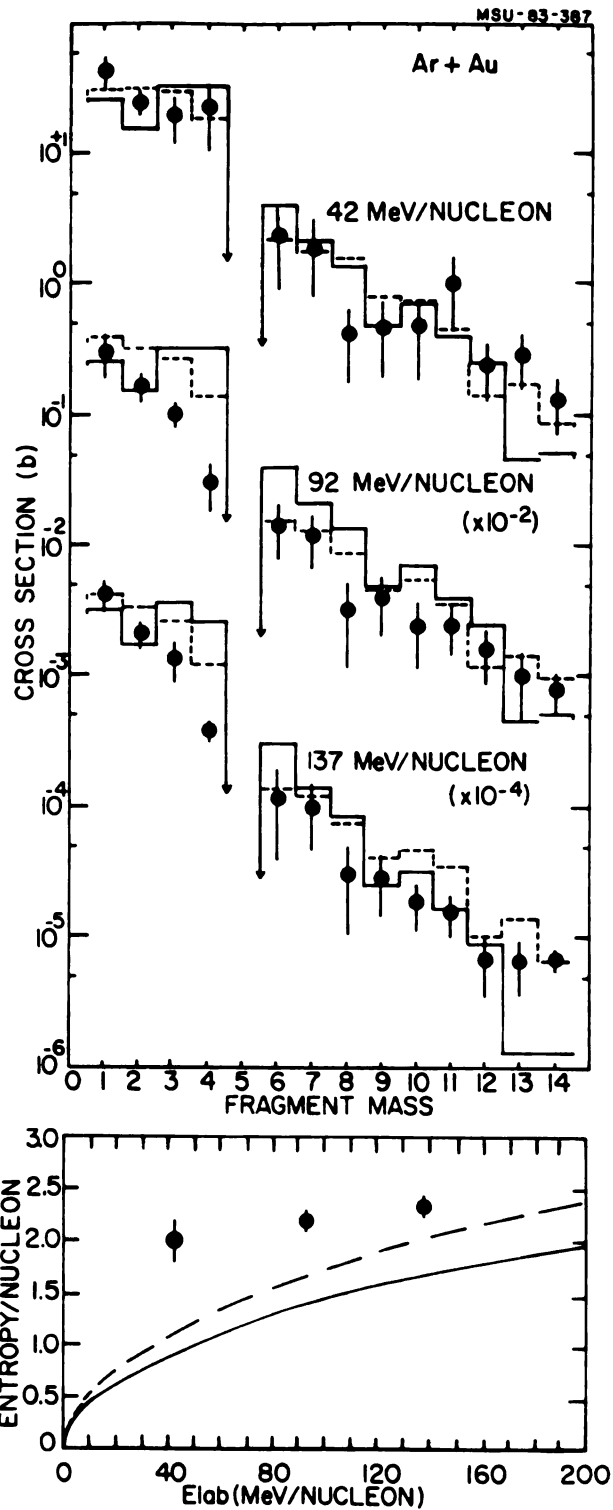


FIGURE V-7. a) Fragment production cross sections. The solid and dashed histograms are results of quantum statistical and Hauser-Feshbach calculations, respectively. b) Entropy extracted from the fits, as a function of bombarding energy. The solid and dashed lines are the entropies expected from non-viscous and viscous fluids [ST 84]

entropy values obtained from the fits: $S/A = 2.0 \pm 0.2$, 2.2 ± 0.2 and 2.35 ± 0.2 for $E_{\text{LAB}} = 42, 92$ and 137 MeV/nucleon, respectively. The solid line shows the average entropy per nucleon expected for the participants using a conventional hydrodynamic calculation, and the dashed line the result for a viscous fluid [ST 84]. Entropies in the range of 4-6 were previously extracted from the observed deuteron-to-proton ratios; the present entropy values are lower than these, but still higher than those expected from hydrodynamical calculations [ST 83]. It should be noted that the theoretical results correspond to an upper limit for the entropy produced because in the calculation the incident matter stops. At low energies the mean free path of the nucleons may be quite long, causing the nuclei be rather transparent to one another and little or no entropy to be produced in the collision.

To determine the extent to which the extracted entropy depends on the assumed breakup mechanism, we have performed a calculation based on the Hauser-Feshbach formalism [FR 83]. These results are shown in the top of Figure V-7 as the dashed histograms. In this approach, particles are statistically emitted from an excited nucleus at constant density, and the temperature, charge, and mass evolution of the system are followed. Emission of nuclei in ground and particle-stable excited states as well as unstable states with lifetimes long compared to the emission time is included. A spherical initial system with $Z=34$ and $A=82$ was

assumed, again corresponding to the fireball at the most probable impact parameter. The entropy extracted is for the initial system with a level density corresponding to an ideal Fermi gas. Entropies determined by fitting the measured mass yields with respect to T at fixed ϵ_F were found to be rather independent of ϵ_F in the range of $24 < \epsilon_F < 60$ MeV. The histograms represent calculations for $\epsilon_F = 38$ MeV, corresponding to an ideal Fermi gas at normal nuclear matter density.

The entropy values deduced from the two very different approaches to the dynamics of the reaction, the explosion picture of the quantum statistical model, and the sequential emission of the Hauser-Feshbach model, are consistent to within S/A of 0.2. This agreement confirms the independence of the entropy determination from assumptions about the breakup dynamics.

2. RAPIDITY DEPENDENCE OF THE ENTROPY

This work is one of the few studies of fragments heavier than alpha particles emitted from the participant region of the reaction. However, a large body of data exists on the emission of target rapidity fragments from proton and heavy ion-induced reactions on heavy targets. We can apply the method described above to study the bombarding energy dependence of the entropy produced in the target remnant, and to investigate the differences in the entropy

produced in the participant and spectator regions of the reaction.

In Figure V-8 relative production cross sections are shown for target rapidity fragments from the reactions of 400 MeV/nucleon Ne + U [GO 77], 2.1 GeV/nucleon Ne + Au [WA 83], 480 MeV p + Ag [GR 80], and 80-350 GeV p + Xe [FI 82]. The solid lines in the figure represent the quantum statistical calculation described above carried out at a density of $\rho = 0.3 \rho_0$. Although data were measured up to $A=30$ for the p + Xe case, only the cross sections that can be compared with the present model are shown. The fits agree well with the observed fragment yields for all four cases, except for $Z=2$ fragments from 480 MeV p + Ag.

The entropies obtained from the fits to these fragment distributions as well as those extracted from the reactions of 30 MeV/nucleon C + Au [CH 83], 55-110 MeV/nucleon C + Ag [JA 82], 250 MeV/nucleon Ne + Au [WA 83], 2.1 GeV/nucleon Ne + U [GO 77], and 4.9 GeV p + Ag and U [WE 78] are shown in the top of Figure V-9 as a function of the incident energy. The depicted errors reflect the errors from the fits as well as known systematic errors in the data. The fits generally encompass fragments with $3 \leq Z \leq 10$ and appear to be independent of both projectile type and energy. The average value for S/A in these cases is 1.84 ± 0.16 . Not shown in this figure is S/A extracted from 80-350 GeV p + Xe [FI 82], which is 1.46 ± 0.67 . This constant value of about 1.8 for the extracted S/A coincides with the expected entropy of

MSU-83-593

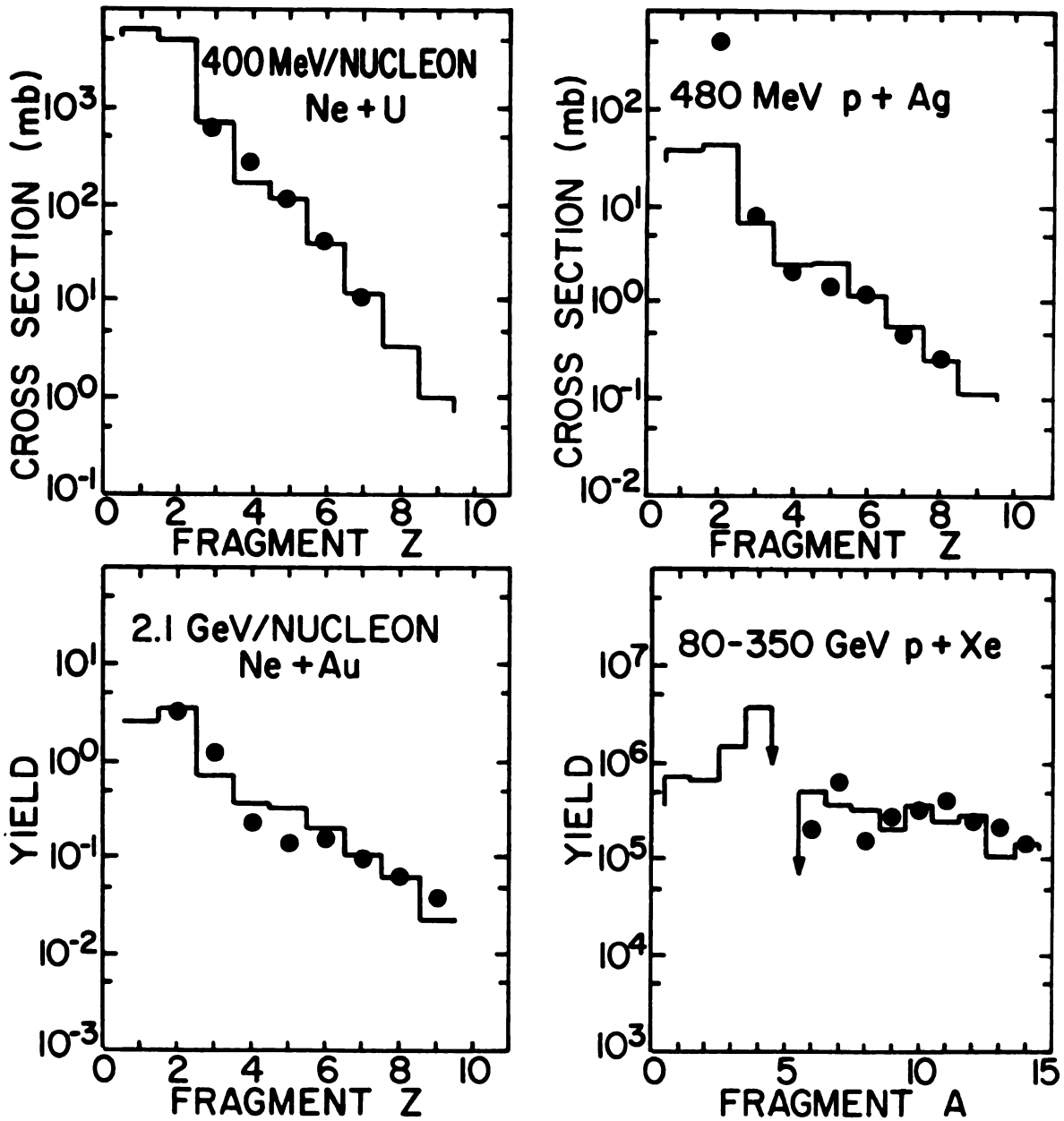


FIGURE V-8. Mass distributions of target rapidity fragments. The histograms are fits with the quantum statistical model.

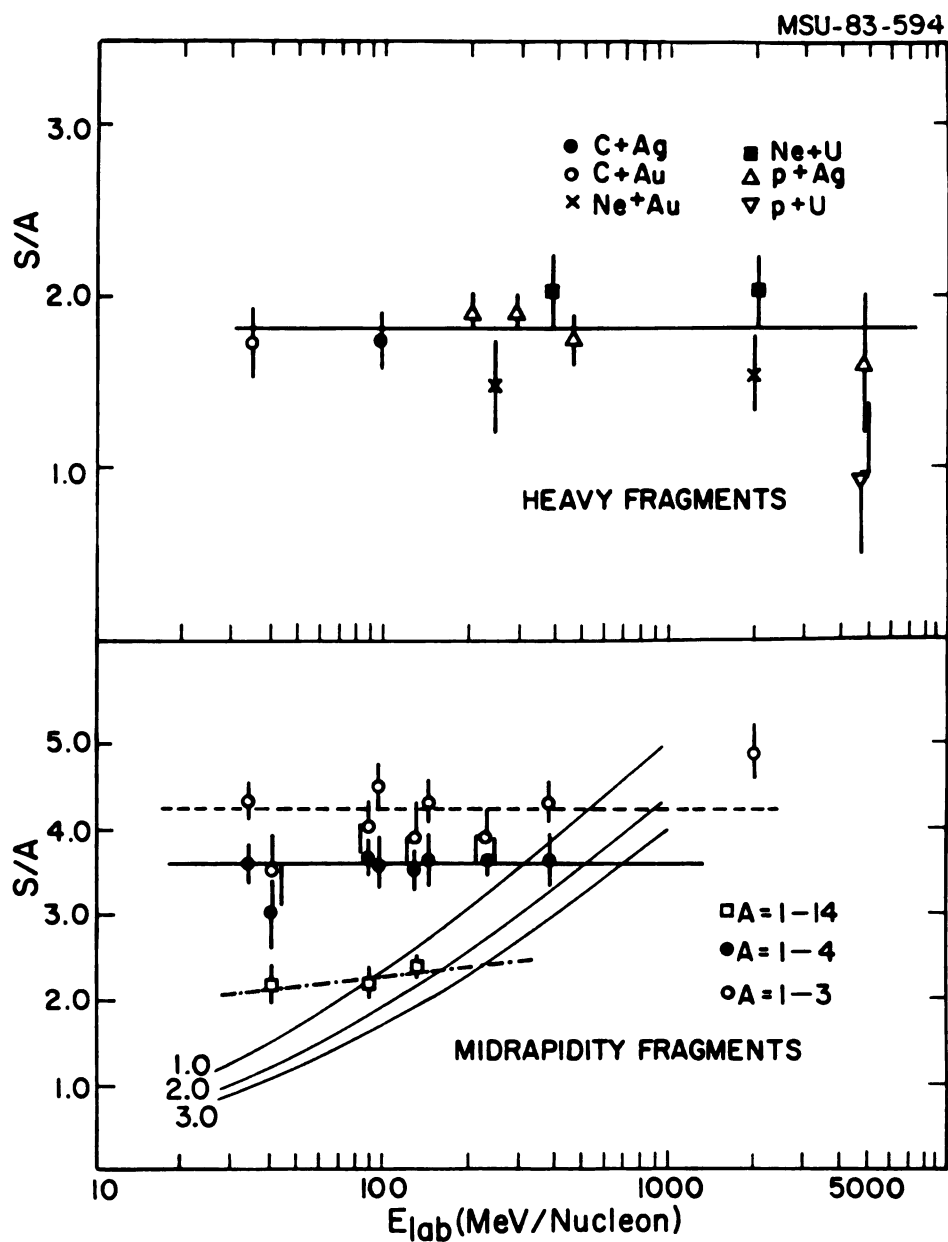


FIGURE V-9. Extracted entropy per nucleon: a) from target rapidity fragments and b) from midrapidity fragments. The solid and dashed lines represent the weighted average for fragments with $1 < A < 3$ and $1 < A < 4$, respectively. The three grouped solid lines show the entropy calculated using a fireball geometry and a Fermi gas model at three different values of ρ/ρ_0 .

nucleons in the target nucleus if it is excited to its binding energy, and suggests that there is a limit to the amount of energy the target remnant is able to absorb from the projectile and/or participant region before it breaks up.

Shown in the bottom of Figure V-9 are the extracted entropies for the intermediate rapidity fragments from the Ar + Au reaction. These values are higher than those extracted from target fragments and increase somewhat with bombarding energy. No complex fragment data currently exist at energies above 137 MeV/nucleon as the data of Gosset, et. al. [GO 77] and Warwick, et. al. [WA 83] do not extend to intermediate rapidities for the heavier fragments. We are therefore unable to follow the energy dependence of the entropy over a large range of bombarding energies. The figure contains S/A values expected from a fireball model taking into account the slowing from Coulomb repulsion between the two nuclei and calculating the entropy using the Fermi gas model. These calculations are shown as solid lines for three densities, $\rho = 1.0 \rho_0$, $2.0 \rho_0$, and $3.0 \rho_0$. The maximum density of the fireball should increase with beam energy, so these curves are clearly a rough estimate of the expected behavior of the entropy.

The extracted entropies from intermediate rapidity fragments with $1 \leq A \leq 3$ and $1 \leq A \leq 4$ from nucleus-nucleus reactions are also shown in the bottom of Figure V-9. Typical fits to intermediate rapidity light particles only

are shown in Figure V-10. In the top of the figure, light fragments with $1 \leq A \leq 4$ from 137 MeV/nucleon Ar + Au are fitted, while fragments with $1 \leq A \leq 4$ and $1 \leq A \leq 3$ from 393 MeV/nucleon Ne + U [SA 80] are fitted in the left and right lower sections, respectively. In addition to the results from this work, included in Figure V-10 are 35 MeV/nucleon C + Au [WE 84], 241 and 393 MeV/nucleon Ne + U [SA 80], and 2.1 GeV/nucleon Ne + Pb [NA 81]. The average value of S/A for fragments with $1 \leq A \leq 3$ and $1 \leq A \leq 4$ are 4.24 ± 0.32 and 3.60 ± 0.12 , respectively, independent of the incident energy and projectile nucleus. These values can be compared to the entropies extracted from the deuteron to proton ratios, where $S/A = 4.7$ was deduced.

The difference between the entropy extracted using the same quantum statistical model compared to light particle cross sections and cross sections for fragments with $1 \leq A \leq 14$ appears to be a paradox because these fragments seem to have common origins. The apparent temperatures of these fragments are similar to each other at a given bombarding energy, while the extracted source velocities vary from 0.5 times the projectile velocity for $A \leq 3$ to 0.3 times the projectile velocity for the heavier fragments. However, the present light particle inclusive data include contributions from more peripheral collisions, where the small number of nucleons contained in the interaction volume between the two nuclei excludes the formation of heavy fragments. The macrocanonical approach inherent in the quantum statistical

MSU-83-617

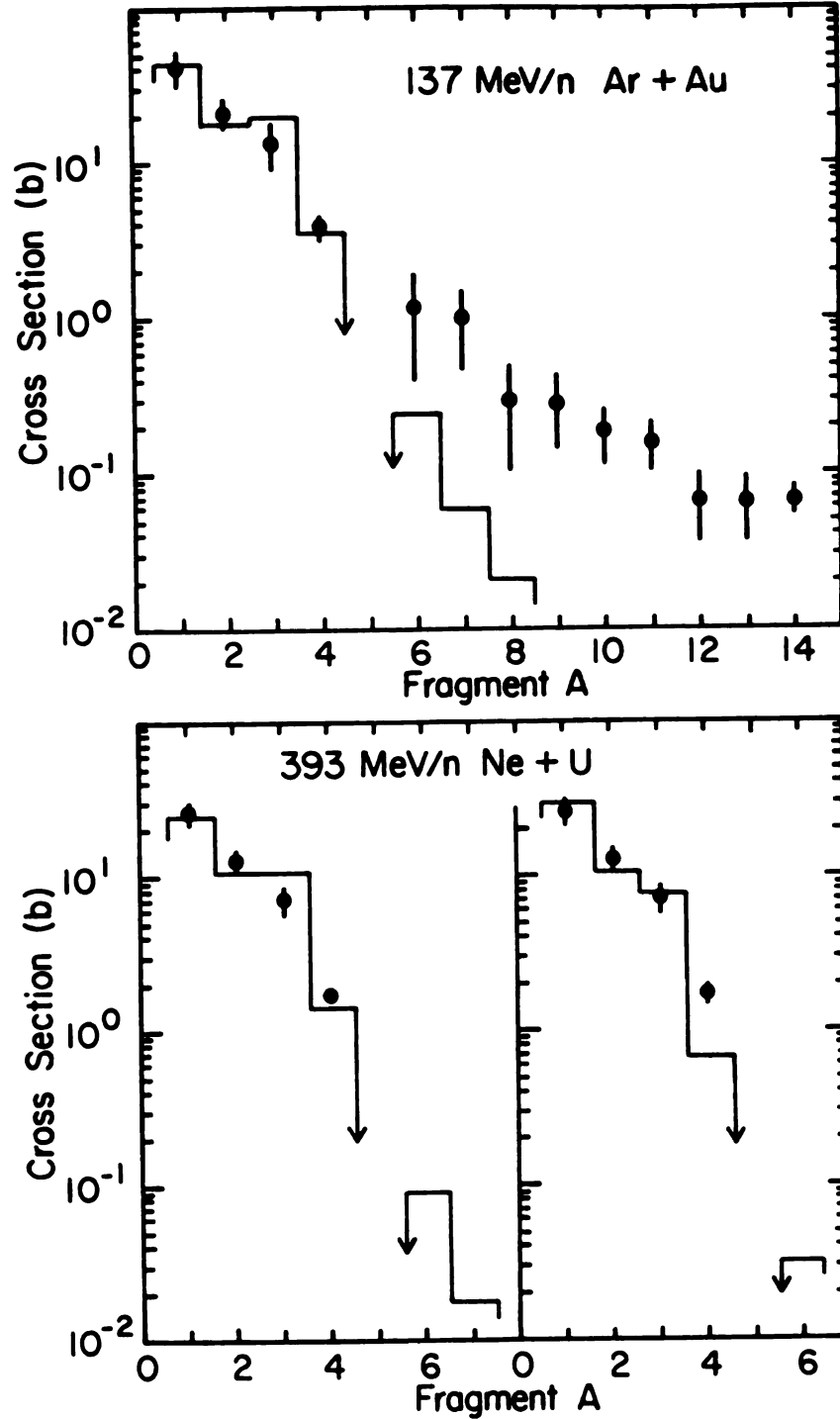


FIGURE V-10. Intermediate rapidity fragment distributions, and quantum statistical model results. In a) and b) fragments with $1 \leq A \leq 4$ are fitted, while in c) only fragments with $1 \leq A \leq 3$ are fitted.

model requires many particles in the system and is inappropriate for peripheral collisions. In contrast, the thermodynamic limit is approached for near-central collisions, which is where the heavier fragments are produced [WA 83]. In fact, even when only light particles were used to extract S/A, the entropy was found to be lower when central collisions were selected [GU 83]. This provides further evidence that to learn about S/A from intermediate and high energy nucleus-nucleus reactions it is necessary to include complex fragments as well as light particles.

E. COALESCENCE MODEL

An alternative description of the formation of complex nuclei in heavy ion collisions is by final state interactions, or coalescence of emitted nucleons [GU 76, GO 77]. The coalescence model assumes that the system is in thermal and chemical equilibrium [GO 78], and determines the probability for coalescence of nucleons within a sphere in momentum space. The probability of finding a nucleon in a sphere of momentum radius p_0 , centered at p is

$$P = \left(\frac{4}{3} \pi p_0^3\right) \frac{d^3 \sigma(p)}{dp^3} \quad (V-25a)$$

where $d^3\sigma(p)/dp^3$ is the cross section for emission of a single nucleon. Then the probability for finding A nucleons is just

$$P_A \approx \left(\frac{4}{3} \pi p_0^3\right) \left(\frac{d^3\sigma(p)}{dp^3}\right)^A \quad (\text{V-25b})$$

Any nucleons within p_0 of each other coalesce to become a composite nucleus. To obtain the cross section for the emission of a nucleus we take the probability of finding (A-1) nucleons in the sphere p_0 and multiply by 1/A times the cross section for emission of the additional particle. The final expression is

$$\frac{d^3N(Z,N)}{dp^3} = \left(\frac{N_T + N_P}{Z_T + Z_P}\right) \frac{1}{N!Z!} \left(\frac{4\pi}{3} p_0^3\right)^{A-1} \left(\frac{d^3N_p}{dp^3}\right)^A \quad (\text{V-26})$$

The $N_T + N_P$ and $Z_T + Z_P$ are the number of neutrons and protons in the target and plus projectile. The Z and N without subscripts are the proton and neutron number of the composite nucleus. Equation (V-26) has been used to extract the size of the coalescence sphere by finding a value for p_0 . One might expect the value of the coalescence radius to fall somewhere in the vicinity of the Fermi momentum of the nucleus, 260 MeV/c, or the average momentum of a nucleon inside the nucleus, which is about 200 MeV/c.

The coalescence model has been successfully used to describe light particle inclusive data both for relativistic

[GO 77, LE 79] and 20 MeV/nucleon [AW 81a] reactions. Figures V-11 and V-12 show the energy spectra for fragments ranging from protons through nitrogen at 30° and 90°, respectively. The regular change in the slopes of the spectra with fragment mass leads one to suspect that the heavier fragments may be described by powers of the observed proton spectrum. In fact, fragments through ${}^7\text{Be}$ were described using the coalescence formalism for 400 MeV/nucleon collisions [GO 77].

In order to extract the radius p_0 , we used

$$\frac{d^3 N}{dp^3} = \frac{1}{\sigma} \frac{d^3 \sigma}{dp^3} \quad (\text{V-27a})$$

and

$$P_A = Ap \quad (\text{V-27b})$$

where p is the momentum of the proton. Then

$$\frac{d^2 \sigma_A}{p_A^2 dp_A d\Omega} = \frac{C}{A^3} \left(\frac{d^2 \sigma_p}{p^2 dp d\Omega} \right)^A \quad (\text{V-28a})$$

where

$$C = \left(\frac{N_T + N_P}{Z_T + Z_P} \right)^N \frac{1}{N! Z!} \left(\frac{4\pi}{3} \frac{p_0^3}{\sigma} \right)^{A-1} \quad (\text{V-28b})$$

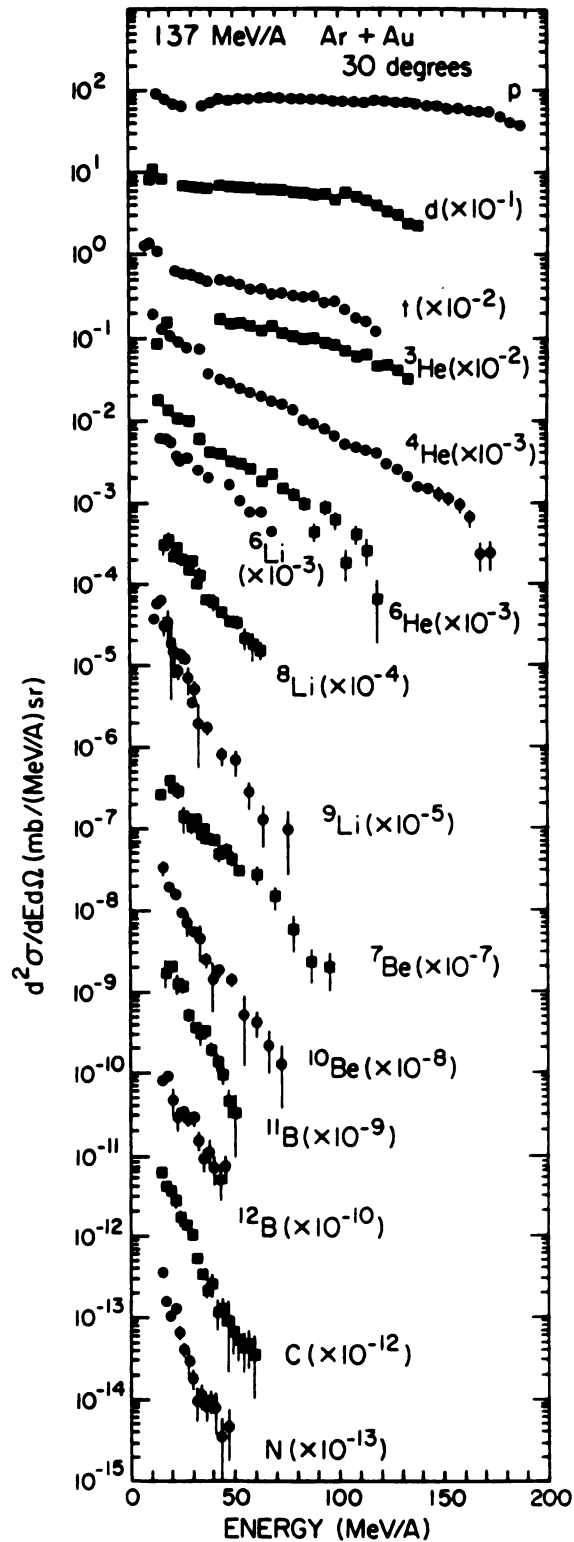


FIGURE V-11. Energy spectra at 30° of fragments from 137 MeV/A Ar + Au.

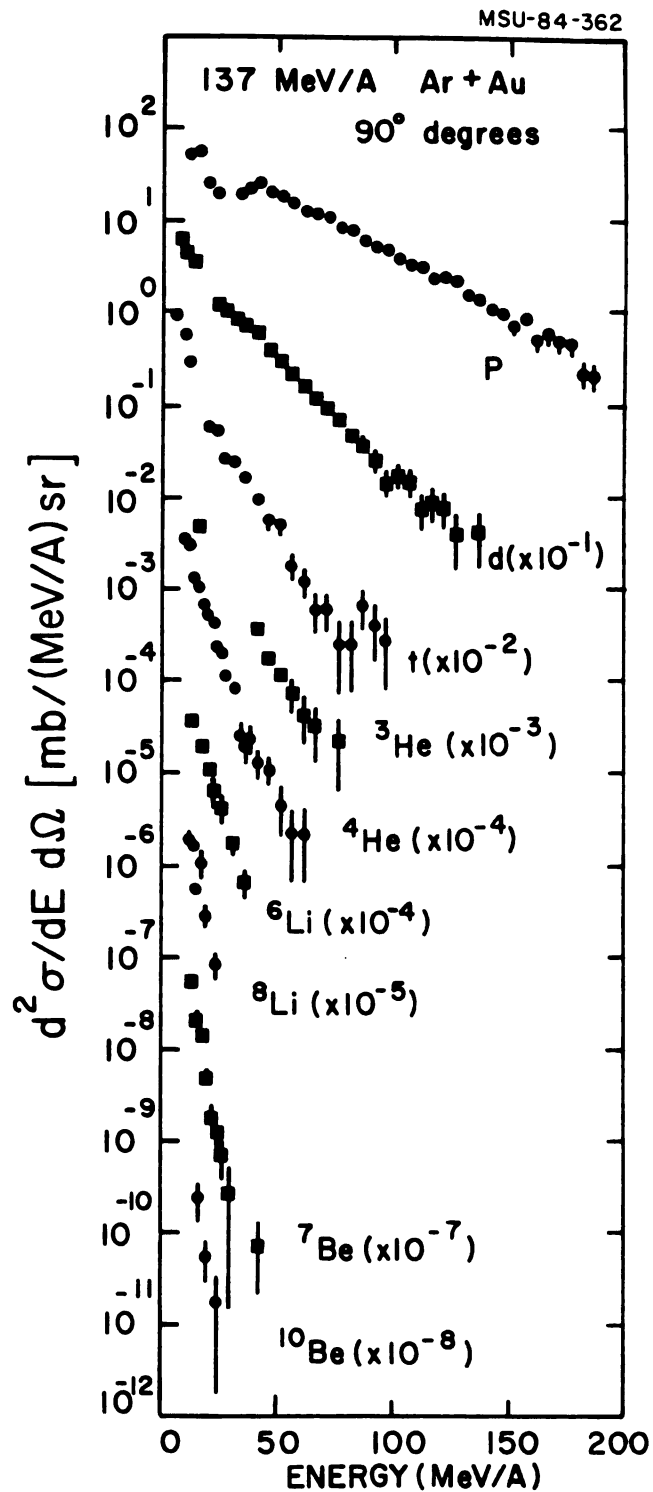


FIGURE V-12. Energy spectra at 90° of fragments from 137 MeV/A Ar + Au.

In performing the fit to the data, we used the measured proton and fragment cross sections $d^2\sigma/dE d\Omega$ and fit all angles simultaneously, using

$$\frac{d^2\sigma_A}{P_A dE_A d\Omega} = \left(\frac{N_T + N_P}{Z_T + Z_P} \right) \frac{1}{A^2 N! Z!} \left(\frac{4\pi}{3m\sigma_0} p_0^3 \right)^{A-1} \left(\frac{d^2\sigma_p}{pdE d\Omega} \right) \quad (V-29)$$

As the data were weighted according to the statistical error bars, and we wished to use the high energy tails of the spectra to learn about the coalescence radius, it was necessary to apply a cutoff on the data to be fit. This cutoff was set to 30 MeV/nucleon.

Figure V-13 shows the results of coalescence model fits to the deuteron spectra for the Ar + Au and Ar + Ca reactions at 42, 92, and 137 MeV/nucleon. The solid lines are coalescence spectra resulting from a least squares fit of the ratio of $(d^2\sigma/pdE d\Omega)$ to the measured deuteron cross sections, shown by the points. It is clear that the data are quite well fit for all six beam-target combinations. The same fitting procedure was applied to the heavier fragments as well; as an example of the fits for heavier fragments, the result for ${}^7\text{Be}$ from 137 MeV/nucleon Ar + Au is shown in Figure V-14. The high energy tails of the spectra are reasonably well fit by the procedure, but the lines derived from the proton spectra are much steeper at low energies than the observed ${}^7\text{Be}$ spectra.

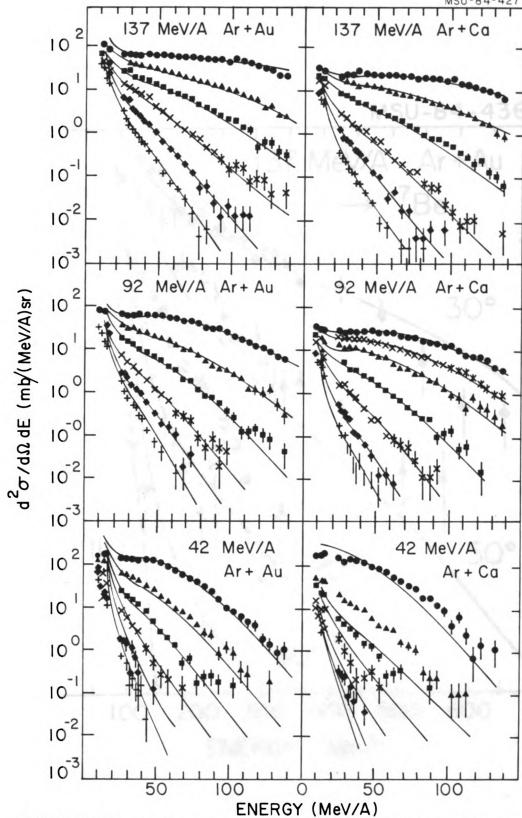


FIGURE V-13. Coalescence model fits to the deuteron spectra from argon induced reactions. The angles shown are 30, 50, 70, 90, 110, and 130°; all angles were fitted with a single coalescence radius.

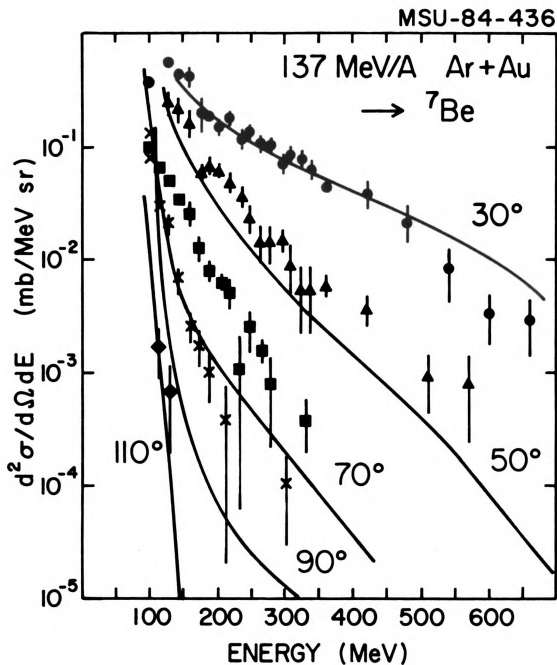


FIGURE V-14. Coalescence model fit to the ${}^7\text{Be}$ spectrum from 137 MeV/A Ar + Au. The angles shown are 30, 50, 70, and 90°; all angles were fitted with a single coalescence radius.

The coalescence model works quite well for fragments even as heavy as nitrogen. In Figure V-15, the results for 30° and 90° spectra for a range of fragments is shown. The fits to the high energy tails are quite good for all fragments at 30°, and are reasonable through ${}^{10}\text{Be}$ at 90°. The fact that the coalescence assumptions yield correct spectral shapes for the higher mass fragments supports statistical models, which allow fragment formation by distributing nucleons in phase space. The values of the coalescence radii, shown in Figure V-16, are relatively constant with fragment mass, further supporting a similar formation mechanism for light nuclei and complex fragments. The average values of p_0 are 154 MeV/c for 137 MeV/nucleon Ar + Au, 158 MeV/c for 137 MeV/nucleon Ar + Ca, 155 MeV/c for 92 MeV/nucleon Ar + Au, and 156 MeV/c for 92 MeV/nucleon Ar + Ca.

Since it represents the radius of a sphere in momentum space corresponding to each fragment, the p_0 must reflect an intrinsic property of the fragment. It should, however, be noted that p_0 contains other implicit factors [ME 78]. One such factor is a spin alignment factor which would account for the necessity of not only having momenta aligned but also spin aligned to give the correct spin of the composite nucleus. For light nuclei which have no excited states this factor is just $(2S + 1)/2$, where S is the spin of the ground state of the composite. Another factor arises from the fact that the composite particle has a momentum $p_A = Ap_p$ so that

MSU-84-435

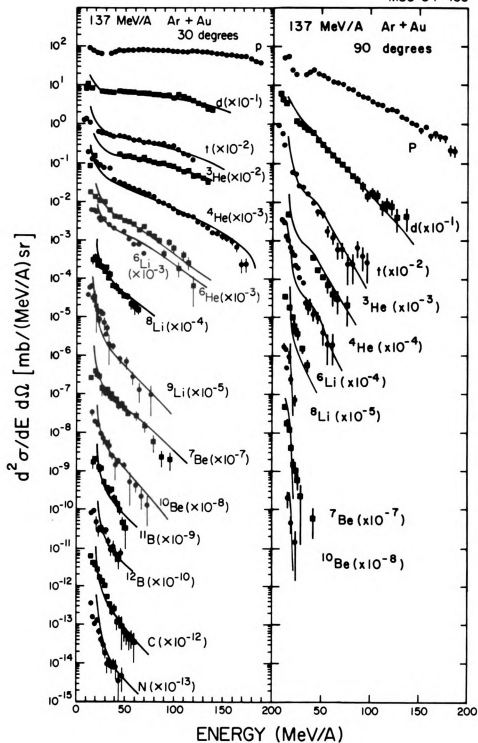


FIGURE V-15. Coalescence model results for fragment spectra at a) 30° and b) 90°.

MSU-84-428

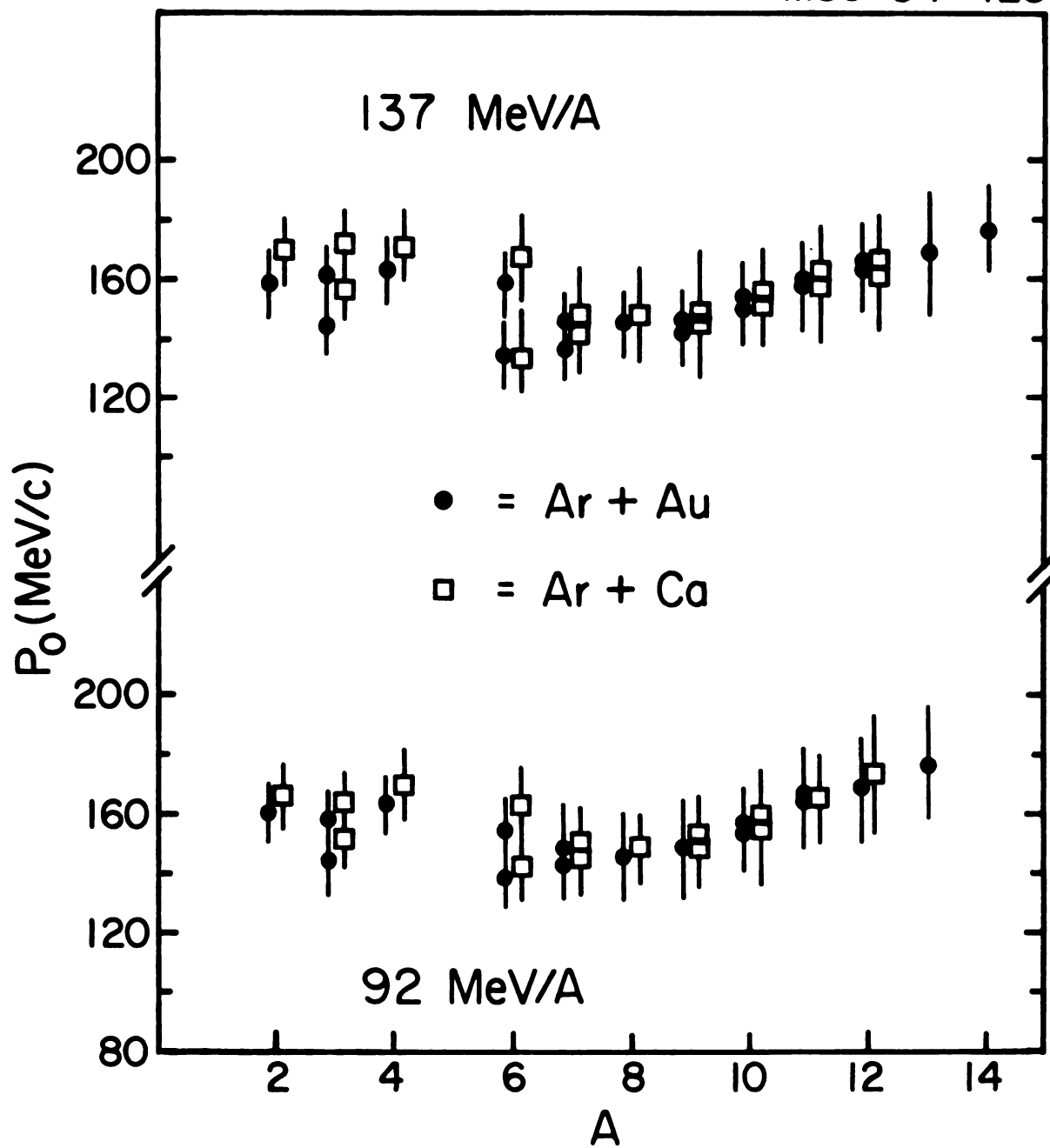


FIGURE V-16. Coalescence radii extracted from fragment spectra, as a function of fragment mass.

$d^3 p_A = A^3 d^3 p_p$. We therefore define a new \tilde{p}_0 which explicitly removes the spin alignment factor and phase space factor from p_0 by

$$(p_0^3)^{A-1} = A^3 \frac{2S+1}{2^A} (\tilde{p}_0^3)^{A-1} \quad (V-30)$$

It is possible to relate this coefficient \tilde{p}_0 to the size of the thermal system at the freeze-out density. This relation is given by

$$V = (Z!N! e^{E_0 k\tau})^{1/A-1} \left(\frac{3h^3}{4\pi\tilde{p}_0^3} \right) \quad (V-31)$$

where E_0 is the binding energy of the ground state composite particle and $k\tau$ the temperature of the system. As $E_0 \ll k\tau$, the term $(e^{E_0 k\tau})^{1/A-1}$ has been replaced by 1. Using

$$V = \frac{4\pi}{3} R^3 \quad (V-32a)$$

and

$$Mc = 197 \text{ MeV fm} \quad (V-32b)$$

we can calculate the radius from

$$R^3 = (Z!N!)^{1/A-1} \left(\frac{9\pi^2}{4} \right) \left(\frac{197}{p_0} \text{ fm}^3 \right) \quad (V-33)$$

Table V-1 gives the p_0 , \bar{p}_0 , and R values for typical light (deuteron) and heavy (^{12}C) fragments from the four beam-target combinations. The light particles yield a source radius of 5.5 fm, and the heavy fragments yield a radius of 4.5 fm. These radii should be compared to results from relativistic collisions: $R \approx 5.0$ fm [ME 77, ME 78] or 3.4-4.3 fm [LE 79], extracted by a similar coalescence approach, $R=5.3$ fm from two-pion interferometry experiments [FU 84], and the radii extracted for central collisions at 400 MeV/nucleon: $R=4.7$ fm for Nb + Nb and $R=4.0$ fm for Ca + Ca [GU 84]. For intermediate energy reactions, source radii of 4 fm and 8 fm have been extracted for 25 MeV/nucleon ^{16}O + Au reactions from p-p and d-d correlations, respectively [LY 83, CH 84]. These analyses provide a reasonably consistent picture of the reaction: a local thermalized region is formed in the reaction, and it expands to a radius of 4-5 fm where the various fragments no longer interact.

Table V-1. Values for coalescence and source radii for typical light and heavy fragments from Ar-induced reactions.

REACTION	PARTICLE	$P_0 (\frac{\text{MeV}}{c})$	$\bar{P}_0 (\frac{\text{MeV}}{c})$	R (fm)
137 MeV/A Ar + Au	d	154	85	5.6
	^{12}C	154	158	4.5
137 MeV/A Ar + Ca	d	158	88	5.4
	^{12}C	158	162	4.4
92 MeV/A Ar + Au	d	155	86	5.5
	^{12}C	155	159	4.5
92 MeV/A Ar + Ca	d	156	86	5.5
	^{12}C	156	160	4.4

CHAPTER VI

DYNAMICAL MODELS

A. BOLTZMANN EQUATION

The very different results from time-dependent Hartree-Fock and fluid dynamical calculations at intermediate bombarding energies [ST 80] shown in Figure I-4 underscore the transitional nature of this energy regime. The TDHF calculations, dominated by the effects of the mean field, exhibit transparency, while fluid dynamics predicts the formation of a compound excited system [ST 80] followed by rapid disintegration. There is an obvious need to include both single-particle viscosity from the interaction of nucleons with the nuclear mean field and two-particle viscosity due to nucleon-nucleon collisions in a realistic theory appropriate for this energy region [GR 84].

1. HIGH ENERGY CASCADE MODELS

In order to put together a microscopic description of these collisions, we have turned to the Monte Carlo methods used in intranuclear cascade calculations appropriate to high energy collisions [BE 76, YA 79, YA 81, CU 81, CU 82, CU 82a, TO 83]. In this approach, nuclei are approximated by a collection of point particles, each representing a nucleon. In setting up the initial nuclei, each particle is given a random position and a random momentum vector such

that
$$|\bar{r}_j - \bar{r}_{\text{proj}\{\text{targ}\}}| \leq R_{\text{proj}\{\text{targ}\}} \quad (\text{VI-1a})$$

and
$$|\bar{p}_j - \bar{p}_{\text{proj}\{\text{targ}\}}| \leq p^{\text{Fermi}} \quad (\text{VI-1b})$$

resulting in nuclei having the right size and Fermi momentum.

Nuclear collisions are treated as a superposition of independent collisions of the point nucleons. The nucleons move on straight line trajectories until they collide; the probability of a collision between two nucleons is given by the free nucleon-nucleon scattering cross sections. A collision takes place if

$$\min\{|\bar{r}_i - \bar{r}_j|\} \leq \left(\frac{\sigma([p_i + p_j]^2)}{\pi} \right)^{1/2} \quad (\text{VI-2})$$

where the left hand side of the equation represents the minimum distance between the two nucleons. The properties of the exit channel are chosen randomly, weighted by the experimental partial cross sections, within the constraint of energy and momentum conservation. An isotropic angular distribution is assumed for the inelastically scattered particles, while a parameterization of the experimental angular distributions is used for elastic scattering. The time evolution of the system is followed until the interactions cease. The quantum mechanical nature of the problem is recovered by averaging the final result over many ensembles with different initial nucleon positions and

momenta, and different random choices for the outcomes of the two-nucleon collisions.

The intranuclear cascade approach has been extensively tested for high energy proton and heavy ion induced reactions. The intranuclear cascade code of Cugnon is able to reproduce the inclusive proton and pion spectra and the observed proton-proton correlations for 800 MeV/nucleon reactions [CU 80a], although the low energy pion cross sections are somewhat underpredicted. Yariv and Fraenkel have also predicted the nucleon spectra [YA 79], although they do not differentiate between nucleons which are bound in complex fragments and those which are not, and therefore overpredict the proton cross sections for lower bombarding energies (i.e. $E_{LAB}=250$ MeV/nucleon). The predicted pion spectra have the correct slopes, but the cross sections are overpredicted, possibly due to the simplified approach to pion absorption in the code [YA 79]. The Yariv-Fraenkel code has also been modified to include antinucleon-nucleon cross sections [CL 82], and is being used to investigate \bar{p} -nucleus collisions.

An intranuclear cascade calculation followed by deexcitation of the excited residual nuclei has been recently tested by Toneev and Gudima [TO 83]. This approach correctly predicts the inclusive proton and pion spectra, as well as the shapes of the events as determined by 4π analysis. This calculation has also been used to determine

the entropy generated during the collision, and values of $S/A = 2.7, 3.3,$ and 4.4 were found for collisions at 400, 800, and 2100 MeV/nucleon, respectively [TO 83]. A similar cascade step, followed by chemical equilibrium among the participant nucleons also was found to explain the p, d, t, and π -spectra for 800 MeV/nucleon Ar + KCl [MA 80, MA 83].

The intranuclear cascade may be viewed [CU 82a] as a solution of the Boltzmann equation for relativistic collisions. The Boltzmann equation is a kinetic equation derived to describe a dilute gas of classical point particles interacting through a repulsive potential [BA 75a]. It includes mean field and collision terms. However, in the limit of relativistic nuclear reactions, the classical collision term dominates the single particle distribution. The mean field term is much less important in this case, and is not included in intranuclear cascade calculations.

In order to apply the Boltzmann equation for intermediate energy reactions, we must take the mean field term into account, and replace the classical collision integral by the Uehling-Uhlenbeck collision terms [UE 33], which respect the Pauli principle. The equation for the rate of change in time of the single particle distribution function, f , is then given by [TA 81, WO 82, BE 84]

$$\frac{\partial}{\partial t} f + \vec{v} \cdot \frac{\partial}{\partial \vec{r}} f + \vec{a} \cdot \frac{\partial}{\partial \vec{v}} f = \int \frac{d^3 p_2 d^3 p_1 d^3 p_1'}{(2\pi)^6} \sigma v_{12} \times$$

$$\times [ff_2(1-f_1)(1-f_2) - f_1f_2(1-f)(1-f_2)]\delta^3(p+p_2-p'_1-p'_2). \quad (\text{VI-3})$$

The time evolution of f is due to two distinct causes: the free motion of the particles and the interparticle collisions. The potential field serves to keep the system from expanding before collisions occur. The motion of the test particles under the influence of this mean field alone is governed by the left hand side of this equation set equal to zero. This gives the Vlasov equation, which has been used to simulate collisions at very low bombarding energies.

In the following sections, we review the implementation of the additional terms into the Monte Carlo framework provided by the intranuclear cascade approach. Our calculation follows most closely the method of Cugnon [CU 80a], and the extensions made by Bertsch, Das Gupta and Kruse [BE 84].

2. NUCLEON-NUCLEON CROSS SECTIONS

Our goal was to produce a generally applicable microscopic theory which could be used for asymmetric as well as symmetric systems. We have therefore incorporated protons, neutrons, deltas and pions of different isospin separately with their experimentally determined scattering cross sections. In contrast to the high energy nuclear cascade models, we wish to carry out calculations for bombarding energies as low as ~ 40 MeV/nucleon, and so must deal with low energy nucleon-nucleon collisions [KR 84a].

We have extended the tabulated scattering cross sections in our code to include the correct details for two-particle collisions at rather low energies.

Figure VI-1 shows the total cross sections for p-p and p-n reactions. The points correspond to experimentally determined values from the literature, the thin line is a smoothed curve through the values, while the heavy line corresponds to a parameterization of the data. In the code, we have used a cross section table, containing the smoothed values, with a linear interpolation between table entries. The elastic scattering cross sections are likewise contained in a lookup table, and the inelastic scattering cross sections are computed from the total and elastic values by subtraction. The selection of the inelastic reaction channel from the among the possible isospins of the final states is determined by branching ratios calculated from the Klebsch-Gordan coefficients. Our calculation includes pion production, and also the pion absorption cross sections as determined from detailed balance [CU 82].

3. PAULI BLOCKING

Once it has been determined that two nucleons pass close enough to one another to undergo a collision, a decision must be made whether the collision will actually take place, or whether it will be Pauli blocked. This decision is made by computing the factors $(1-f)(1-f)$ [BE 84].

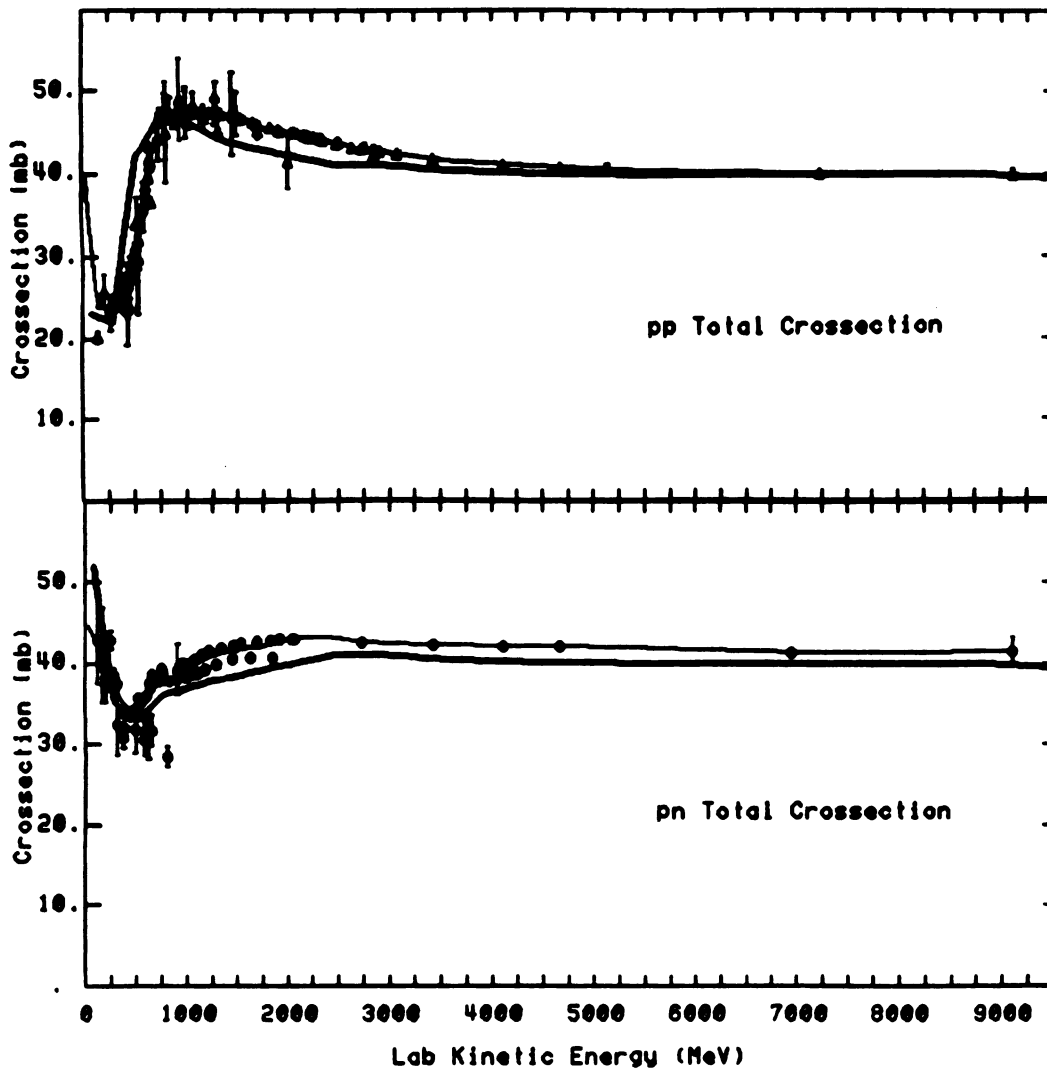


FIGURE VI-1. Nucleon-nucleon total cross sections used to determine collision probabilities in the Boltzmann equation model.

To allow calculation of f for the final state of each particle, a radius \tilde{r} in configuration space, and a radius \tilde{p} in momentum space are defined in the initialization step of the calculation. These radii are chosen to define a six dimensional sphere containing N nucleons in the initial system (i.e. at normal nuclear matter density).

$$N = \frac{4}{(2\pi\hbar)^3} \times \frac{4}{3} \pi \tilde{r}^3 \times \frac{4}{3} \pi \tilde{p}^3 \quad (\text{VI-4})$$

In this work N was chosen to be 4 particles. The number used for N is the result of a compromise between the need for small radii to insure a uniform local density, and the need for large N to reduce statistical errors in counting the nucleons in the sphere.

Once the phase space coordinates of the scattered particles are determined, the particle density in the six dimensional sphere of radius \tilde{r} in configuration space and radius \tilde{p} in momentum space is computed. In order to minimize the statistical error in this density, we use an ensemble averaged density, requiring simulation of multiple collisions simultaneously. The calculations reported here have been performed using 15 simultaneous collisions. The number of particles in the sphere is compared to the 4 particles expected in normal nuclear matter; the ratio of these two numbers gives the occupation (or blocking factor)

f , and the collision probability factor $(1-f)$. This factor should be in the range $0 \leq (1-f) \leq 1$, and the blocking is determined in the calculation through comparison to a random number $0 \leq X \leq 1$. If $X < f$, the collision is Pauli blocked, whereas if $X > f$ the collision is allowed to occur. We found that as the bombarding energy was lowered, a large fraction of the attempted collisions were Pauli blocked. For the Ar + Ca system 80 % of collisions at 137 MeV/nucleon, 83 % of collisions at 92 MeV/ nucleon and 90 % of the attempted collisions at 42 MeV/ nucleon were blocked.

It can happen that the nucleons within the sphere are very non-uniformly distributed, for example when the test particle is near the surface of the nucleus. In this case, part of the test sphere extends beyond the nucleus and contains no particles. This situation is detected by comparing the location of the center of mass of the nucleons within the test sphere to the location of the center of the sphere. If the two are found to be very different the test volume is recalculated, removing a pole cap with the volume of the unoccupied space from the sphere. With this correction, the Pauli blocking mechanism was found to be 96% efficient.

4. MEAN FIELD TERM

A constant time-step integration routine is used to insure synchronization of the ensembles [KR 84, BE 84]. Within each synchronization time-step (increments of 0.5

fm/c, or 1.0 fm/c for the lower energies, are used) a time-matrix [CU 81] is constructed, i.e. all particles are transported in smaller time intervals to the (lab)-time of the next collision before that collision is allowed to take place. The trajectories of the particles are not straight, as in the high energy cascade models, but are curved because of the influence of the mean field.

The acceleration of the test particles due to the field gradient is calculated at the beginning of each time-step, and is recalculated for the collision partners prior to further transport. The force due to the field is assumed to be constant within a synchronization time-step, however the acceleration does change abruptly at the boundary between time-steps. The local gradient of the field at each test particle is computed via the difference between the particle densities in two hemispheres centered around the test particle.

$$\frac{\rho_{\text{left}} - \rho_{\text{right}}}{3/4 R} = \Delta\rho \text{ for } R=R_x, R_y, R_z \quad (\text{VI-5})$$

We have used the radius $R=2$ fm for the hemispheres. To decrease the statistical error in the computed densities, ensemble averaging of the test spheres is used. This averaging results in a reasonably smooth (about 10% fluctuation at normal density) single particle distribution function.

The density dependent potential field $U(\rho)$ is given by a local Skyrme interaction:

$$U(\rho) = -124 \rho/\rho_0 + 70.5(\rho/\rho_0)^2 \text{ MeV} \quad (\text{VI-6})$$

with a compressibility coefficient of $K=375$ MeV. It should be noted that U , which is a microscopic quantity describing the behavior of single particles, is directly related to the nuclear equation of state, a macroscopic relation, via

$$U = \frac{\partial(\rho E)}{\partial \rho} \quad (\text{VI-7})$$

Figure VI-2 indicates that the field does indeed hold the nuclei together. The top of the figure shows the spatial distribution of the nucleons in the nucleus, and the bottom section shows the momentum distribution. The solid lines show the initial distributions, and the dashed lines show the particle distributions in the absence of collisions, 40 fm/c later. It is quite clear that the particles are still inside the nuclei after 40 fm/c, and that the spatial and momentum distributions bear close resemblance to the initial conditions.

Figure VI-3 shows sample results from the calculation once nucleon-nucleon collisions are allowed to take place. The system is 42 MeV/nucleon Ar + Ca, with an impact parameter of 0 fm (a head-on collision) in the left hand side of the figure, and $b=5$ fm, or a peripheral collision,

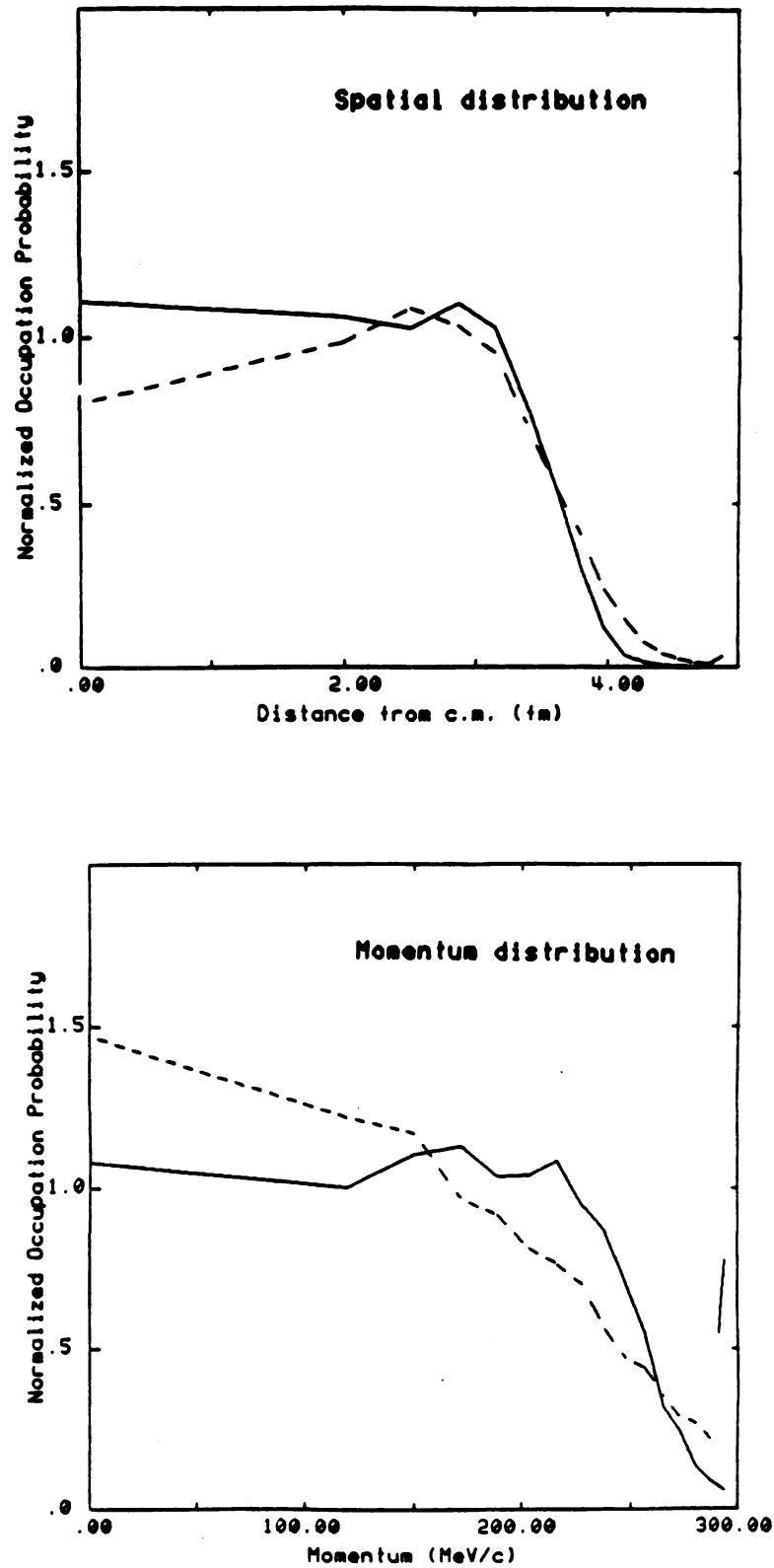


FIGURE VI-2. Spatial and momentum distributions of nucleons inside the nuclei at $t=0$ (solid lines) and $t=40$ fm/c (dashed lines) under the influence of the mean field term alone.

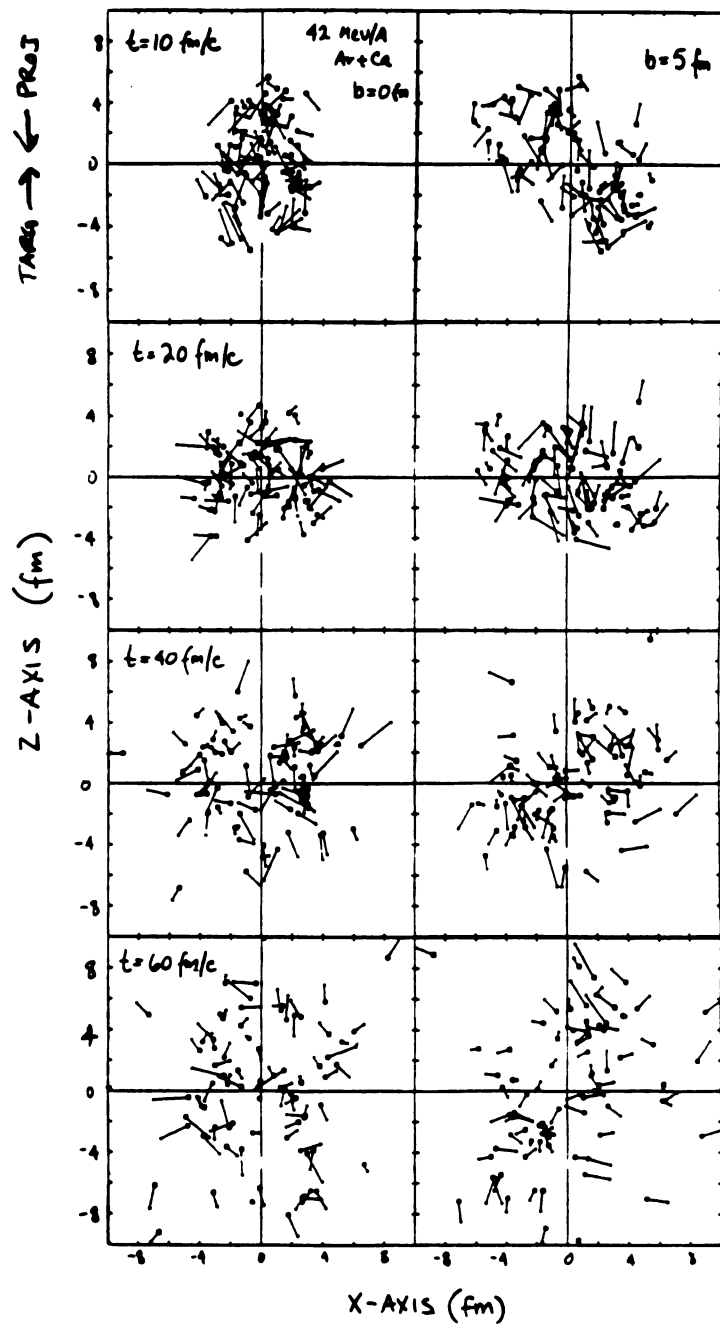


FIGURE VI-3. Particle positions and momenta (indicated by the arrows) for 42 MeV/A Ar + Ca collisions at $b=0$ and $b=5$ fm. The time development of the reaction from $t=10$ fm/c to $t=60$ fm/c is shown.

on the right side. The points show the locations of the nucleons in the center of mass x-z plane, where the projectile and target approach each other in the negative and positive z direction, respectively. The arrows show the motion of the nucleons: the length of each arrow is proportional to the momentum of the nucleon. The rather chaotic appearance of the momenta, even at times early in the collision, is due to the Fermi momentum of the nucleons. The time development of the reaction is given in the vertical direction: the top frames show the particle distributions at 10 fm/c, the second frames at 20 fm/c, the third at 40 fm/cm and the bottom at 60 fm/c.

The central collision leads to a rather high density of particles in the central region at 20 fm/c, when the nuclei almost overlap. The later frames show an almost isotropic emission of the nucleons from this region; the time development is consistent with the formation of a compound system which subsequently explodes. On the right side of the figure, the peripheral collision looks quite different. Large fragments of the projectile and target remain clustered together throughout the collision, with particles from the region of overlap emitted mostly to the side.

5. GENERALIZED COALESCENCE

After the collisions among the nucleons have ceased, the resulting positions and momenta must be sorted into particle spectra to compare with the experimental data. As the

calculation yields only information for individual nucleons and the cross section for production of light nuclei is a significant fraction of the total nucleon cross section, a method to discern light nuclear clusters or large spectator fragments from single nucleons must be employed. This treatment is especially important for intermediate energy collisions where the cross sections for formation of complex fragments are quite large [JA 83]. We have used a generalized six-dimensional coalescence model to find the nucleons bound in clusters and prevent them from contributing to the proton cross sections.

The rationale behind the generalized coalescence is very similar to the reasoning behind the coalescence model of Chapter V, but it is extended to configuration as well as momentum space. As the two-nucleon force is short-ranged, it should become negligible at a distance greater than 3 fm. If we define a cluster as a collection of nucleons which are interacting with each other, but not with the rest of the system, we can conclude that a nucleon belongs to a cluster if and only if it is closer than a distance r_0 to any one nucleon in the cluster. These clusters, however, can be excited, and in an excited fragment, those nucleons with momenta larger than some "escape momentum" will be emitted from the fragment. We therefore require that nucleons within a cluster do not have momenta which differ by more than p_0 from the cluster momentum.

The algorithm has been tested on initial collision configurations, where we should, of course, find two clusters - the projectile and the target. The spatial clustering was found to result in one large cluster, while the complete algorithm produced the correct result. These tests also indicated that reasonable values should be around 2-3 fm for r_0 , and 200-300 MeV/c for p_0 . The values for p_0 are considerably larger than those derived from light particle spectra (see Chapter V), or used to find light particles in a momentum space-only post-cascade coalescence [TO 83]. This may be due to the fact that these values of $p_0 \geq 200$ MeV/c were determined by producing nuclei of mass 40. We use the large p_0 as we are attempting to identify large as well as small nuclei via coalescence.

In practice, to perform the coalescence we first collect all the nucleons into clusters in configuration space. We then randomly choose a particle within each cluster, and add the other particles to it if their relative momentum is not too large. This process is iterative, and the cluster momentum is recalculated every time a particle is added to it. We have used $r_0 = 2.2$ fm and $p_0 = 200$ MeV/c in the analysis of the results reported here. These two parameters have been adjusted to yield correct total cross sections for the observed nucleons. The values are quite reasonable as they are in the vicinity of the distance between nucleons in normal nuclear matter, and the average momentum of a nucleon inside a nucleus.

It is important to note that the decay of excited clusters is not yet included, so the 6-d coalescence serves only to prevent bound protons from being counted as free protons in the detectors. The neglect of the cluster excitation energy also means that evaporation protons are absent in the calculated spectra.

6. COMPARISON WITH DATA

The code resulting from the changes described above has been tested by comparisons to high energy data. It was found to satisfactorily reproduce observed particle spectra. Figure VI-4 shows the comparison of protons emitted from 800 MeV $p + C$ reactions at 15, 30, 40, and 60 degrees. Data are represented by the points, and the calculation by the histograms. The statistical error in the calculation is indicated by the error bars shown on the histograms. The agreement of the calculation with the data is reasonable, although the elastic scattering of the protons to 15° is seriously underpredicted. Tests of the calculation for the $Ar + KCl$ system resulted in correct predictions of the pion multiplicity [KR 84], and the event shapes calculated for 400 MeV $Nb + Nb$ collisions were found to agree with shapes determined from 4π measurements [KR 84].

Calculations with this model have been performed for $Ar + Ca$ reactions at 137, 92, and 42 MeV/nucleon. The calculated neutron and proton distributions are practically identical, and have been combined to increase the

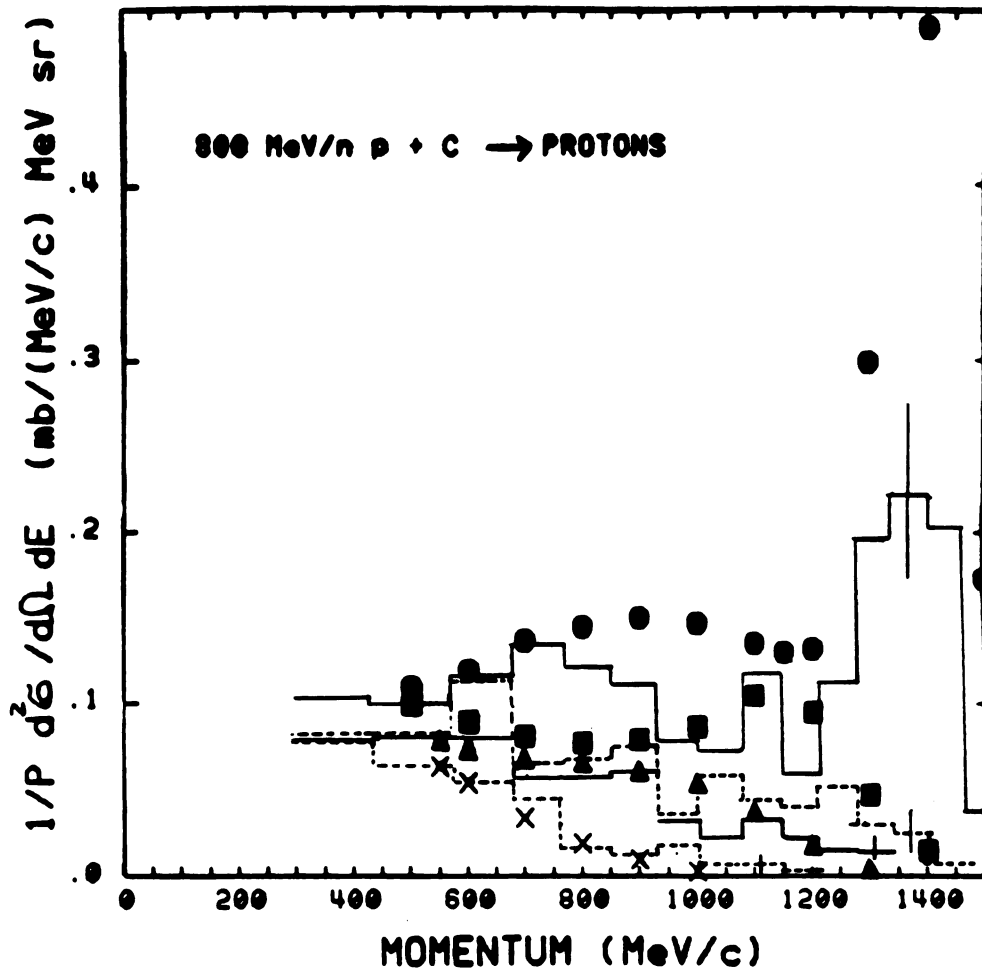


FIGURE VI-4. The results of the Boltzmann equation model for 800 MeV p + C. Inclusive proton spectra at 15°, 30°, 40°, and 60° are shown by the points, and the calculation by the histograms. Statistical errors in the calculation are indicated.

statistical certainty in the calculated double differential proton spectra. The solid lines in Figure VI-5 show the calculated angular distributions, after removal of bound nucleons, for protons emitted at the three bombarding energies. The observed angular distributions, indicated by the data points, are quite well reproduced by the calculation.

The upper section of Figure VI-6 shows the comparison between calculated and measured proton spectra for 137 MeV/nucleon Ar + Ca at the six laboratory angles between 30° and 130°. The calculated cross sections and slopes of the spectra agree reasonably well with the data. Production of high energy nucleons at 50° and 70° is underpredicted by a factor of 2. This same effect was found in a traditional intranuclear cascade approach applied to collisions at 1 GeV/nucleon [TO 83], where it was suggested that this may be due to hydrodynamic effects. The lower section of Figure VI-6 shows the same data compared to the proton spectra calculated with the intranuclear cascade model of Cugnon [CU 81]. The cascade serves as a useful reference in this case to demonstrate the importance of the mean field and phase space Pauli blocking for the intermediate bombarding energies. The cascade calculation includes a simple approximation to the Pauli blocking by excluding collisions with less than 24 MeV c.m. kinetic energy; the resulting nucleon momentum distributions were analyzed via the same procedure as the Boltzmann equation results, including the

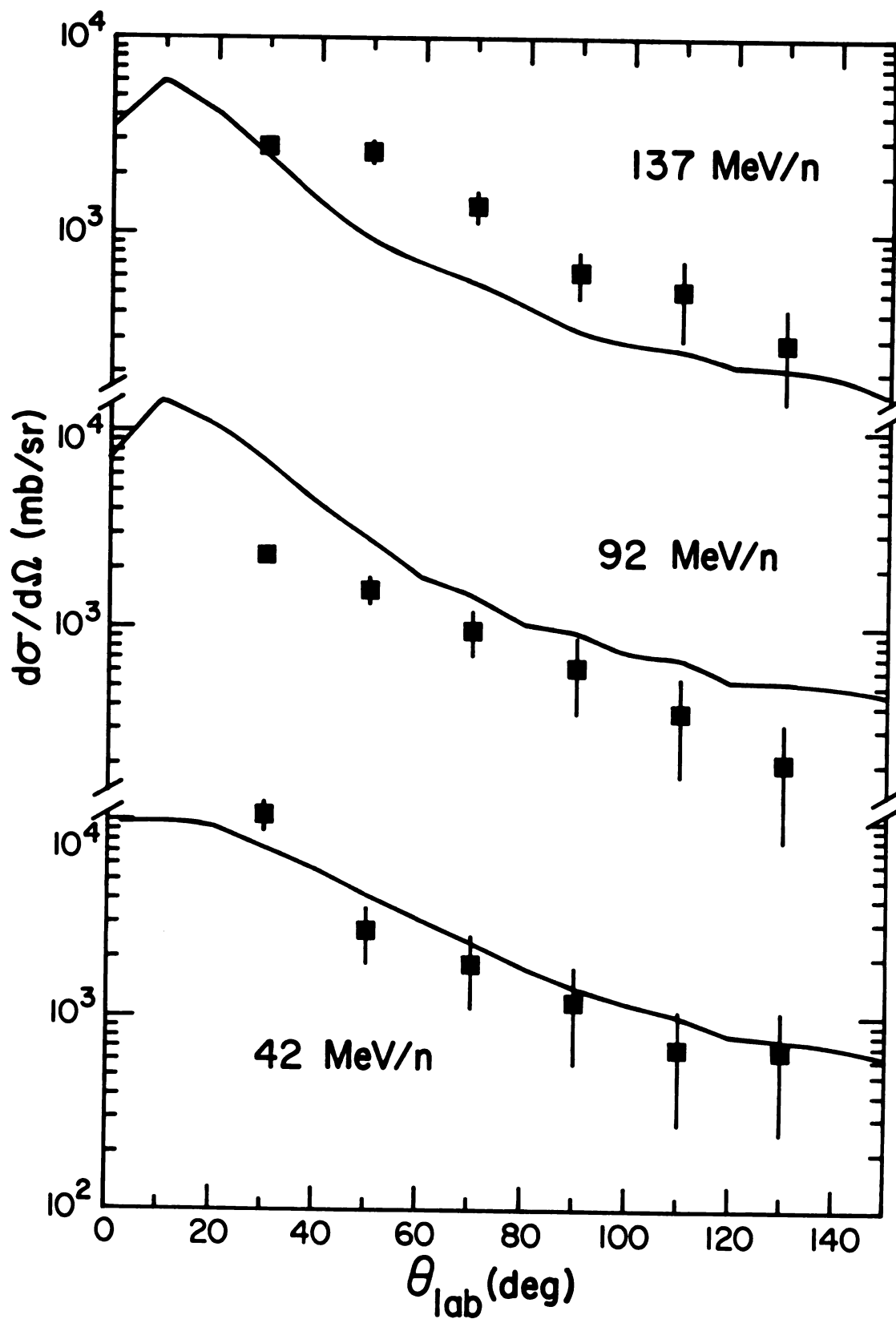


FIGURE VI-5. Inclusive proton angular distributions for Ar + Ca reactions. The data are indicated by the points and the Boltzmann equation results by the solid lines.

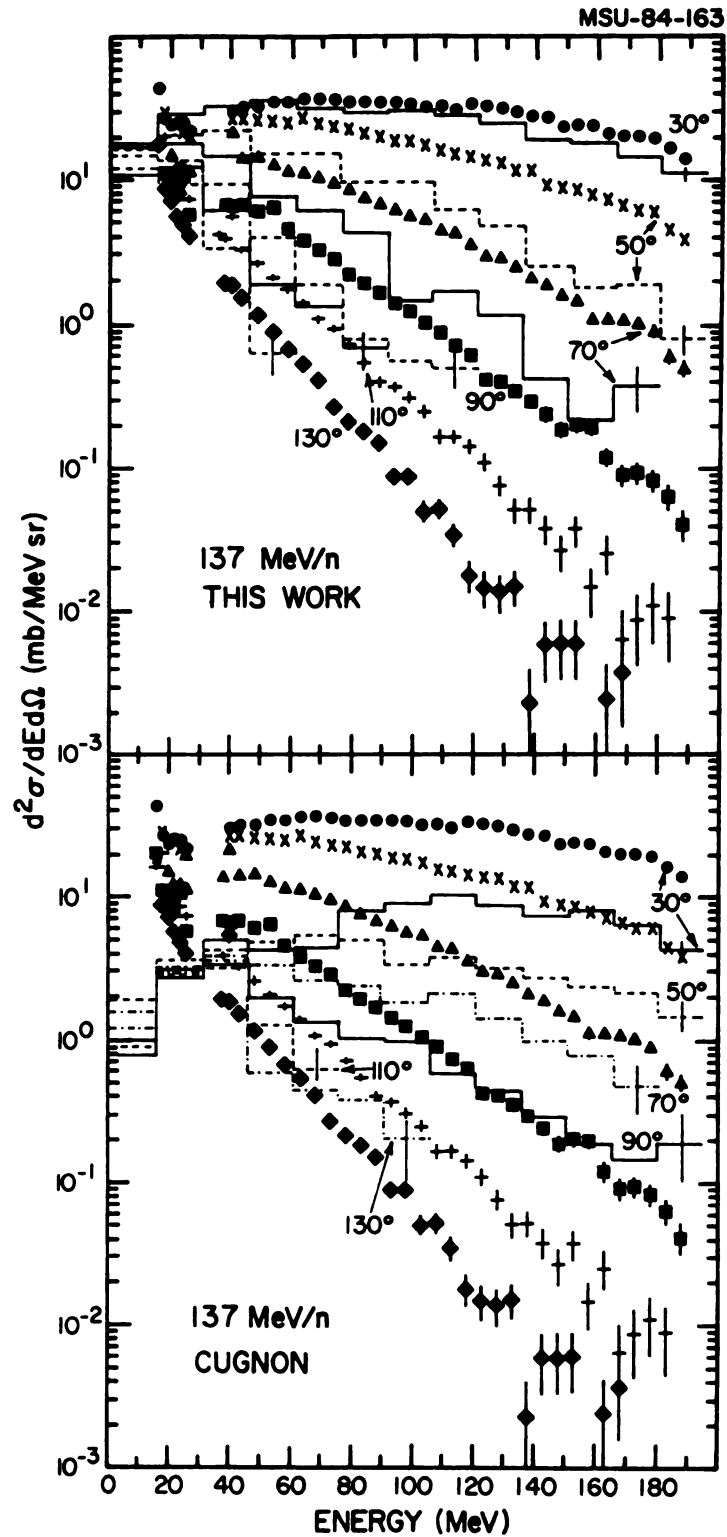


FIGURE VI-6. Inclusive proton spectra for 137 MeV/A Ar + Ca. The data are indicated by the points. a) the histograms show results of the Boltzmann equation calculation. b) the histograms are results obtained with the cascade model [CU 81]

coalescence step. Variation of the coalescence parameters was found to change the magnitude of the cross sections, but to have a negligible effect on the shape of the spectra. It is important to note that the same coalescence parameters were used in both sections of Figure VI-6. It is clear from the figure that the simple cascade simulation, though appropriate for high bombarding energies, cannot reproduce the medium energy data.

Figure VI-7 compares the Boltzmann equation calculation + coalescence step with the data for Ar + Ca at 92 and 42 MeV/nucleon in the top and bottom sections, respectively. The coalescence parameters used were the same as at the higher energy. At 92 MeV/nucleon, the calculations agree with the data; in particular the spectra at 50° and 70° are well reproduced, contrasting with the situation at the higher bombarding energy. The calculation at 42 MeV/nucleon agrees well with the data except for the 30° spectra, which are underpredicted at the lower proton energies. This is probably due to the neglect of proton evaporation from the clusters, which would dominate the projectile and target rapidity regions.

It is evident from these comparisons that the Boltzmann equation, including the nuclear mean field and Pauli blocking corrections to the collision terms, provides a useful approach to the dynamics of intermediate energy heavy ion collisions. We can use this model to study the effect of the collision term on the mean field dynamics, as the

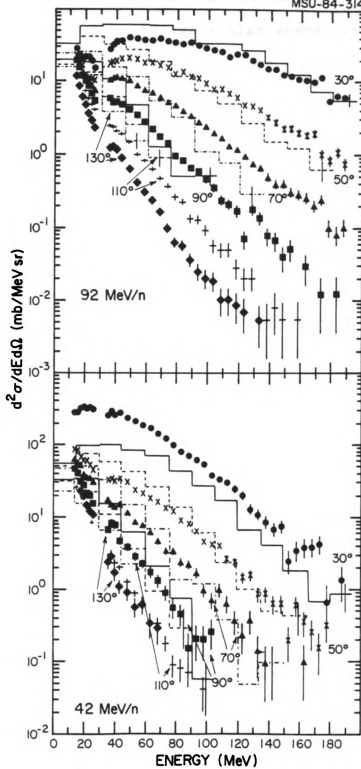


FIGURE VI-7. The Boltzmann equation calculation is compared to the proton spectra for a) 92 MeV/A Ar + Ca and b) 42 MeV/A Ar + Ca.

calculation may be used in the one extreme to mimic TDHF, and on the other hand to simulate a high energy intranuclear cascade model.

B. NUCLEAR FLUID DYNAMICS

There has been much discussion recently of the question of the mean free path, λ , of nucleons in intermediate energy reactions. There have been claims that for 50-150 MeV/nucleon reactions, λ should be large compared to the nuclear radius [SC 80, NE 81], and also conflicting claims that it must be smaller ($\sim 1-2$ fm) [CO 80]. It is clear that there is a great deal of uncertainty, and the question will only be answered by comparison of theories incorporating either assumption with the data. In this spirit we compare the results of a three-dimensional viscous hydrodynamical calculation, which assumes $\lambda \ll R$ [BU 81, BU 83] to our data. These data allow a systematic check on the applicability of nuclear fluid dynamics in the intermediate energy regime. This process has already begun with the comparison of calculated results to proton spectra from 84 MeV/nucleon C + Au [BU 83].

1. DESCRIPTION

The fluid dynamical calculations treat the nuclear matter in the collision as a viscous fluid in three dimensions. The calculation is carried out using a grid 0.5 fm on each side. For each grid element the classical fluid

dynamical equations are integrated including shear and bulk viscosity and heat conductivity [BU 81]. The nuclear binding is treated via Coulomb and Yukawa potentials [ST 80a].

The energy of the nucleons in the system can be divided into the kinetic and internal energy per nucleon [ST 79]. The internal energy is separated into two terms: E_T , the thermal energy resulting from the low temperature Fermi gas expansion and E_C , which includes the binding and compressional energy. A compression constant of 200 MeV was used, and the binding energy was -16 MeV/nucleon, the binding energy of normal nuclear matter. The pressure is calculated from the internal energy and separated into two parts as well, and analyses of hydrodynamical results have discussed the difficulty in isolating effects of the compressional pressure from the thermal pressure [ST 81c].

At the late stage of the reaction, the system breaks up into nucleons and light nuclei, thus the calculation is carried out to $\rho=0.5 \rho_0$, at which point it is assumed that the fragments no longer interact. The distribution of fragments is calculated via a statistical model very similar to the quantum statistical model described in Chapter V, but including only the ground states of fragments up to ${}^4\text{He}$. The particle cross sections for each fluid element are then summed, and inclusive cross sections are obtained by a weighted average over the impact parameter [CS 81, BU 83].

In order to view the dynamics of the collision as described by the hydrodynamical model, one can generate contour plots of the nucleon densities at various stages of the reaction. Figure VI-8 shows a sequence of density contour plots illustrating the time evolution of 84 MeV/nucleon C + Au collisions. The plots shown are for impact parameters $b = 1, 3, 5,$ and 7 fm, starting from the top of the figure. The arrows indicate the laboratory velocity of the nucleons. At all impact parameters the matter was found to be compressed by 30%, and, except for peripheral collisions with $b > 7$ fm, was squeezed to the side. When double differential cross sections for protons from the calculation were compared with data [JA 81, GL 82], the overall shape as well as the angular dependence of the high energy tails of the spectra agreed quite well. The theory underestimated the total proton yield by a factor of 6, however, which was attributed to the decay of excited nuclear states neglected in the chemical equilibrium in the model [BU 83].

2. COMPARISON WITH DATA

Calculations were performed for Ar + Au data of the present work, at 137, 92 and 42 MeV/nucleon, and the chemical equilibrium distribution of particles was computed at $\rho = 0.5 \rho_0$ to generate inclusive spectra of protons and light fragments [BU 84]. The results of the calculations are compared with the data in Figure VI-9 through VI-11 for

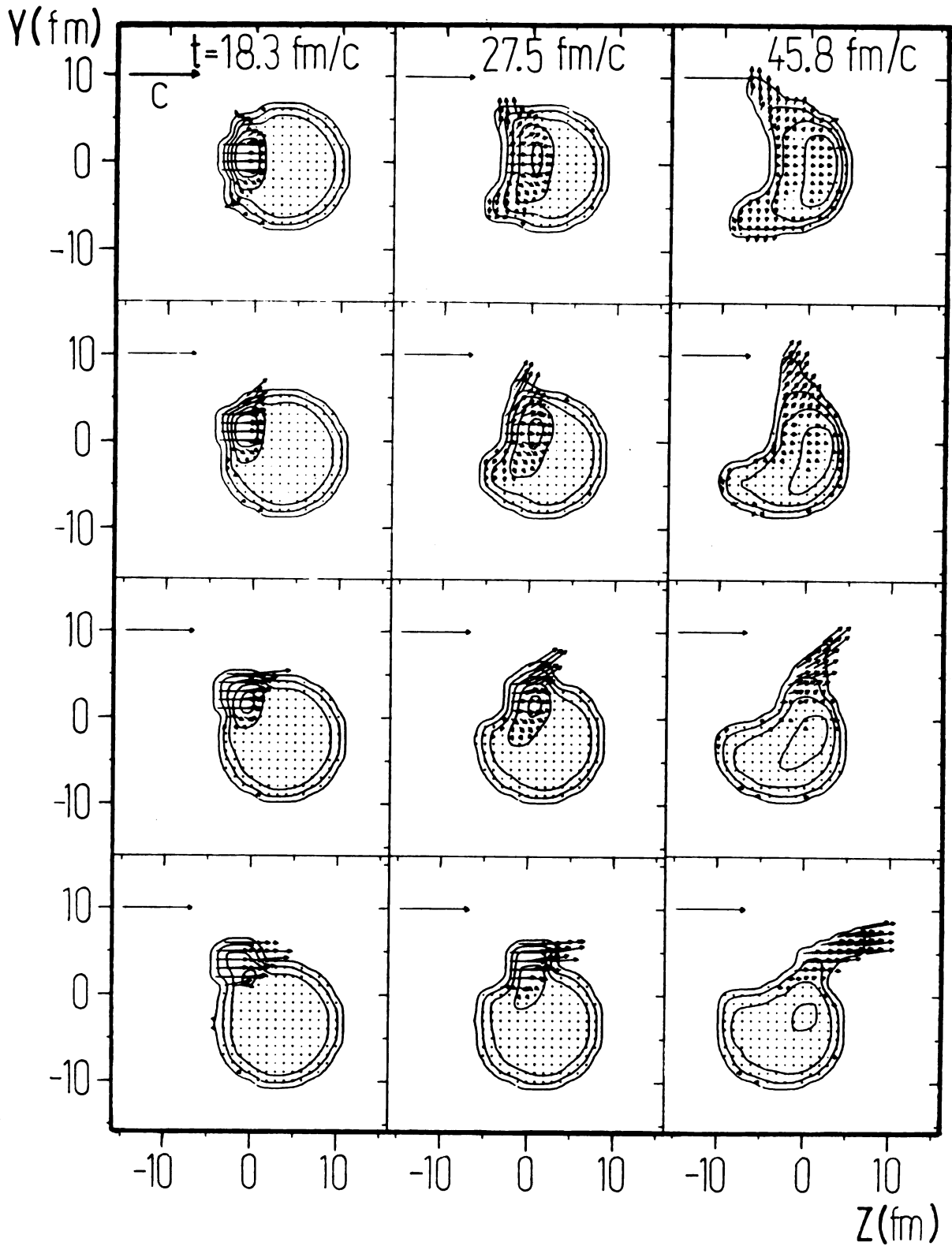


FIGURE VI-8. Time evolution of the 84 MeV/A 12C + Au reaction in a fluid dynamical calculation for impact parameters $b=1, 3, 5,$ and 7 fm .

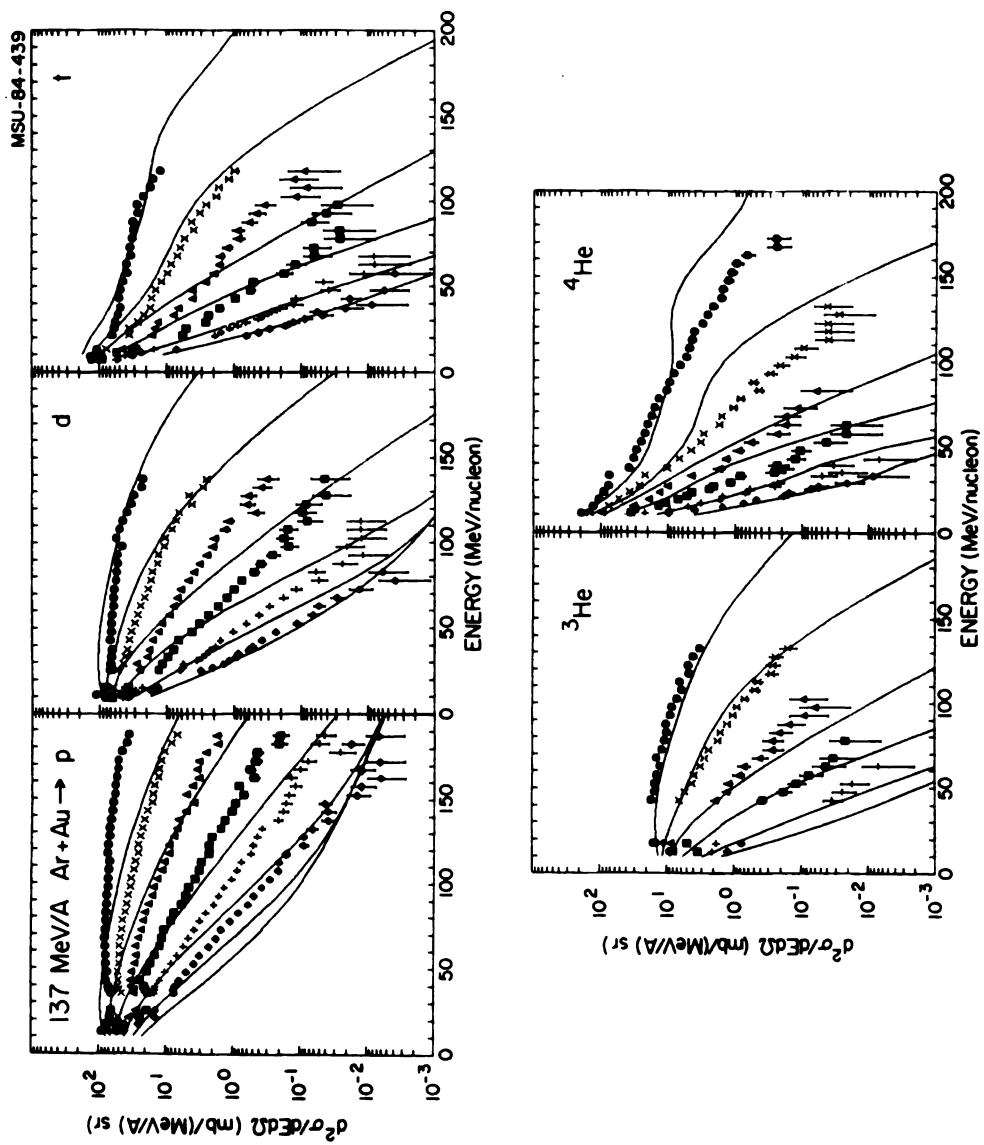


FIGURE VI-9. Fluid dynamical results (solid lines) for light particle spectra from 137 MeV/A Ar + Au.

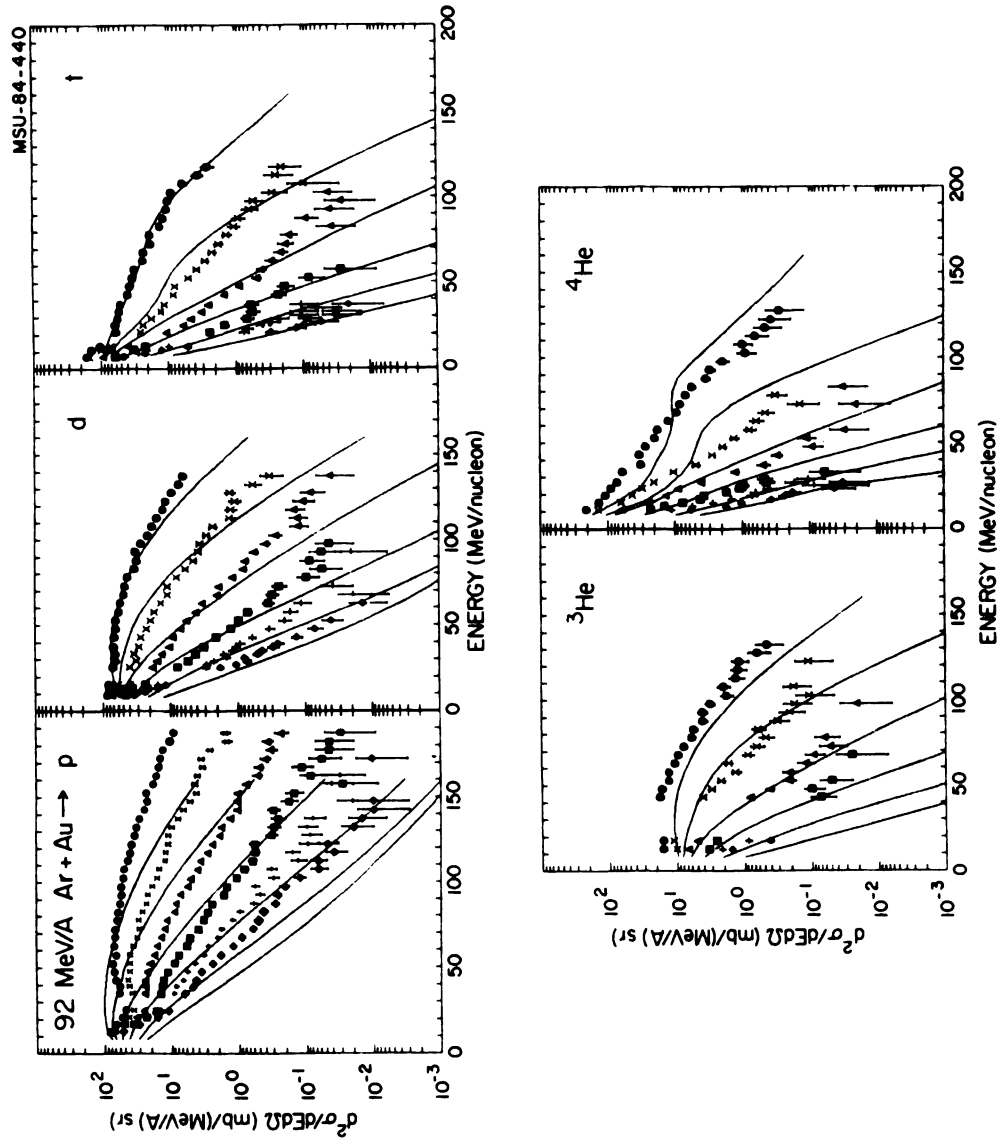


FIGURE VI-10. Fluid dynamical results (solid lines) for light particle spectra from 92 MeV/A Ar + Au.

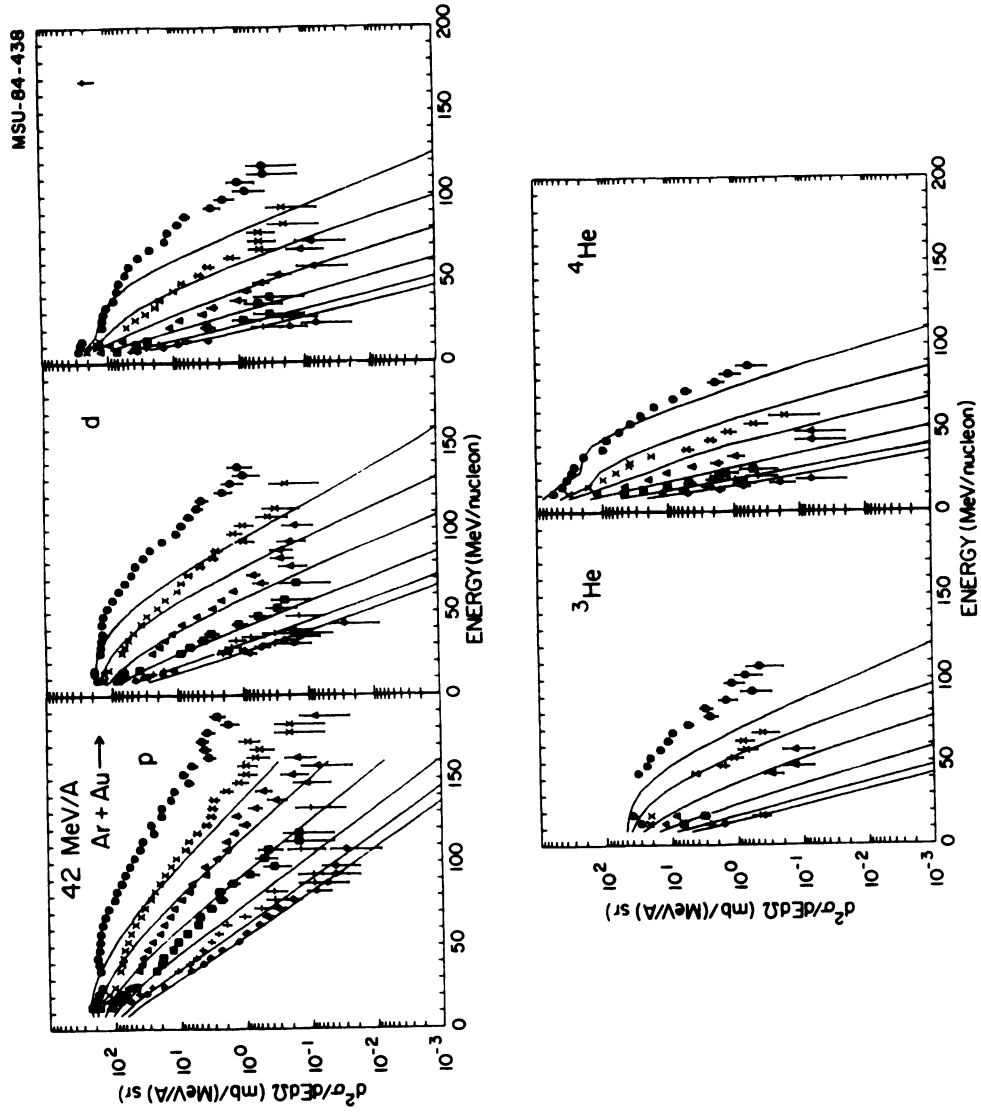


FIGURE VI-11. Fluid dynamical results (solid lines) for light particle spectra from 42 MeV/A Ar + Au.

the 137, 92, and 42 MeV/nucleon cases, respectively. It is important to note that the normalization of the calculation is arbitrary: a normalization factor has been applied for the hydrodynamic result for each particle. These normalization factors are given in Table VI-1.

The renormalized calculations show moderately good agreement with the data for particles heavier than protons. The agreement, however, degrades with decreasing bombarding energy. The calculated proton spectra are too steep at all bombarding energies, while the ^4He spectra at 30° and 50° are incorrectly predicted to have bumps in the cross sections close to the beam energy/nucleon. The differences in the proton spectra predicted and observed for the 137 MeV/nucleon case make it difficult to determine whether hydrodynamic behavior is in fact responsible for the underprediction of the 50° and 70° spectra by the Boltzmann equation. It is likely that impact parameter selected data and calculations are required to answer this question. At 42 MeV/nucleon, the high energy tails of the spectra are consistently underpredicted, especially for angles $< 90^\circ$.

Table VI-1 shows that the proton and deuteron cross sections are underpredicted by the calculation. The discrepancy in the proton spectra was explained by the omission of particle-unstable clusters in the chemical equilibrium step [BU 83]. Such decays would produce many protons, but it is unlikely that the deuteron cross sections would increase noticeably. The overprediction of triton and

Table VI-1. Renormalization factors for comparison of fluid dynamical results to light particle data for Ar + Au reactions.

PARTICLE	137 MeV/A	92 MeV/A	42 MeV/A
p	10	16	40
d	4	4	9
t	0.5	0.3	0.7
³ He	1	1	4
⁴ He	0.17	0.1	0.7

alpha particle production may perhaps be expected due to the omission of heavier fragments in the chemical equilibrium. Some of the nucleons present as alpha particles in the calculated distribution would in fact be part of heavier clusters. It is nevertheless clear from the present comparison that the hydrodynamical approach does not provide a complete picture of intermediate energy reactions. At 42 MeV/nucleon the calculation looks different from the data (although this is less true at backward angles), suggesting that the validity of the short mean free path assumption is very questionable here. It was suggested that $R/\lambda > 3$ yields local thermal equilibration [KN 79]; it is evident that although the particle energy spectra appear thermal, this prerequisite for hydrodynamics does not seem to be met as the bombarding energy falls below 50 MeV/nucleon.

CHAPTER VII

SUMMARY AND CONCLUSIONS

A. SUMMARY OF RESULTS

The emission of light and complex fragments up to $A=14$ has been studied in intermediate energy argon and neon-induced reactions. The energy spectra were observed to fall approximately exponentially with energy, and could be described by a Boltzmann distribution. Plotting contours of constant cross section in the rapidity vs. perpendicular momentum plane revealed that many of the observed particles arise from a source moving with a rapidity intermediate between that of the target and of the projectile. Combining this observation with the thermal appearance of the energy spectra, a subset of the data was fitted with the assumption of emission from a single moving source. The parameters describing the intermediate rapidity source were extracted. Fitting the full data with three sources, including a projectile-like, target-like and intermediate source, yielded similar values for the parameters describing the intermediate rapidity source.

The systematics of the extracted source temperatures and velocities were studied for various beam-target combinations. The extracted source parameters were found to be relatively independent of the mass of the emitted fragment, suggesting that complex fragments as well as light

particles are emitted from a thermalized subsystem of the projectile and target.

Calculations were performed with the fireball model and the temperatures of the particle spectra were approximately reproduced, but the fireball velocity differed from the velocity of the intermediate source. This suggested that although the fireball geometry is inadequate at these bombarding energies, thermalization of a subset of the nucleons is still a useful concept. The question of the entropy in this thermalized system was explored, and it was shown that a quantum statistical model incorporating production of heavier fragments must be used to extract reliable information about the entropy from the data. A calculation assuming chemical equilibrium at the entropy per nucleon describing the heavy fragment ($A > 4$) distribution was unable to match the observed cross sections for light particles. However, it was recognized that the inclusive data are in fact summed over impact parameter and include collisions producing very small interaction regions. These peripheral collisions produce predominantly light particles. The entropy extracted from target-like fragments was found to be independent of the projectile energy and corresponded to the entropy expected for a heavy nucleus excited to its binding energy. The entropy extracted from midrapidity fragments was higher.

The spectra of complex fragments were well described by the proton spectra raised to the $A^{1/3}$ power. The concept of

coalescence of nucleons emitted close together in momentum space into complex fragments was invoked to explain this phenomenon, and the radius of a coalescence sphere in momentum space was extracted for each observed fragment. This approach worked well for emission of fragments as heavy as nitrogen, and the coalescence radius was linked to the size of the source emitting the particles. This source was found to have a radius between 4.5 and 5.5 fm, in agreement with experiments measuring two-proton correlations.

The light particle data was also used to test two models describing the dynamics of the collisions. The first was a solution of the Boltzmann equation, incorporating a mean field and Pauli blocking as well as two-nucleon collisions into an extension of the intranuclear cascade approach. A generalized coalescence in phase space was used to separate the projectile and target remnants from the observed particle spectra. The mean field and Pauli blocking were found to be necessary to describe the observed proton spectra.

In order to further test the limits of applicability of models describing relativistic heavy ion collisions, nuclear fluid dynamical calculations were performed. After renormalization of the calculation to the data, the agreement with light particle spectra was fair at the two higher energies, but the calculated spectral shapes were different from the observed energy distributions at 42 MeV/nucleon.

B. CONCLUSIONS

This survey of intermediate energy heavy ion reactions has answered a number of questions about the evolution of the reaction mechanism as the bombarding energy increases, but has raised many more. The concept of thermalization of a subsystem of the nucleons in the reaction seems to be valid for intermediate bombarding energies. The energy spectra of observed particles may be described by emission from a single moving source, as in higher energy collisions. The temperatures of the sources vary smoothly with bombarding energy, indicating that the transition to mechanisms typical of relativistic energy reactions is a smooth one. Although this seems to rule out any abrupt transitions such as a phase transition from a nuclear liquid to a nuclear gas, the small sizes of the systems created would cause large fluctuations, masking the sharp changes in temperature or fragment sizes typical of such transitions.

Comparison of data with the fireball model, which assumes clean cuts in the projectile and target, shows that the simple geometrical picture is inadequate at these bombarding energies, where the reaction is slow enough to allow exchange of particles between the "participants" and the "spectators". The detailed time evolution of the thermalized subsystem remains to be determined. The system may start out as a hot spot in the target nucleus and grow into the surrounding target matter, or it may undergo a rapid explosion into nucleons and nuclear fragments.

Experiments investigating the correlations among such fragments will be necessary to address this question.

Midrapidity fragments with $A > 4$ also arise from a thermal source. Their energy spectra and angular distributions are consistent with their formation via coalescence of nucleons emitted close together in momentum space. This agreement suggests that they arise from collisions with rather large interaction regions, and therefore small impact parameters. It remains to be determined whether one can use the emission of such fragments as an impact parameter trigger, and whether the central collisions result in a multifragmentation of the system, or in a very hot gas of nucleons which freezes out into small and large fragments.

The production of heavy fragments can also be used to learn about the entropy generated in the collision, as the entropy cannot be reliably inferred from the deuteron-to-proton ratio alone. The entropy from target-like fragments is independent of the projectile identity and energy, suggesting that the target absorbs a limited amount of energy and breaks up in a similar manner regardless of the fate of the participant region. The entropy extracted from midrapidity fragments is higher, in agreement with the expectation that they arise from a more violent interaction.

Detailed dynamical descriptions of reactions in this energy regime were found to need elements of low energy reactions (such as the influence of a nuclear mean field and

Pauli blocking) and of high energy reactions (the two-body dissipation mechanism inherent in nucleon-nucleon collisions). The assumption of a very short mean free path in this energy regime was found to be inadequate, especially for collisions at $E_{\text{LAB}} < 50$ MeV/nucleon. It remains to be investigated at which point the low energy effects become negligible, however it is unlikely that a simple cutoff in bombarding energy will be found. It is more likely that complete theories to describe the intermediate energy regime will merge with theories used for relativistic collisions, yielding similar results at the higher bombarding energies.

First coincidence experiments are already being performed, and the outcomes should help to more fully describe the bombarding energy evolution in the reaction dynamics. The further study of intermediate energy heavy ion reactions promises to allow us to form, at last, a unified picture of the response of nuclear matter from very gentle to very energetic excitation.

LIST OF REFERENCES

LIST OF REFERENCES

A

- [AB 72] M. Abramowitz and I.A. Stegun, Handbook of Mathematical Functions (Dover, New York, 1972).
- [AD 84] B.P. Adyasevich, V.G. Antonenko, Yu.I. Grigoryan, M.S. Ippolitov, K.V. Karadzhev, A.L. Lebedev, V.I. Manko, S.A. Nikolaev, Yu.P. Polunin, A.A. Tsvetkov and A.A. Vinogradov, Phys. Lett. 142B, 245 (1984).
- [AI 84] J. Aichelin and J. Hüfner, Phys. Lett. 136B, 15 (1984).
- [AI 84a] J. Aichelin, J. Hüfner and R. Ibarra, Phys. Rev. C30, 107 (1984).
- [AM 75] A.A. Amsden, G.F. Bertsch, F.H. Harlow and J.R. Nix, Phys. Rev. Lett. 35, 905 (1975).
- [AU 82] R.L. Auble, J.B. Ball, F.E. Bertrand, C.B. Fulmer, D.C. Hensley, I.Y. Lee, R.L. Robinson, P.H. Stelson, C.Y. Wong, D.L. Hendrie, H.D. Holmgren and J.D. Silk, Phys. Rev. Lett. 49, 441 (1982).
- [AU 83] R.L. Auble, J.B. Ball, F.E. Bertrand, C.B. Fulmer, D.C. Hensley, I.Y. Lee, R.L. Robinson, P.H. Stelson, C.Y. Wong, D.L. Hendrie, H.D. Holmgren and J.D. Silk, Phys. Rev. C28, 1552 (1983).
- [AW 81] T.C. Awes, G. Poggi, S. Saini, C.K. Gelbke, R. Legrain and G.D. Westfall, Phys. Lett. 103B, 417 (1981).
- [AW 81a] T.C. Awes, G. Poggi, C.K. Gelbke, B.B. Back, B.G. Glagola, H. Breuer and V.E. Viola, Jr., Phys. Rev. C24, 89 (1981).
- [AW 82] T.C. Awes, S. Saini, G. Poggi, C.K. Gelbke, D. Cha, R. Legrain and G.D. Westfall, Phys. Rev. C25, 2361 (1982).

B

- [BA 75] H.G. Baumgardt, T.U. Schott, Y. Sakamoto, E. Schopper, H. Stöcker, J. Hofmann, W. Scheid and W. Greiner, Z. Phys. A273, 359 (1975).
- [BA 75a] R. Balescu, Equilibrium and Nonequilibrium Statistical Mechanics, (John Wiley and Sons, New York 1975) p. 384.
- [BE 76] H.W. Bertini, R.T. Santoro and O.W. Hermann, Phys. Rev. C14, 590 (1976).
- [BE 81] G.F. Bertsch and J. Cugnon, Phys. Rev. C24, 2514 (1981).
- [BE 84] G. Bertsch, H. Kruse and S. DasGupta, Phys. Rev. C29, 673 (1984).
- [BI 79] J.R. Birkelund, L.E. Tubbs, J.R. Huizenga, J.N. De and D. Sperber, Phys., Rep. 56, 107 (1979).
- [BI 80] M. Bini, C.K. Gelbke, D.K. Scott, T.J.M. Symons, P. Doll, D.L. Hendrie, J.L. Laville, M.C. Mermaz, C. Olmer, K. VanBibber and H.H. Wieman, Phys. Rev. C22, 1945 (1980).
- [BO 73] J.D. Bowman, W.J. Swiatecki and C.F. Tsang, LBL Report No. LBL-2908 (1973).
- [BO 76] P. Bonche, S. Koonin and J.W. Negele, Phys. Rev. C13, 1226 (1976).
- [BO 83] B. Borderie, M.F. Rivet, I. Forest, J. Galin, D. Guerreau, R. Bimbot, D. Gardes, B. Gatty, M. Lefort, H. Oeschler, S. Sung, B. Tamain and X. Tarrago, Nucl. Phys. A402, 57 (1983).
- [BO 83a] V. Borrel, D. Guerreau, J. Galin, B. Gatty, D. Jacquet and X. Tarrago, Z. Phys. A314, 191 (1983).
- [BO 83b] D.H. Boal, Phys. Rev. C28, 2568 (1983).
- [BO 84] David H. Boal, Michigan State University, preprint MSUCL-451 (1984), to be published in Advances in Nuclear Physics, J.W. Negele and E. Vogt, editors.
- [BO 84a] David H. Boal, Phys. Rev. C30, 749 (1984).

- [BO 84b] D.H. Boal and J.H. Reid, Phys. Rev. C29, 973 (1984).
- [BR 79] H. Breuer, B.G. Glagola, V.E. Viola, K.L. Wolf, A.C. Mignerey, R. Birkelund, D. Hilscher, A.D. Hoover, J.R. Huizenga, W.U. Schröder and W.W. Wilcke, Phys. Rev. Lett. 43, 191 (1979).
- [BU 81] G. Buchwald, L.P. Csernai, J.A. Maruhn, W. Greiner and H. Stöcker, Phys. Rev. C24, 135 (1981).
- [BU 83] G. Buchwald, G. Graebner, J. Theis, J.A. Maruhn, W. Greiner, and H. Stöcker, Phys. Rev. C28, 1119 (1983).
- [BU 84] G. Buchwald, private communication (1984).

C

- [CA 84] G. Caskey, A. Galonsky, B. Remington, M.B. Tsang, C.K. Gelbke, A. Kiss, F. Deak, Z. Seres, J.J. Kolata and J. Hinnefeld, Michigan State University preprint MSUCL-465 (1984).
- [CE 81] R.A. Cecil, B.D. Anderson, A.R. Baldwin, R. Madey, W. Schimmerling, J.W. Kast and D. Ortendahl, Phys. Rev. C24, 2013 (1981).
- [CH 73] G.F. Chapline, M.H. Johnson, E. Teller and M.S. Weiss, Phys. Rev. D8, 4302 (1973).
- [CH 83] C.B. Chitwood, D.J. Fields, C.K. Gelbke, W.G. Lynch, A.D. Panagiotou, M.B. Tsang, H. Utsunomiya and W.A. Friedman, Phys. Lett. 131B, 289 (1983).
- [CH 84] C.B. Chitwood, J. Aichelin, D. Boal, G.F. Bertsch, D.J. Fields, C.K. Gelbke, W.G. Lynch, M.B. Tsang, J.C. Shillcock, T.C. Awes, R.L. Ferguson, F.E. Obenshain, F. Plasil, R.L. Robinson and G.R. Young, MSU Preprint MSUCL-479 (1984).
- [CL 82] M.R. Clover, R.M. DeVries, N.J. DiGiacomo, and Y. Yariv, Phys. Rev. C26, 2138 (1982).
- [CO 80] M.T. Collins and J.J. Griffin, Nucl. Phys. A348, 63 (1980).
- [CS 81] L.P. Csernai and H.W. Barz, Z. Phys. A296, 173 (1981).
- [CS 83] L.P. Csernai, H. Stöcker, P.R. Subramanian, G. Buchwald, G. Graebner, A. Rosenhauer, J.A. Maruhn and W. Greiner, Phys. Rev. C28, 2001 (1983).

- [CU 80] R.Y. Cusson, J. Maruhn and H. Stöcker, Z. Phys. A294, 125 (1980).
- [CU 80a] J. Cugnon, Phys. Rev. C22, 1885 (1980).
- [CU 81] J. Cugnon, T. Mizutani and J. Vandermeulen, Nucl. Phys. A352, 505 (1981).
- [CU 81a] J. Cugnon, Phys. Rev. C23, 2094 (1981).
- [CU 82] J. Cugnon, D. Kinet and J. Vandermeulen, Nucl. Phys. A379, 553 (1982).
- [CU 82a] J. Cugnon, Nucl. Phys. A387, 191c (1982).

D

- [DA 81] S. DasGupta and A. Mekjian, Phys. Reports 72C, 133 (1981).

F

- [FA 82] G. Fai and J. Randrup, Nucl. Phys. A381, 537 (1982).
- [FI 82] J.E. Finn, S. Agarwal, A. Bujak, J. Chuang, L.J. Gutay, A.S. Hirsch, R.W. Minich, N.T. Porile, R.P. Scharenberg, B.C. Stringfellow and F. Turkot, Phys. Rev. Lett. 49, 1321 (1982).
- [FI 84] D.J. Fields, W.G. Lynch, C.B. Chitwood, C.K. Gelbke, M.B. Tsang, H. Utsunomiya and J. Aichelin, Michigan State University preprint MSUCL-471 (1984).
- [FR 81] K.A. Frankel and J.D. Stevenson, Phys. Rev. C23, 1511 (1981).
- [FR 83] W.A. Friedman and W.G. Lynch, Phys. Rev. C28, 16 (1983).
- [FU 84] S.Y. Fung, D. Beavis, S.Y. Chu, D. Keane, Y.M. Liu, R.T. Poe, G. VanDalen and M. Vient, Conference on Intersections Between Particle and Nuclear Physics, Steamboat Springs, May 1984.

G

- [GA 80] S.I.A. Garpman, S.K. Samaddar, D. Sperber and M. Zielinskapfabe, Phys. Lett. 92B, 56 (1980).

- [GA 82] J. Galin, H. Oeschler, S. Song, B. Borderie, M.F. Rivet, I. Forest, R. Bimbot, D. Gardes, B. Gatty, H. Guillemot, M. Lefort, B. Tamain and X. Tarrago, Phys. Rev. Lett. 48, 1787 (1982).
- [GE 78] C.K. Gelbke, C. Olmer, M. Buenard, D.L. Hendrie, J. Mahoney, M.C. Mermaz and D.K. Scott, Phys. Reports 42, 311 (1978).
- [GL 75] D. Glas and U. Mosel, Nucl. Phys. A237, 429 (1975).
- [GL 82] R. Glasow, G. Gaul, B. Ludewigt, R. Santo, H. Ho, W. Kühn, U. Lynen and W.F.J. Müller, Phys. Lett. 108B, 15 (1982); Phys. Lett. 120B, 71 (1983).
- [GO 75] F.S. Goulding and B.G. Harvey, Ann. Rev. Nucl. Sci. 25, 167 (1975).
- [GO 77] J. Gosset, H.H. Gutbrod, W.G. Meyer, A.M. Poskanzer, A. Sandoval, R. Stock and G.D. Westfall, Phys. Rev. C16, 629 (1977).
- [GO 78] J. Gosset, J.I. Kapusta and G.D. Westfall, Phys. Rev. C18, 844 (1978).
- [GO 78a] A.S. Goldhaber, Phys. Rev. C17, 2243 (1978).
- [GO 79] A.S. Goldhaber and H.H. Heckman, Ann. Rev. Nucl. Sci. 28, 161 (1979).
- [GO 79a] P.A. Gottschalk and M. Weström, Nucl. Phys. A314, 232 (1979).
- [GO 80] A. Gobbi and W. Nörenberg, Heavy Ion Collisions, Vol. 2, p. 128, Edited by R. Bock, (North Holland Publishing, 1980).
- [GO 83] P.L. Gonthier, H. Ho, M.N. Namboodiri, J.B. Natowitz, L. Adler, S. Simon, K. Hagel, S. Kniffen and A. Khodai, Nucl. Phys. A411, 284 (1983).
- [GR 75] D.E. Greiner, P.J. Lindstrom, H.H. Heckman, B. Cork and F.S. Bieser, Phys. Rev. Lett. 35, 152 (1975).
- [GR 80] Ray E.L. Green and Ralph G. Korteling, Phys. Rev. C22, 1594 (1980).
- [GR 81] G. Gregoire, C. Ngô and B. Remaud, Phys. Lett. 99B, 17 (1981).
- [GR 84] C. Gregoire and F. Scheuter, GANIL preprint P84-06 (1984).
- [GR 84a] Ray E.L. Green, Ralph G. Korteling and K. Peter Jackson, Phys. Rev. C29, 1806 (1984).

- [GU 76] H.H. Gutbrod, A. Sandoval, P.J. Johansen, A.M. Poskanzer, J. Gosset, W.G. Meyer, G.D. Westfall and R. Stock, Phys. Rev. Lett. 37, 667 (1976).
- [GU 83] H.H. Gutbrod, H. Löhner, A.M. Poskanzer, T. Renner, H. Riedesel, H.G. Ritter, A. Warwick, F. Weik and H. Wieman, Phys. Lett. 127B, 317 (1983).
- [GU 84] H.A. Gustafsson, H.H. Gutbrod, B. Kolb, H. Löhner, B. Ludewigt, A.M. Poskanzer, T. Renner, H. Riedesel, H.G. Ritter, A. Warwick, F. Weik and H. Wieman, Phys. Rev. Lett. 53, 544 (1984).

H

- [HA 79] R.L. Hatch and S.E. Koonin, Phys. Lett. 81B, 1 (1979).
- [HA 84] B. Hasselquist, G.M. Crawley, L.H. Harwood, B.V. Jacak, Z.M. Koenig, G.D. Westfall, J. Yurkon, J.P. Dufour and T.J.M. Symons, to be published.
- [HE 78] H.H. Heckman, D.E. Greiner, P.J. Lindstrom and H. Shwe, Phys. Rev. C17, 1735 (1978).
- [HY 71] E.K. Hyde, G.W. Butler and A.M. Poskanzer, Phys. Rev. C4, 1759 (1971).

J

- [JA 78] J. Jaros, A. Wagner, L. Anderson, O. Chamberlain, R.Z. Fuzesy, J. Gallup, W. Gorn, L. Schroeder, S. Shannon, G. Shapiro and H. Steiner, Phys. Rev. C18, 2273 (1978).
- [JA 81] B. Jakobsson, L. Carlen, P. Kristiansson, J. Krumlinde, A. Oskarsson, I. Otterlund, B. Schröder, H.-A. Gustafsson, T. Johansson, H. Ryde, G. Tibell, J.P. Bondorf, G. Fai, A.O.T. Karvinen, O.B. Nielsen, M. Buenard, J. Cole, D. Lebrun, J.M. Loiseaux, P. Martin, R. Ost, P. de Saintignon, C. Guet, E. Monnard, J. Mougey, H. Nifenecker, P. Perrin, J. Pinston, C. Ristori and F. Schussler, Phys. Lett. 102B, 121 (1981).
- [JA 82] B. Jakobsson, G. Jönsson, B. Lindkvist and A. Oskarsson, Z. Phys. A307, 293 (1982).
- [JA 83] B.V. Jacak, G.D. Westfall, C.K. Gelbke, L.H. Harwood, W.G. Lynch, D.K. Scott, H. Stöcker, M.B. Tsang and T.J.M. Symons, Phys. Rev. Lett. 51, 1846 (1983).

- [JA 84] B.V. Jacak, G.D. Westfall, N. Anantaraman, M.W. Curtin, C.K. Gelbke, L.H. Harwood, B. Hasselquist, Z.M. Koenig, A.D. Panagiotou and D.K. Scott, to be published.
- [JE 82] B.K. Jennings, S. DasGupta and N. Mobed, Phys. Rev. C25, 278 (1982).

K

- [KA 84] Joseph Kapusta, Phys. Rev. C29, 1735 (1984).
- [KN 79] J. Knoll and J. Randrup, Nucl. Phys. A324, 445 (1979).
- [KR 84] H. Kruse, B.V. Jacak and H. Stöcker, Michigan State University preprint MSUCL-470 (1984).
- [KR 84a] H. Kruse, B.V. Jacak, H. Stöcker and G.D. Westfall, Michigan State University preprint MSUCL-478 (1984).

L

- [LA 83] G. La Rana, G. Nebbia, E. Tomasi, C. Ngô, X.S. Chen, S. Leray, P. Lhenoret, R. Lucas, C. Mazur, M. Ribrag, C. Cerruti, S. Chiodelli, A. Demeyer, D. Guinet, J.L. Charvet, M. Morjean, A. Peghaire, Y. Pranal, L. Sinopoli, J. Uzureau and R. De Swiniarski, Nucl. Phys. A407, 233 (1983).
- [LE 74] M. Lefort, J. Phys. A7, 107 (1974).
- [LE 79] M.C. Lemaire, S. Nagamiya, S. Schnetzer, H. Steiner and I. Tanihata, Phys. Lett. 85B, 38 (1979).
- [LE 83] S. Leray, G. Nebbia, C. Gregoire, G. La Rana, P. Lhenoret, C. Mazur, C. Ngô, M. Ribrag, E. Tomasi, S. Chiodelli, J.L. Charvet and C. Lebrun, Saclay Preprint (1983), Nucl. Phys. A425, 345 (1984).
- [LI 80] E.M. Lifshitz and L.P. Pitaevskii, Statistical Physics (Pergamon Press, Oxford, 1980), p. 115.
- [LY 82] U. Lynen, H. Ho, W. Kühn, D. Pelte, U. Winkler, W.F.J. Müller, Y.-T. Chu, P. Doll, A. Gobbi, K. Hildenbrand, A. Olmi, H. Sann, H. Stelzer, R. Bock, H. Löhner, R. Glasow and R. Santo, Nucl. Phys. A387, 129c (1982).
- [LY 83] W.G. Lynch, C.B. Chitwood, M.B. Tsang, D.J. Fields, D.R. Klesch, C.K. Gelbke, G.R. Young, T.C. Awes, R.L. Ferguson, F.E. Obenshain, F. Plasil, R.L.

Robinson and A.D. Panagiotou, Phys. Rev. Lett. 51, 1850 (1983).

M

- [MA 80] R. Malfliet, Phys. Rev. Lett. 44, 864 (1980).
- [MA 82] V.I. Manko and S. Nagamiya, Nucl. Phys. A384, 475 (1982).
- [MA 83] Rudi Malfliet and Bernd Shürmann, Phys. Rev. C28, 1136 (1983).
- [MA 84] Rudi Malfliet, Groningen Preprint, (1984).
- [ME 69] D.F. Measday and C. Richard-Serre, Nucl. Instrum. Methods 76, 45 (1969).
- [ME 77] A.Z. Mekjian, Phys. Rev. Lett. 38, 640 (1977).
- [ME 78] A.Z. Mekjian, Phys. Rev. C17, 1051 (1978).
- [ME 80] W.G. Meyer, H.H. Gutbrod, Ch. Lukner and A. Sandoval, Phys. Rev. C22, 179 (1980).
- [MI 80] I.M. Mishustin, F. Myhrer and P.J. Siemens, Phys. Lett. 95B, 361 (1980).
- [MO 84] D.J. Morrissey, W. Benenson, E. Kashy, B. Sherrill, A.D. Panagiotou, R.A. Blue, R.M. Ronningen, J. VanderPlicht and H. Utsunomiya, MSU Preprint MSUCL-454 (1984).

N

- [NA 81] S. Nagamiya, M.-C. Lemaire, E. Moeller, S. Schnetzer, G. Shapiro, H. Steiner and I. Tanihata, Phys. Rev. C24, 971 (1981).
- [NA 81a] J.B. Natowitz, M.N. Namboodiri, L. Adler, R.P. Schmitt, R.L. Watson, S. Simon, M. Berlinger and R. Choudhury, Phys. Rev. Lett. 47, 1114 (1981).
- [NA 82] S. Nagamiya, Phys. Rev. Lett. 49, 1383 (1982).
- [NA 84] S. Nagamiya and M. Gyulassy, Advances in Nuclear Physics, Vol. 13, 201 (1984).
- [NE 81] J.W. Negele and K. Yazai, Phys. Rev. Lett. 47, 71 (1981).
- [NE 82] J. Negele, Rev. Mod. Phys. 54, 913 (1982).

- [NI 81] J.R. Nix and D. Strottman, Phys. Rev. C23, 2548 (1981).

P

- [PA 72] R.K. Pathria, Statistical Mechanics (Pergamon Press, Oxford 1972), p. 221.
- [PA 84] A.D. Panagiotou, M.W. Curtin, H. Toki, D.K. Scott and P.J. Siemens, Phys. Rev. Lett. 52, 496 (1984).
- [PE 68] R.H. Pehl, F.S. Goulding, D.A. Landis and M. Lenzlinger, Nucl. Instrum. Methods 59, 45 (1968).
- [PO 75] A.M. Poskanzer, R.G. Sextro, A.M. Zebelman, H.H. Gutbrod, A. Sandoval and R. Stock, Phys. Rev. Lett. 35, 1701 (1975).
- [PO 84] E.C. Pollaco, M. Conjeaud, S. Harar, C. Volant, Y. Cassagnou, R. Dayras, R. Legrain, M.S. Nguyen, H. Oeschler and F. Saint-Laurent, Saclay Preprint 2124 03/1984 (1984).
- [PR 83] Proceedings of the International Conference on Nucleus-Nucleus Collisions, Nucl. Phys. A400 (1983).
- [PR 83a] Proceedings of the 6th High Energy Heavy Ion Study and 2nd Workshop on Anomalons, Lawrence Berkeley Laboratory Report LBL-16281, December 1983.

R

- [RA 81] J. Randrup and S.E. Koonin, Nucl. Phys. A356, 223 (1981).
- [RA 84] F. Rami, J.P. Coffin, G. Guillaume, B. Heusch, P. Wagner, A. Fahli and P. Fintz.
- [RE 65] D.V. Reames, Phys. Rev. 137, B332 (1965).

S

- [SA 80] A. Sandoval, H.H. Gutbrod, W.G. Meyer, R. Stock, Ch. Lukner, A.M. Poskanzer, J. Gosset, J.-C. Jourdain, C.H. King, Nguyen Van Sen, G.D. Westfall and K.L. Wolf, Phys. Rev. C21, 1321 (1980).
- [SA 83] A. Sandoval, R. Bock, R. Brockman, A. Dacal, J.W. Harris, M. Maier, M.E. Ortiz, H.G. Pugh, W. Rauch, R.E. Renfordt, F. Riess, L.S. Schroeder, R. Stock.

- H. Ströbele and K.L. Wolf, Nucl. Phys. A400, 365c (1983).
- [SC 77] W.U. Schröder and J.R. Huizenga, Ann. Rev. Nucl. Sci. 27, 465 (1977).
- [SC 80] J.P. Schiffer, Nucl. Phys. A335, 339 (1980).
- [SC 81] D.K. Scott, Nucl. Phys. A354, 375c (1981).
- [SC 82] O. Scholten, private communication (1982).
- [SI 79] K. Siwek-Wilczynska, E.H. duMarchie van Voorthuysen; J. van Popta, R.H. Siemssen and J. Wilczynski, Phys. Rev. Lett. 42, 1599 (1979); Nucl. Phys. A330, 150 (1979).
- [SI 79a] P.J. Siemens and J.I. Kapusta, Phys. Rev. Lett. 43, 1486 (1979).
- [SO 75] M.I. Sobel, P.J. Siemens, J.P. Bondorf and H.A. Bethe, Nucl. Phys. A251, 502 (1975).
- [SO 83] L.G. Sobotka, M.L. Padgett, G.J. Wozniak, G. Guarino, A.J. Pacheco, L.G. Moretto, Y. Chan, R.G. Stokstad, I. Tserruya and S. Wald, Phys. Rev. Lett. 51, 2187 (1983).
- [ST 77] J. Stevenson, P.B. Price and K. Frankel, Phys. Rev. Lett. 38, 1125 (1977).
- [ST 79] H. Stöcker, J.A. Maruhn and W. Greiner, Z. Phys. A293, 173 (1979).
- [ST 80] H. Stöcker, R.Y. Cusson, J.A. Maruhn and W. Greiner, Z. Phys. A294, 125 (1980).
- [ST 80a] H. Stöcker, J.A. Maruhn and W. Greiner, Phys. Rev. Lett. 44, 725 (1980).
- [ST 81] H. Stöcker, C. Riedel, Y. Yariv, L.P. Csernai, G. Buchwald, G. Graebner, J.A. Maruhn, W. Greiner, K. Frankel, M. Gyulassy, B. Shürmann, G. Westfall, J.D. Stevenson, J.R. Nix and D. Strottman, Phys. Rev. Lett. 47, 1807 (1981).
- [ST 81a] N. Stelte and R. Weiner, Phys. Lett. 103B, 275 (1981).
- [ST 81b] H. Stöcker, R.Y. Cusson, J. Maruhn and W. Greiner, Phys. Lett. 101B, 379 (1981).
- [ST 81c] H. Stöcker, M. Gyulassy and J. Boguta, Phys. Lett. 103B, 269 (1981).

- [ST 83] H. Stöcker, G. Buchwald, G. Graebner, P. Subramanian, J.A. Maruhn, W. Greiner, B.V. Jacak and G.D. Westfall, Nucl. Phys. A400, 63c (1983).
- [ST 84] H. Stöcker, J. of Phys. G10, L111 (1984).
- [SU 81] P.R. Subramanian, L.P. Csernai, H. Stöcker, J.A. Maruhn, W. Greiner and H. Kruse, J. of Phys. G7, L1241 (1981).
- [SY 80] T.J.M. Symons, P. Doll, M. Bini, D.L. Hendrie, J. Mahoney, G. Mantzouranis, D.K. Scott, K. VanBibber, Y.P. Viyogi, H.H. Wieman and C.K. Gelbke, Phys. Lett. 94B, 131 (1980).

T

- [TA 81] H.H.K. Tang, C.H. Dasso, H. Esbensen, R.A. Broglia and A. Winther, Phys. Lett. 101B, 10 (1981).
- [TO 83] V.D. Toneev and K.K. Gudima, Nucl. Phys. A400, 173 (1983).
- [TS 84] M.B. Tsang, D.R. Klesch, C.B. Chitwood, D.J. Fields, C.K. Gelbke, W.G. Lynch, H. Utsunomiya, K. Kwiatkowski, V.E. Viola and M. Fatyga, Phys. Lett. 134B, 169 (1984).

U

- [UE 33] E. Uehling and G. Uhlenbeck, Phys. Rev. 43, 552 (1933).

V

- [VO 78] V.V. Volkov, Phys. Reports 44, 93 (1978).

W

- [WA 83] A.I. Warwick, H.H. Wieman, H.H. Gutbrod, M.R. Maier, J. Peter, H.G. Ritter, H. Stelzer, F. Wiek, M. Freedman, D.J. Henderson, S.B. Kaufman, E.P. Steinberg and B.D. Wilkins, Phys. Rev. C27, 1083 (1983).
- [WE 76] G.D. Westfall, J. Gosset, P.J. Johansen, A.M. Poskanzer, W.G. Meyer, H.H. Gutbrod, A. Sandoval and R. Stock, Phys. Rev. Lett. 37, 1202 (1976).

- [WE 78] G.D. Westfall, R.G. Sextro, A.M. Poskanzer, A.M. Zebelman, G.W. Butler and E.K. Hyde, Phys. Rev. C17, 1368 (1978).
- [WE 82] G.D. Westfall, B.V. Jacak, N. Anantaraman, M.W. Curtin, G.M. Crawley, C.K. Gelbke, B. Hasselquist, W.G. Lynch, D.K. Scott, M.B. Tsang, M.J. Murphy, T.J.M. Symons, R. Legrain and T.J. Majors, Phys. Lett. 116B, 118 (1982).
- [WE 84] G.D. Westfall, Z.M. Koenig, B.V. Jacak, L.H. Harwood, G.M. Crawley, M.W. Curtin, C.K. Gelbke, B. Hasselquist, W.G. Lynch, A.D. Panagiotou, D.K. Soctt, H. Stöcker and M.B. Tsang, Phys. Rev. C29, 861 (1984).
- [WE 84a] G.D. Westfall, private communication (1984).
- [WI 80] J. Wilczynski, K. Siwek-Wilczynska, T. VanDriel, S. Gonggrip, D.C.J.M. Hageman, R.V.F. Janssens, J. Lukasiak and R.H. Siemssen, Phys. Rev. Lett. 45, 606 (1980).
- [WO 77] C.Y. Wong, J.A. Maruhn and T.A. Welton, Phys. Lett. 66B, 19 (1977).
- [WO 82] C.Y. Wong, Phys. Rev. C25, 1461 (1982).
- [WU 79] J.R. Wu, C.C. Chang and H.D. Holmgren, Phys. Rev. C19, 370 (1979).
- [WU 79a] J.R. Wu, C.C. Chang and H.D. Holmgren, Phys. Rev. C19, 659 (1979).
- [WU 80] J.R. Wu and I.Y. Lee, Phys. Rev. Lett. 45, 8 (1980).

Y

- [YA 79] Y. Yariv and Z. Fraenkel, Phys. Rev. C20, 2227 (1979).
- [YA 81] Y. Yariv and Z. Fraenkel, Phys. Rev. C24, 488 (1981).